Astronomy Letters, Vol. 30, No. 3, 2004, p. 139. Translated from Pis'ma v Astronomicheskiĭ Zhurnal, Vol. 30, No. 3, 2004, p. 163.

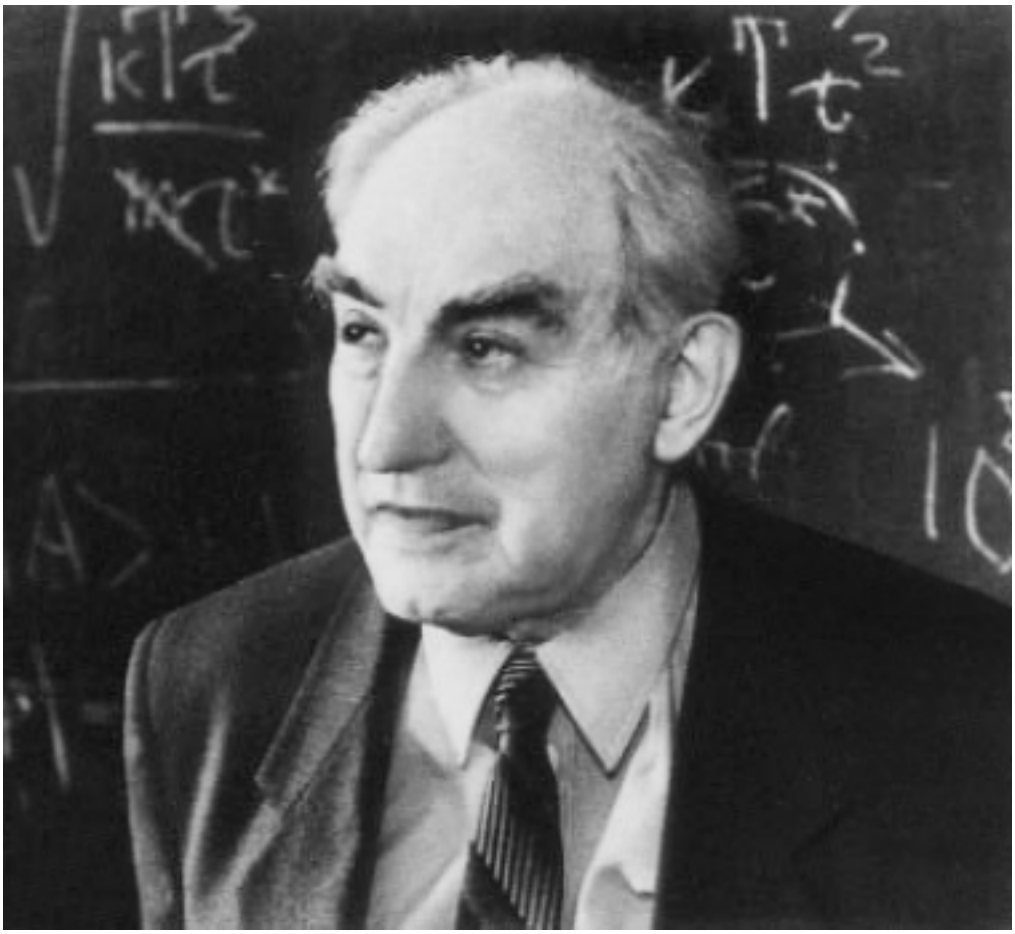

Vitaliĭ Lazarevich Ginzburg, 2003 Nobel Laureate in Physics

We heartily congratulate an outstanding physicist and astrophysicist, a member of the Editorial Board of our Journal

1063-7737/04/3003-0139$26.00

Astronomy Letters, Vol. 30, No. 3, 2004, pp. 140–147. Translated from Pis'ma v Astronomicheskiĭ Zhurnal, Vol. 30, No. 3, 2004, pp. 164–172.

The Origin of Intergalactic Thermonuclear Supernovae

A. G. Kuranov* **and K. A. Postnov****

Sternberg Astronomical Institute, Universitetskii pr. 13, Moscow, 119992 Russia

Received August 21, 2003

Abstract—The population synthesis method is used to study the possibility of explaining the appreciable fraction of the intergalactic type-Ia supernovae (SN Ia), $20^{+12}_{-15}\%$, observed in galaxy clusters (Gal-Yam *et al.* 2003) when close white dwarf binaries merge in the cores of globular clusters. In a typical globular cluster, the number of merging double white dwarfs does not exceed $\sim 10^{-13}$ per year per average cluster star in the entire evolution time of the cluster, which is a factor of ~ 3 higher than that in a Milky-Way-type spiral galaxy. From 5 to 30% of the merging white dwarfs are dynamically expelled from the cluster with barycenter velocities up to 150 km s^{-1}. SN Ia explosions during the mergers of double white dwarfs in dense star clusters may account for $\sim 1\%$ of the total rate of thermonuclear supernovae in the central parts of galaxy clusters if the baryon mass fraction in such star clusters is $\sim 0.3\%$.

Key words: *supernovae, globular clusters, stellar evolution.*

INTRODUCTION

SN Ia (thermonuclear supernovae) are among the most important objects in modern astrophysics, because the maximum of their optical light curves has a small spread. Therefore, they can be used[1] as a standard candle in modern cosmology, and fundamental conclusions about the expansion kinematics of the Universe can be reached (Riess *et al.* 1998; Perlmutter *et al.* 1999). The physical cause of an SN Ia explosion is the thermonuclear explosion of a white dwarf (WD) with a mass close to the Chandrasekhar limit (Hoyle and Fauler 1960). This idea is fully confirmed by detailed numerical calculations of the evolution of a white dwarf in a binary system (see, e.g., Dunina-Barkovskata *et al.* 2001). The WD mass can increase during mass transfer between the components in a close binary, which determines the astrophysical sources of such supernovae—double WDs that merge through gravitational radiation (Iben and Tutukov 1984; Webbink 1984) or accreting WDs in semidetached or symbiotic binaries with a second nondegenerate component (Whelan and Iben 1973; Nomoto 1982). SN Ia are observed in galaxies of all morphological types (van den Berg *et al.* 2003), and their rate (in SNU units) depends weakly on the type of galaxy (see Capellaro *et al.* (1997) and more recent papers of Capellaro's group).

At present, it is not completely clear which of these scenarios (or both) make the largest contribution to the SN Ia rate, and a considerable observational effort is being made to find the Galactic population of double WDs with a total mass close to or larger than the Chandrasekhar limit (e.g., the SPY project by Napiwotzki *et al.* 2003). We will adhere to the scenario of merging double WDs as the progenitors of type-Ia supernovae. The recent discovery of hydrogen emission lines in the spectrum of SN 2002ic (Hamuy *et al.* 2003) cannot rule out this formation channel of thermonuclear supernovae, because such SN Ia are atypical; their origin is the subject of debate (e.g., Livio and Riess 2003; Chugai and Yungelson 2003).

A dedicated search for supernovae in Abell clusters of galaxies (the WOOTS project; Gal-Yam *et al.* 2003) has revealed that two of the seven SN Ia found (SN 1998fc in Abell 403 at $z = 0.1$ and SN 2001al in Abell 2122/4 at $z = 0.066$) have no obvious host galaxies and can be associated only with faint dwarf galaxies with $M_R > -12^m$. In reality, in both cases, the supernovae are projected onto the halos of the central cD galaxies in the corresponding clusters. However, the authors rejected the possibility that they belong to these galaxies because of the large radial-velocity difference (750–2000 km s^{-1}) between the supernovae and the corresponding cD galaxies.

Assuming a modified Schechter luminosity function for the galaxies in the Virgo cluster (Trentham

*E-mail: alex@xray.sai.msu.ru

**E-mail: pk@sai.msu.ru

[1] However, with certain reservations, up to 40% of SN Ia may be peculiar (Lee *et al.* 2001), plus a significant spread of theoretical light curves (Sorokina *et al.* 2000).

and Tully 2002), the luminosity fraction of the dwarf galaxies in the clusters under study should have been less than 0.3%. If the supernova rate is proportional to the luminosity, and if the fraction of the supernovae without obvious host galaxies is on the order of 10%, this leads to a ~30-fold excess of them among such dwarf galaxies compared to high-mass galaxies. Therefore, these supernovae are believed to have exploded outside of galaxies (intergalactic supernovae) as a result of the evolution of the intergalactic stellar population. It is concluded from these observations that the fraction of the intergalactic SN Ia is 20^{+12}_{-15}%, in accordance with the theoretically expected fraction of the stars outside galaxies due to the tidal interaction between cluster galaxies. The authors themselves (Gal-Yam *et al.* 2003) point out the low statistical significance of the result obtained, and such a high percentage of the extragalactic SN Ia should be confirmed by further observations.

There is a potential channel for the formation of intergalactic supernovae through the dynamical expulsion of close WD pairs from the system of galactic globular clusters (GCs). The stellar mass fraction in the observed GCs is ~0.1% of the visible mass of the galaxies. However, dynamical interactions between stars in dense cluster cores increase the merger rate of close pairs with white dwarfs. Some of them can be expelled from the clusters during triple collisions, and the assumption that the rate of thermonuclear supernovae is proportional to luminosity for dense clusters becomes invalid. The numerical calculations of the WD evolution in open star clusters by Shara and Hurley (2002) confirmed the significant increase in the formation rate of close WD pairs through dynamical interactions.

The goal of our study was to quantitatively estimate the merger rate of double WDs in the dense cores of star clusters using the method of population synthesis of the evolution of binary stars with a semianalytical allowance made for their dynamical interactions with single stars in the cluster core. We show that the the merger rate of double WDs in GCs per average cluster star is a factor of ~3 higher than the merger rate of double WDs in spiral galaxies with continuous star formation. If ~0.3% of the baryon mass in the cluster centers is concentrated in virialized dense star clusters with masses of 10^5–$10^8 M_\odot$, then ~1% of SN Ia in the cluster centers can be naturally explained without additionally assuming the presence of 10% of the intergalactic stellar population.

THE MODEL

The Structure and Evolution of a Globular Cluster

In our calculations, we used a Michie–King model (Michie 1963) to describe the structure of the globular cluster. The stellar population was broken down into subsystems (depending on their mass), and their space density ρ_α was fitted by a power law:

$$\rho_\alpha(r) = \begin{cases} \rho_{c_\alpha}, & r \le r_{c_\alpha} \\ \rho_{c_\alpha}(r/r_{c_\alpha})^{-2}, & r_{c_\alpha} < r \le r_{h_\alpha} \\ \rho_{h_\alpha}(r/r_{h_\alpha})^{-4}, & r_{h_\alpha} < r \le r_t, \end{cases} \quad (1)$$

where r_{c_α} and r_{h_α} are, respectively, the radii of the core and the sphere within which half the mass of the α subsystem of stars is contained; and r_t is the tidal radius of the cluster. Thus, $\rho_{h_\alpha} = \rho_{c_\alpha}(r_{h_\alpha}/r_{c_\alpha})^{-2}$ and $\rho_{c_\alpha} = M_{\mathrm{tot}_\alpha} / \left[8\pi r_{c_\alpha}^2 \left(r_{h_\alpha} - \frac{2}{3} r_{c_\alpha}\right)\right]$. Under the energy equipartition condition for GC stars, we may assume that

$$r_{c_\alpha} = \sqrt{\frac{\bar{m}_c}{m_\alpha}} r_c,$$

where $\bar{m}_c$ is the mean mass of the stars in the GC core, $r_c = \sqrt{\frac{3v_m^2}{4\pi G \rho_c}}$ is the radius of the GC core, v_m is the rms space velocity, and ρ_c is the central number density of the stars:

$$\rho_c = \sum_\alpha \rho_{c_\alpha}. \quad (2)$$

The stellar velocities can be described by the truncated Maxwellian distribution

$$g(E) = \begin{cases} K e^{-\gamma J^2}[e^{-\beta E} - e^{-\beta E_t}], & E < E_t, \quad J < J_c(E) \\ 0, & E > E_t, \end{cases} \quad (3)$$

where E and J are the energy and the angular momentum (per unit mass), respectively; and $J_c(E)$ is the value of J for a star in a circular orbit with energy E, $\beta = 3/v_m^2$. Stars with $E > E_t$ are assumed to have escaped from the cluster.

Detailed calculations of the evolution of the standard model reveal a collapse of the inner core and an expansion of the outer layers. As follows from numerical calculations (see, e.g., Kim *et al.* 1998), the core contraction at late stages asymptotically approaches

a power law:

$$\rho_c(t) \sim \rho_c(0)(1 - t/t_{\rm coll})^{-1.2}, v_m(t) \sim v_m(0)(1 - t/t_{\rm coll})^{-0.12}, \quad (4)$$

where t is the current time, and $t_{\rm coll}$ is the collapse time of the cluster.

As the GC core contracts, the central number density of the stars rapidly increases, which causes the formation rate and the binding energy of binary stars to increase. Once the initial collapse has stopped, one might expect an expansion of the cluster core due to the tidal formation of binary stars. For some time, the newly forming binaries will be the energy source that maintains the expansion of the inner cluster regions. The expansion can be described by the following asymptotic formulas (see Kim *et al.* 1998):

$$\rho_c(t) \sim t^{-2}, v_m(t) \sim t^{-0.32}. \quad (5)$$

We used several GC models that differed in central density ρ_c and radius r_c at the time of the collapse. In all models, the collapse time was taken to be $t_{\rm coll} = 7 \times 10^9$ yr, the central potential was $W_0 = -\beta\phi(0) = 9$ (where $\phi(r)$ is the gravitational potential), the total number of stars was 10^6, and the fraction of the initially binary stars was assumed to be 30%.

The last two parameters specify the normalization of our calculations. For the adopted Salpeter initial mass function with a minimum mass of the forming stars of $0.1M_\odot$, the mean stellar mass in the GC is $0.38M_\odot$, and the total mass of the GC of 10^6 stars is $\sim 4\times 10^5 M_\odot$. Thus, the results presented below pertain to modeling the evolution of 3×10^5 binaries in a GC with a mass of $1.3 \times 10^5 M_\odot$.

Here, it is pertinent to take special note of the chosen 30% fraction of the initially binary stars in the GC. It follows from Hubble Space Telescope observations of GCs (Rubinstein and Bailyn 1997) that the fraction of main-sequence binary stars in the GC with a collapsed core NGC 6752 may range from 15 to 38%. In NGC 288, this fraction is estimated to be in the range of from 8 to 38% (Bellazzinni *et al.* 2002). A numerical analysis of the evolution of binaries in a GC (Fregeau *et al.* 2003) indicates that the fraction of the binaries with respect to their initial number after the core collapse ranges (depending on the cluster model) from ~0 to 35% (the table in the paper by Fregeau *et al.* 2003). This is attributable to the effective dynamical disruption of wide pairs and to the mergers of close systems. Note also that the above authors assumed up to 30% of the initially hard binaries in the GC. We chose an upper limit of $1000R_\odot$ for the initial binary semiaxes, which corresponds to the criteria by Fregeau *et al.* (2003). Thus, the high (at first glance) percentage of the initially binary systems that we adopted is not overestimated and is consistent with the available observations. Unfortunately, we cannot accurately estimate the number of newly forming binaries due to tidal captures. In any case, their percentage is much lower than the fraction of initially binary systems.

The Evolution of a Binary in a Globular Cluster

The Scenario Machine population synthesis code (Lipunov *et al.* 1996) was used to model the evolution of binary and single stars. We used the initial distributions

$$f(\log a) = \text{const}, \quad (6)$$

$$\max\left\{\begin{matrix} 10R_\odot \\ R_{\rm L}(M_1) \end{matrix}\right\} < a < 10^3 R_\odot$$

for the semimajor axes of the binaries and

$$f(M_1) \propto M_1^{-2.35}, \quad 0.1M_\odot < M_1 < 120M_\odot \quad (7)$$

for the mass of the primary component. Here, $R_{\rm L}(M_1)$ is the Roche lobe radius for the primary component. For the component mass ratio, we used a power-law distribution:

$$f(q) \propto q^{\alpha_q}, \quad q = M_2/M_1 < 1. \quad (8)$$

Here, α_q is the parameter of the distribution in component mass ratio. In our calculations, we varied it between 0 and 1.

Another important parameter of the evolution of binaries that significantly affects the results of all such calculations is the energy transfer efficiency at the common-envelope stage, $\alpha_{\rm CE}$. Having been determined both by Lipunov *et al.* (1996) and in other studies of this group, it was assumed to be $\alpha_{\rm CE} = 0.5$. This value corresponds to the (standard) value of $\alpha_{\rm CE} = 1$ in the determination used by Hurley *et al.* (2002), in which the common envelope was ejected only through the transfer of the gravitational energy of orbital motion of the approaching components to it.

When describing the dynamical interactions between cluster stars, we took into account the following processes in the code:

(1) The passages that led to changes in the orbital parameters of binaries (semimajor axis and eccentricity).

(2) The passages that led to star exchanges.

(3) The passages that led to the disruption of binaries.

(4) The interactions between single stars that led to the formation of binaries.

The corresponding cross sections σ_{ij} for these processes were numerically calculated by several authors (see Heggie *et al.* 1996; Mikkola 1984; Kim and Lee 1999).

The rate of interaction between an individual binary b at distance r from the GC center with an α subsystem of stars with a space density $n_\alpha(r)$ at time t is given by the formula

$$\mathcal{R}_{\alpha b}(t) = n_\alpha(r,t) v_m(r,t) \sigma_{\alpha b}.$$

The determination of the binary position in the GC and $\mathcal{R}$ is described in more detail in the Appendix.

To draw a change in the binding energy ΔE_b and orbital eccentricity e of a binary during the close passage of a third star, we used the following formulas for the differential interaction cross section (Heggie *et al.* 1993; Davis *et al.* 1992):

$$\frac{d\sigma}{dX} = k\pi a_0^2 \frac{X^{-\Delta}(1+X)^{-4.5+\Delta}}{V^2}, \qquad (9)$$

$$\frac{d\sigma_e}{de} \sim e, \qquad (10)$$

where $X = \Delta E_b / E_b$, and the parameter Δ depends on the relative velocity of the approaching stars. The mean value is $\langle X \rangle = 0.4$.

The change in binding energy during a triple collision results in momentum transfer to the binary barycenter. Thus, it determines the possibility of the binary being expelled from the cluster through such a collision and the distance to which the escaped binary can go before its merger.

RESULTS OF THE CALCULATIONS

Since the expulsion of merging double WDs from a cluster is directly related to the dynamical interactions between stars, one might expect the number of such systems $N^{\rm ej}_{\rm WD^2}$ in the evolution time to be determined by Γ:

$$\Gamma \propto \int \mathcal{R}_{\rm WD^2} n_{\rm WD^2} dV \sim \frac{\rho_0^2 r_c^3}{v_m} \sim \rho_0^{1.5} r_c^2, \qquad (11)$$

where the integration is over the entire GC volume.

The calculated numbers of merging WD pairs for various GC models are given in the table. We see from this table that the choice of a GC model (parameter Γ) most strongly affects precisely the number of WDs dynamically expelled from the cluster: $N^{\rm ej}_{\rm WD^2} \propto \Gamma^{0.65}$. A similar power law also follows from observations for X-ray sources in the GC. In this case, the power-law index for the X-ray sources that are associated with higher-mass binaries is close to unity: $N_{\rm X\text{-}ray} \propto \Gamma^{0.74\pm0.36}$ (Pooley *et al.* 2003).

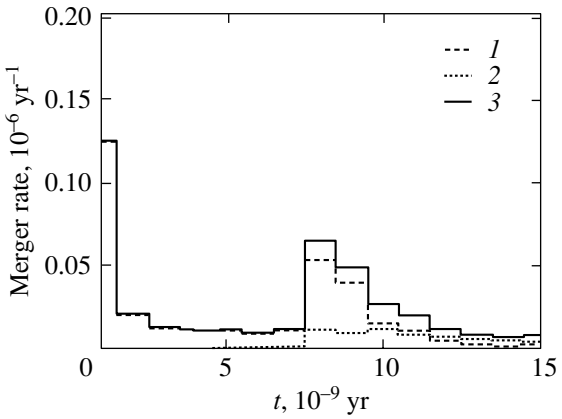

Fig. 1. Merger rate of double WDs in a GC (model C, $\alpha_q = 1$) versus time, in units of 10^{-6} yr^{-1}. The increase in merger rate at $t \sim 7 \times 10^9$ yr corresponds to an increase in Γ during the GC core collapse: *1*—for systems merging within the GC; *2*—for systems expelled from the GC; and *3*—the total merger rate of double WDs in the GC.

The merger rate of double WDs (SN Ia candidates) is plotted against time for one model (C) in Fig. 1. The increase in merger rate at time $t \sim 7 \times 10^9$ yr corresponds to a sharp increase in Γ during the evolution of the cluster (GC core collapse).

The ratio of the total number of mergers to the number of evolving binaries may serve as a character-

The number of merging double white dwarfs in a GC of 10^6 stars with a total mass of $4 \times 10^5 M_\odot$ in an evolution time of 1.5×10^{10} yr

Model	ρ_c, pc^{-3}	r_c, pc	Γ	$N_{\rm WD^2}$	$N^{\rm GC}_{\rm WD^2}$	$N^{\rm ej}_{\rm WD^2}$	ν
A	10^5	0.1	1	108	98	10	0.09
				228	216	12	0.05
B	10^5	0.3	10	120	108	12	0.10
				252	216	36	0.14
C	10^6	0.1	32	138	114	24	0.17
				330	264	66	0.20
D	10^7	0.03	90	174	132	42	0.24
				381	261	120	0.31

Note. The initial number of binaries is 3×10^5. The GC parameters are given at the time of the core collapse (7×10^9 yr). The value of Γ was normalized in such a way that $\Gamma = 1$ for model A. $N_{\rm WD^2}$ is the total number of merging double WDs over the entire evolution time; $N^{\rm GC}_{\rm WD^2}$ and $N^{\rm ej}_{\rm WD^2}$ are the numbers of merging double WDs within the GC and expelled from the GC, respectively; and ν is the fraction of the expelled merging double WDs. For each model, the results of our calculations are presented for two values of α_q: $\alpha_q = 0$ (upper rows) and $\alpha_q = 1$ (lower rows) (see formula (8)).

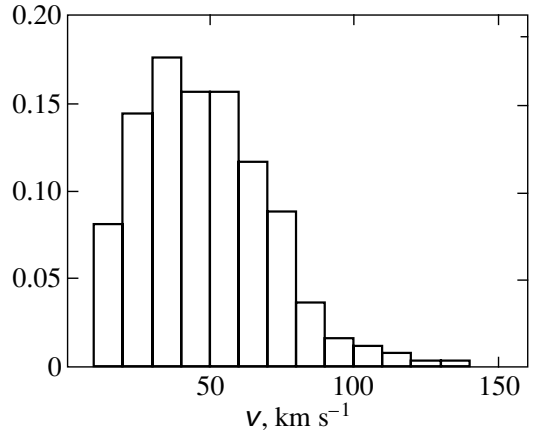

Fig. 2. Histogram (normalized to unity) illustrating the distribution of WD pairs expelled from the cluster in their barycenter velocities (model C).

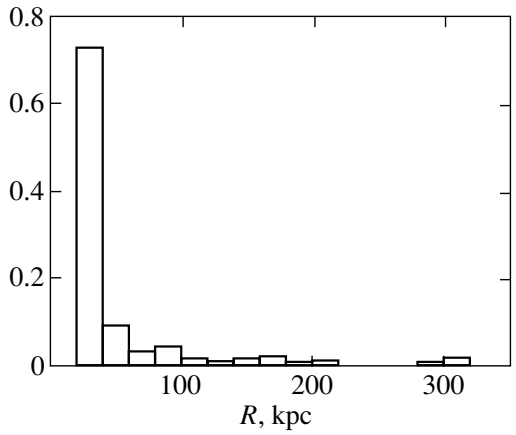

Fig. 3. Histogram (normalized to unity) illustrating the distribution of WD pairs expelled from the cluster in distance from the center of an isolated globular cluster at the time of their merger (model C).

istic of the efficiency of the merger rate of double WDs that is independent of the adopted normalization (the total number of stars in the cluster and the fraction of the initially binary stars). Taking 300 mergers per 3×10^5 binaries (table) as a typical value, we obtain an efficiency of 10^{-3} per initial binary system. This value is half the value obtained by Shara and Hurley (2002) in their numerical simulations and can be explained, in particular, by the higher efficiency of the common envelope ($\alpha_{CE} = 3$) in these numerical simulations.

Note also that the total number of merging WDs as a result of the GC evolution, N_{WD^2}, changes by a factor of only 1.5 for different GC models and is 100–500 per cluster; most (70%) of the mergers occur after the collapse of the cluster core. The mean merger rate of double WDs in the past 5 Gyr is then $\sim 10^{-13}$ per year per average cluster star, which is a factor of $\sim$3 higher than the estimated merger rate of double WDs in our Galaxy (Nelemans *et al.* 2001; Hurley *et al.* 2002).

The distributions of WD pairs expelled from the cluster in their barycenter velocities and distances from the center of the host GC are shown in Figs. 2 and 3. As we see from Fig. 2, the fraction of the stars with escape velocities of about 100 km s^{-1} is small (a few percent).

DISCUSSION

The Escape of Merging Double WDs from the System of Galactic Globular Clusters

Our Galaxy. The GC system of our Galaxy extends to distances as large as 100 kpc above the Galactic plane and has a velocity dispersion of about 150 km s^{-1} (see, e.g., the catalogs by Kukarkin (1974) and Harris (1996)). The escape velocity from the Galactic potential is $\sim$550 km s^{-1} in the Galactic plane and decreases to $\sim$100 km s^{-1} at distances of $\sim$100 kpc from the Galactic center (accurate estimates are difficult to obtain, because the form of the Galactic potential is not known at such distances). The escape of the stars expelled from the GC usually takes place at the apocenter of the cluster orbit near which the cluster is located for the longest time. Clearly, not all of the binaries expelled from the cluster will be able to escape from the host galaxy, but will remain in its halo. Thus, the total number of WD pairs escaping from the cluster gives an *upper* limit on the number of intergalactic type-Ia supernovae. The rough upper limit on the probable number of intergalactic SN Ia, $N_{SN\,Ia}$, that emerge during the mergers of double WDs expelled from the GC in a cluster of N_{gal} galaxies is

$$N_{SN\,Ia} = N_{WD^2} \times N_{GC} \times N_{gal}$$
$$\sim 100 \times 500 \times 10^3 = 5 \times 10^7$$

(N_{GC} is the number of GCs in an average galaxy). In a characteristic time of 10^{10} yr, the formation rate of SNe Ia through this channel throughout the cluster is $\sim 5 \times 10^{-3}$ per year, which is comparable to the merger rate of double white dwarfs with a total mass exceeding the Chandrasekhar limit in a *single* galaxy (Nelemans *et al.* 2001). Even this upper limit is an order of magnitude smaller than the high fraction of the extragalactic SNe Ia deduced from observations.

Dwarf elliptical galaxies. We may also assume that dwarf elliptical dE galaxies (the fraction of which in a cluster can be significant) with a mass of up to $M \sim 10^8 M_\odot$ are the main source of observed intergalactic supernovae. The central number densities of

the stars in such galaxies are comparable to those in dense GC cores. The escape velocity from a cluster at a constant star space density is $v_e \propto M^{1/3}$. Therefore, applying our calculations to a system of 10^8 stars, we find that the number of escaping WD pairs from this system is $10^8/10^6 \times f(> v_e) \times 100 \sim 100$ (in this estimate, the fraction of the binaries with barycenter velocities higher than the escape velocity from the cluster, $v_e \sim 100$ km s^{-1}, was taken to be $f(> v_e) \sim 1/100$), which is also insufficient to explain the truly intergalactic supernovae.

cD galaxies. Let us now turn to the central cD galaxy as the source of intergalactic supernovae. Although SN 1998fc in Abell 403 and SN 2001al in Abell 2122/4 are projected onto the halos of the central cD galaxies (the projected distance is 160 kpc), we rule out the possibility that they belong to these galaxies because of the radial-velocity difference (Gal-Yam *et al.* 2003). The giant elliptical galaxies in the cluster centers are known to have a huge system of globular clusters (up to 10 000). Using the results obtained in our calculations ($\sim$300 mergers of double WDs in cluster cores and $\sim$100 merging pairs escaped after the core collapse), we obtain an average estimate of the maximum SN Ia rate due to the WD evolution in the GC in projection onto the halo of the cD galaxy, $400 \times 10^4/(5 \times 10^9) \sim 10^{-3}$ per year. Only a few percent of such double WDs can have barycenter velocities high enough to escape from the galaxy; they cannot explain the observations.

The Mergers of Double WDs in Virialized Star Clusters at the Centers of Galaxy Clusters

Is there an alternative explanation for the observations by Gal-Yam *et al.* (2003) that does not appeal for the evolution of 10–20% of the stars outside galaxies? In our view, the most plausible explanation for intergalactic supernovae is the merger of WD pairs in a virialized system of star clusters in the central regions of galaxy clusters. It follows from observations of the central parts of the Virgo cluster and from simulations (see the recent review article by Lee (2002) and references therein) that a huge system of blue GCs with a large velocity dispersion must be formed during the formation of giant elliptical galaxies. Recent observations of intergalactic (up to 250 kpc from the center) GCs in the nearby Hydra I and Centaurus clusters (Hilker 2002) lead to a similar conclusion. An enhanced density of star clusters in the central regions of galaxy clusters naturally arises during the merger of the galaxies that form giant cD galaxies as well as through the tidal capture of the GC system of the galaxies that pass near the cluster center. Assuming that 0.3% of the luminosity (and the baryon mass) in the cluster centers is concentrated in dense collapsed stellar structures and taking into account the threefold increase in the merger rate of double WDs in such clusters, we naturally obtain $\sim$1% of the observed SN Ia rate *outside* the visible host galaxies. Thus, this model predicts the existence of faint ($\langle M_R \rangle \sim -10^m$) *host clusters* for SN Ia. It is hoped that the purposeful search for type-Ia supernovae being conducted at present as part of various projects (see, e.g., Tonry *et al.* 2003) will improve the existing statistics and will reveal the faint host galaxies and astrophysical sources of intergalactic SN Ia. The absence of host clusters with $M_R > -8^m \ldots -10^m$ may serve as a critical argument for choosing the model of intergalactic type-Ia supernovae from intergalactic stars.

CONCLUSIONS

We have considered a possible formation channel of intergalactic SN Ia during the mergers of double white dwarfs that evolve and are expelled from dense star clusters (GCs, the nuclei of dwarf elliptical galaxies, etc.) when they dynamically interact with a third star (triple collisions). The population synthesis method was used to model the formation and evolution of close double white dwarfs in cluster cores by taking into account the time evolution of their physical parameters and to calculate the rates of escape of such objects from clusters. We obtained their distributions in escape velocities from clusters, in merger rates, and in distances from the host cluster after escape. We showed that the mean merger rate of double WDs after core collapse could reach $\sim 10^{-13}$ per year per average GC star. In a typical GC, the number of expelled WD pairs after the GC core collapse is $\sim$100. For a galaxy cluster with several thousand members, this estimate yields a formation rate of intergalactic thermonuclear supernovae <0.005 per year, which is much lower than the observed high rate of intergalactic supernovae of this type. We hypothesize that the possible observed high percentage of intergalactic SN Ia without any obvious host galaxies can be explained in part by the evolution of double WDs in dense star clusters. A system of such clusters naturally arises near the center of galaxy clusters during the formation of giant elliptical galaxies and, subsequently, during the tidal interaction between the galaxies that pass near the cluster center. This hypothesis can be verified through observations of the faint host clusters of SN Ia in nearby galaxy clusters.

ACKNOWLEDGMENTS

We wish to thank A.S. Rastorguev and O.K. Sil'chenko for their helpful discussions and L.R Yungel'son for his valuable remarks. This work was supported by the Russian Foundation for Basic Research (project nos. 03-02-16110a and 03-02-06733mas).

APPENDIX

The Position of a Binary in a Globular Cluster

The relative motions of stars in a GC produce continuous fluctuations of the gravitational field. In turn, these fluctuations cause the magnitude and direction of the velocity of each star to change. As a result, the energy $E = v^2/2 + \phi(r)$ and the angular momentum $J = r \times v_t$ of the star will change. When calculating each evolutionary track, the changes in these parameters in a time interval Δt due to the gravitational interaction with the surrounding stars can be calculated using the formula

$$\Delta E = n\epsilon_1 + n^{1/2} y_1 \epsilon_2^2,$$
$$\Delta J = n j_1 + n^{1/2} y_2 j_2^2,$$
$$\Delta t = nP(E, J),$$

where y_1 and y_2, the random numbers drawn from a normal distribution with a mean $\langle y_1 \rangle = \langle y_2 \rangle = 0$ and a variance $\langle y_1^2 \rangle = \langle y_2^2 \rangle = 1$, are chosen from the correlation condition in such a way that

$$\langle y_1 y_2 \rangle = \xi^2 / \epsilon_2 j_2.$$

We used a method with averaging over the orbit similar to the method by Shapiro and Marchant (1978) and Marchant and Shapiro (1979) to determine the coefficients ϵ_1, $j_{1,2}$, and ξ:

$$\epsilon_1 = 2 \int_{r_\mathrm{p}}^{r_\mathrm{a}} \langle \Delta E \rangle dr / v_r,$$
$$\epsilon_2^2 = 2 \int_{r_\mathrm{p}}^{r_\mathrm{a}} \langle \Delta E^2 \rangle dr / v_r,$$
$$j_1 = 2 \int_{r_\mathrm{p}}^{r_\mathrm{a}} \langle \Delta J \rangle dr / v_r,$$
$$j_2^2 = 2 \int_{r_\mathrm{p}}^{r_\mathrm{a}} \langle \Delta J^2 \rangle dr / v_r,$$
$$\xi^2 = 2 \int_{r_\mathrm{p}}^{r_\mathrm{a}} \langle \Delta E \Delta J \rangle dr / v_r.$$

Here, r_p and r_a are the pericenter and apocenter of the stellar orbit in the cluster. These coefficients are the mean rates of change in E and J due to several approaches over the orbital period and the mean cumulative values over the orbital period.

The diffusion coefficients that contain E and J can be expressed in terms of $\langle \Delta v_{||} \rangle, \langle \Delta v_{||}^2 \rangle$ and $\langle (\Delta v_\perp)^2 \rangle$—the locally calculated velocity diffusion coefficients:

$$\langle \Delta E \rangle = v \langle \Delta v_{||} \rangle + \frac{1}{2} \langle \Delta v_\perp^2 \rangle + \frac{1}{2} \langle \Delta v_{||}^2 \rangle,$$
$$\langle \Delta E^2 \rangle = v^2 \langle \Delta v_{||}^2 \rangle,$$
$$\langle \Delta J \rangle = \frac{J}{v} \langle \Delta v_{||} \rangle + \frac{r^2}{4J} \langle \Delta v_\perp^2 \rangle,$$
$$\langle \Delta J^2 \rangle = \frac{J^2}{v^2} \langle \Delta v_{||}^2 \rangle + \frac{1}{2} (r^2 - \frac{J^2}{v^2}) \langle \Delta v_\perp^2 \rangle,$$
$$\langle \Delta E \Delta J \rangle = J \langle \Delta v_{||}^2 \rangle.$$

For a Maxwellian velocity distribution of the field stars, the diffusion coefficients reduce to standard form (Spitzer 1987):

$$\langle \Delta v_{||} \rangle = -2 \left(1 + \frac{m}{m_f} \right) n_f \Gamma k^2 G(x),$$
$$\langle (\Delta v_{||})^2 \rangle = 2 n_f \Gamma k \frac{G(x)}{x},$$
$$\langle (\Delta v_\perp)^2 \rangle = 2 n_f \Gamma k \frac{\Phi(x) - G(x)}{x},$$

where $\Phi(x)$ is the error function

$$\Phi(x) = \frac{2}{\pi^{1/2}} \int_0^x \exp -y^2 dy$$

and

$$G(x) \equiv \frac{\Phi(x) - x\Phi'(x)}{2x^2}.$$

Using E and J, we can determine the orbital parameters of the star within the GC: the orbital period

$$P(E, J) = 2 \int_{r_\mathrm{p}}^{r_\mathrm{a}} dr / v_r,$$

the pericenter r_p and the apocenter r_a of the stellar orbit in the cluster from the condition

$$v_r^2 = 2E - 2\phi(r) - J^2/r^2 = 0.$$

The rate of interaction between a binary b and an α subsystem of stars at time t is given by the formula

$$\mathcal{R}_{\alpha b}(t) = \sigma_{\alpha b} \times \frac{2}{P(E, J)} \int_{r_\mathrm{p}}^{r_\mathrm{a}} n_\alpha(r, t) v(r, t) / v_r dr.$$

REFERENCES

1. M. Bellazzinni, P. F. Fusi, P. Montegriffo, *et al.*, Astron. J. **123**, 2541 (2002).
2. E. Capellaro, M. Turatto, D. Yu. Tsvetkov, *et al.*, Astron. Astrophys. **322**, 431 (1997).
3. N. N. Chugai and L. R. Yungel'son, Pis'ma Astron. Zh. **30**, 83 (2004); astro-ph/0308297 (2003).
4. N. V. Dunina-Barkovskaya, V. S. Imshennik, and S. I. Blinnikov, Pis'ma Astron. Zh. **27**, 412 (2001) [Astron. Lett. **27**, 353 (2001)].
5. M. B. Davis, W. Benz, and J. G. Hills, Astrophys. J. **424**, 870 (1994).
6. J. M. Fregeau, M. A. Gurkan, K. J. Joshi, and F. A. Rasio, Astrophys. J. (in press); astro-ph/0301521 (2003).
7. M. Hamuy, M. M. Phillips, N. B. Suntzeff, *et al.*, Nature (in press); astro-ph/0306270 (2003).
8. W. E. Harris, Astron. J. **112**, 1487 (1996).
9. D. C. Heggie, C. Douglas, and P. Hut, Astrophys. J., Suppl. Ser. **85**, 347 (1993).
10. D. C. Heggie, P. Hut, and S. L. W. McMillan, Astrophys. J. **467**, 359 (1996).
11. M. Hilker, astro-ph/0210466 (2002).
12. F. Hoyle and W. A. Fauler, Astrophys. J. **132**, 565 (1960).
13. J. R. Hurley, C. A. Tout, and O. R. Pols, Mon. Not. R. Astron. Soc. **329**, 897 (2002).
14. I. Iben, Jr. and A. V. Tutukov, Astrophys. J., Suppl. Ser. **54**, 355 (1984).
15. A. Gal-Yam, D. Maoz, P. Guhathakurta, and A. V. Filippenko, Astron. J. **125**, 1087 (2003).
16. S. S. Kim and H. M. Lee, Astron. Astrophys. **347**, 123 (1999).
17. S. S. Kim, H. M. Lee, and J. Goodman, Astrophys. J. **495**, 786 (1998).
18. B. V. Kukarkin, *Globular Star Clusters* (Nauka, Moscow, 1974) [in Russian].
19. M. G. Lee, J. Korean Astron. Soc. **35**, 1 (2002).
20. W. Lee, A. V. Filippenko, R. R. Treffers, *et al.*, Astrophys. J. **546**, 734 (2001).
21. V. M. Lipunov, K. A. Postnov, and M. E. Prokhorov, Astrophys. Space Sci. Rev. **9**, 1 (1996).
22. M. Livio and A. Riess, submitted to the Astrophys. J.; astro-ph/0308018.
23. A. B. Marchant and S. L. Shapiro, Astrophys. J. **234**, 317 (1979).
24. R. W. Michie, Mon. Not. R. Astron. Soc. **125**, 127 (1963).
25. S. Mikkola, Mon. Not. R. Astron. Soc. **208**, 75 (1984).
26. R. Napiwotzki, N. Christlieb, H. Drechsel, *et al.*, Messenger **112**, 25 (2003).
27. G. Nelemans, L. R. Yungelson, S. F. Portegies Zwart, and F. Verbunt, Astron. Astrophys. **365**, 491 (2001).
28. K. Nomoto, Astrophys. J. **253**, 798 (1982).
29. S. Perlmutter, G. Albering, G. Goldhaber, *et al.*, Astrophys. J. **517**, 565 (1999).
30. D. Pooley, W. H. Lewin, S. F. Anderson, *et al.*, Astrophys. J. **591**, 131 (2003).
31. A. G. Riess, A. V. Filippenko, P. Challis, *et al.*, Astron. J. **116**, 1009 (1998).
32. E. P. Rubinstein and C. D. Bailyn, Astrophys. J. **474**, 701 (1997).
33. S. L. Shapiro and A. B. Marchant, Astrophys. J. **225**, 603 (1978).
34. M. M. Shara and J. R. Hurley, Astrophys. J. **571**, 830 (2002).
35. E. I. Sorokina, S. I. Blinnikov, and O. S. Bartunov, Pis'ma Astron. Zh. **26**, 90 (2000) [Astron. Lett. **26**, 67 (2000)].
36. L. Spitzer, Jr., *Dynamical Evolution of Globular Clusters* (Princeton Univ. Press, Princeton, 1987; Mir, Moscow, 1990).
37. J. L. Tonry, B. P. Schmidt, B. Barris, *et al.*, Astrophys. J. (in press); astro-ph/0305008 (2003).
38. N. Trentham and R. B. Tully, Mon. Not. R. Astron. Soc. **335**, 712 (2002).
39. S. van den Berg, Li Weidong, and A. Filippenko, Publ. Astron. Soc. Pac. (in press); astro-ph/0308195 (2003).
40. R. F. Webbink, Astrophys. J. **277**, 355 (1984).
41. J. Whelan and I. Iben, Jr., Astrophys. J. **186**, 1007 (1973).

Translated by V. Astakhov

Astronomy Letters, Vol. 30, No. 3, 2004, pp. 148–158. Translated from Pis'ma v Astronomicheskiĭ Zhurnal, Vol. 30, No. 3, 2004, pp. 173–184.

Stars of Extragalactic Origin in the Solar Neighborhood

T. V. Borkova* **and V. A. Marsakov****

Rostov State University, pr. Stachki 194, Rostov-on-Don, 344104 Russia

Received July 1, 2003

Abstract—For 77 main-sequence F–G stars in the solar neighborhood with published iron, magnesium, and europium abundances determined from high-dispersion spectra and with the ages estimated from theoretical isochrones, we calculated the spatial velocities using Hipparcos data and the Galactic orbital elements. A comparison with the orbital elements of the globular clusters that are known to have been accreted by our Galaxy in the past reveals stars of extragalactic origin. We show that the abundance ratios of r- and α-elements in all the accreted stars differ sharply from those in the stars that are genetically associated with the Galaxy. According to current theoretical models, europium is produced mainly in low-mass type-II supernovae (SNe II), while magnesium is synthesized in large quantities in high-mass SN II progenitors. Since all the old accreted stars of our sample exhibit a significant Eu overabundance relative to Mg, we conclude that the maximum masses of the SN II progenitors outside the Galaxy were much lower than those inside it. On the other hand, only a small number of young accreted stars exhibit low negative ratios $[\mathrm{Eu/Mg}] < 0$. This can be explained by the delay of primordial star formation and the explosions of high-mass SNe II in a relatively small part of extragalactic space. We provide evidence that the interstellar medium was weakly mixed at the early evolutionary stages of the Galaxy formed from a single protogalactic cloud, and that the maximum mass of the SN II progenitors increased in it with time simultaneously with the increase in mean metallicity.

Key words: *stellar chemical composition, Galactic subsystems, accreted stars.*

INTRODUCTION

In recent years, observational astronomy has provided compelling evidence that not all of the stars that currently belong to our Galaxy were formed from a single protogalactic cloud. Some of the stellar objects were captured by the Galaxy at different times from the nearest satellite galaxies. The epoch of accretion of isolated protogalactic fragments and extragalactic objects probably began at the earliest formation stages of the Galaxy and is still going on. In particular, we are currently observing the disruption of a dwarf spherical galaxy in Sagittarius (dSph Srg) by tidal forces from the Galaxy (Ibata *et al.* 1994; Mateo 1996). Four globular clusters are confidently associated with this galaxy: M 54, Arp 2, Ter 8, and Ter 7. The cluster Pal 12 is far from this galaxy, but, according to the accurately reconstructed orbits of the two stellar systems, it was expelled from Srg about one and a half billion years ago (Dinescu *et al.* 2000). The massive globular cluster M 54 is generally believed to be the nucleus of the system (Larson 1996). In addition, it is highly likely that five more globular clusters belong to the Srg system: M 53, Pal 5, NGC 4147, NGC 5053, and NGC 5634 (Dinescu *et al.* 2000; Palma and Majewski 2002; Bellazini and Ferraro 2003). The galactic orbital elements of the clusters Rup 106, Pal 13, NGC 5466, NGC 6934, and NGC 7006 also suggest that they were captured from various satellite galaxies (Dinescu *et al.* 2000, 2001). Freeman (1993) assumed that even ω Cen (the largest known globular cluster in the Galaxy), which is close to the Galactic center and has a retrograde orbit, was the nucleus of a dwarf galaxy in the past. Tshuchiya *et al.* (2003) showed, through numerical simulations, that the disruption of a dwarf satellite by tidal forces from the Galaxy and the emergence of its central cluster in the Galaxy in a highly eccentric orbit are quite possible. All of the globular clusters whose extragalactic origin has been established solely from their spatial positions and velocities exhibit redder horizontal branches than do most of the Galactic clusters with a similar metallicity. If we assume, as was previously done (Borkova and Marsakov 2000), that all of the low-metallicity globular clusters with anomalous morphology of their horizontal branches are extragalactic in origin, then there will be a factor of 1.5 more such clusters than there are low-metallicity clusters in the protodisk halo, i.e., those formed from the single protogalactic cloud. Therefore,

*E-mail: borkova@ip.rsu.ru
**E-mail: marsakov@ip.rsu.ru

accreted stellar objects constitute the bulk of the Galactic halo.

The theory of dynamical evolution predicts the inevitable dissipation of clusters through the combined actions of two-body relaxation, tidal destruction, and collisional interactions with the Galactic disk and bulge (see, e.g., Gnedin and Ostriker 1990). Indeed, traces of the tidal interaction with the Galaxy in the shape of extended deformations (tidal tails) have been found in all the clusters for which high-quality optical images were obtained (Leon *et al.* 2000). The latter authors even established for ω Cen that, after the last passage through the plane of the disk, this cluster lost, in the form of stars, slightly less than one percent of its mass. Thus, even in the nearest solar neighborhood, we may attempt to identify stars of extragalactic origin and to find possible differences in the abundances of heavy elements between them and the stars genetically associated with the entire Galaxy.

All of the chemical elements heavier than boron are currently believed to have been synthesized in stars of various masses. According to the scenario suggested by Tinsley (1979), the presently observed lowest-metallicity stars were formed from an interstellar medium enriched with the elements ejected by high-mass ($M > 10M_\odot$) asymptotic-giant-branch (AGB) stars and with the elements produced during their subsequent explosions as type-II supernovae (SNe II). The characteristic explosion time of SNe II after their formation is about 30 Myr. These events inject α- and r-elements and a few iron-peak elements. However, the production of the bulk of the iron began about one billion years after a burst of star formation, when stars with masses of $6{-}8M_\odot$ that were members of close binaries evolved and exploded as SNe Ia. The onset of the SN Ia explosion phase roughly coincides with the onset of the formation of a thick-disk subsystem. Since the contribution of SNe Ia to the synthesis of iron-peak elements is larger than their contribution to the synthesis of α-elements, the ratio characteristic of low-metallicity stars, $[\alpha/\mathrm{Fe}] \approx 0.4$, decreases to zero when going from $[\mathrm{Fe/H}] \approx -1.0$ (the lowest-metallicity thick-disk stars) to solar-metallicity stars (Edvardsson *et al.* 1993; Furmann 1998). The abundance of europium, an element produced in the r-process, behaves similarly: the value of $[\mathrm{Eu/Fe}] \approx 0.5$ typical of low-metallicity stars decreases with increasing metallicity, starting from $[\mathrm{Fe/H}] \approx -1$. Both processes take place in stars whose final evolutionary stage is an SN II explosion, but the predominant yield of elements in different processes depends on the stellar mass.

Recent studies have revealed field stars that do not follow this scenario of enrichment with α- and r-elements. Thus, in particular, Carney *et al.* (1997), King (1997), and Hanson *et al.* (1998) discovered low-metallicity stars with an $[\alpha/\mathrm{Fe}]$ ratio much smaller than its expected value. Likewise, Barris *et al.* (2000), Mashonkina (2003), and Mashonkina *et al.* (2003) found halo stars with anomalous abundances of r-elements. In other words, there is a significant spread in the relative elemental abundances of the two processes among stars with $[\mathrm{Fe/H}] < -1.0$. The nature of this spread has not yet been completely established, because various scenarios for the enrichment of the interstellar medium with chemical elements can be realized both in isolated protogalactic fragments inside a single protogalactic cloud and in independent companion galaxies. Here, we make an attempt to solve this question by analyzing a sample of 77 nearby stars for which reliable stellar parameters (including the abundances of certain chemical elements, ages, etc.) and their galactic orbital elements have been determined from high-quality observational data.

OBSERVATIONAL DATA AND STELLAR PARAMETERS

We took the initial sample from the doctoral dissertation by Mashonkina (2003). It includes 77 nearby main-sequence F–G stars (we excluded one star, because no radial velocity was available for it). Most of these (66 stars) were selected from the lists by Furmann (1998, 2003). Eleven more stars with $[\mathrm{Fe/H}] < -1.0$ were specially studied by Mashonkina to extend the list toward halo stars. Since the lifetime of the stars in this spectral range on the main sequence is several billion years, among them are also some of the oldest stars of the Galaxy. In all cases, spectra with a high spectral resolution (up to $\lambda/\Delta\lambda \approx 60\,000$) and a high signal-to-noise ratio (up to $\mathrm{S/N} \approx 200$) were used. Each star was observed at least twice.

All the fundamental physical parameters of the stars (T_{eff}, $\log g$, [Fe/H], etc.) were determined from the same observational data. The effective temperatures were estimated from Balmer line profiles with an error of $\varepsilon T_{\mathrm{eff}} = \pm 80$ K. The gravities that were determined by analyzing the profiles of strong magnesium lines were almost equal to those determined from Hipparcos trigonometric parallaxes, and the error was $\varepsilon \log g = \pm 0.1$. The sample includes only stars with $\log g \geq 3.5$. The values of [Fe/H] were determined with an error of ± 0.10 dex. The accuracy of the above parameters strongly affects the abundance estimates for various elements. The uncertainty in the [Mg/Fe] ratio (the surrogate of $[\alpha/\mathrm{Fe}]$) is ± 0.10 dex. Mashonkina determined the relative non-LTE abundances [Eu/Fe] (the surrogate of r-elements) with an

error of ±0.10 dex. Bernkoff *et al.* (2001) estimated the ages of the stars from the isochrones by VandenBerg (1992) and VandenBerg *et al.* (2000) by taking into account the peculiar heavy-element abundances in each star. For several thick-disk subgiants, the age was determined with an accuracy of about ±1 Gyr. Since the uncertainty in the ages of main-sequence stars can reach 2 or 3 Gyr, the individual age estimates for these stars should be treated with caution and should be used only in the statistical sense.

For all of the sample stars, we calculated the distances and spatial velocity components using the Hipparcos catalog and the radial-velocity catalog by Barbier-Brossat and Figon (2000). The galactic orbital elements were calculated using a multicomponent model of the Galaxy that consisted of a disk, a bulge, and an extended massive halo (Allen and Santillan 1991). We assumed that the Galactocentric distance of the Sun was 8.5 kpc, the Galactic rotation velocity at the solar Galactocentric distance was 220 km s^{-1}, and the velocity of the Sun with respect to the local centroid was $(U_\odot, V_\odot, W_\odot) = (-10, 10, 6)$ km s^{-1}. A list of stars with all the parameters calculated and used here is given in the table.

Despite the small size of our sample, it contains representatives of all the Galactic subsystems (except the bulge). Its representativeness is slightly violated by the fact that the low-metallicity stars were chosen from a larger volume of space to compensate for their scarcity in the solar neighborhood, which is attributable to the high velocities of these stars (particularly their W component). However, even a few stars with [Fe/H] < -1.0 (22 stars) can reveal some of the global patterns of their behavior because of the high accuracy of the parameters obtained for them.

CRITERIA FOR SEPARATING THIN- AND THICK-DISK STARS

While analyzing the properties of F–G dwarfs from his sample, Furmann (1998) found that the Mg abundance relative to iron increased abruptly when going from the thin disk to the thick disk. This author clearly showed that there was a gap in ages of about 2 or 3 Gyr between these subsystems. The existence of a delay in star formation in the Galaxy prior to the formation of the Galactic thin-disk subsystem was first pointed out by Marsakov and Suchkov (1977). Since the thin-disk stars are known to have low peculiar velocities relative to the local standard of rest ($V_{\rm pec}$), we separated this subsystem using two criteria: $t \le 9$ Gyr and $V_{\rm pec} \le 100$ km s^{-1}. A comparison of Figs. 1a and 1b indicates that these two criteria automatically separate stars with [Mg/Fe] ≤ 0.25 (except one thick-disk star that fell within this range). In the [Fe/H]–[Mg/Fe] diagram, we clearly see a gap of Δ[Mg/Fe] ≈ 0.1 between the stars of the two disk subsystems. However, we also simultaneously see a mutual overlapping of the ranges both in metallicity and in residual velocities (and, hence, in orbital sizes). In other words, [Fe/H] and $V_{\rm pec}$ here are less suitable criteria for the individual separation of the stars of these subsystems from one another.

Objectively, thick-disk stars are much more difficult to separate from the protodisk-halo stars genetically associated with them. The ages of most of the stars that do not belong to the thin disk lie within a narrow time interval, and we can say nothing about the difference between the formation epochs of these subsystems because of the errors in its determination. However, based on an abundance analysis, Mashonkina *et al.* (2003) concluded that, although the time intervals of these subsystems overlap, star formation in the thick disk began about 1 Gyr later than in the halo. The subsystems can be separated according to the value [Fe/H] ≈ -1.0. Indeed, the metallicity distributions for the globular clusters near this point exhibit a large deficit of stars (Borkova and Marsakov 2000), while the RR Lyrae field stars show a distinct inflection (Borkova and Marsakov 2002). In this case, however, a number of stars with circular orbits characteristic of the disk subsystem fall into the halo. Here, we decided to use the peculiar velocity as the criterion. If we separate the sample stars by $V_{\rm pec} \approx 155$ km s^{-1}, then only one star with [Fe/H] > -1.0 will be in the halo, and two low-metallicity stars will be in the thick disk. Such stars in the thick disk are commonly called a low-metallicity tail.

THE PROTODISK- AND ACCRETED-HALO SUBSYSTEMS

There is no unique necessary and sufficient statistical criterion that would serve to separate extragalactic objects. In each specific case, all the available parameters must be considered simultaneously. To stratify the field stars into halo subsystems, different authors have primarily used such parameters as the retrogradation of their orbits and their distances from the Galactic center and plane. Naturally, the thick-disk objects must first be removed from the sample (see above). The galactic orbital elements of the stars, their ages, and the abundances of the α-elements in them have been most commonly used as additional criteria (for an overview of the criteria, see the monograph by Carney 1999). For globular clusters, the morphology of their horizontal branches has proven to be a good criterion (see, e.g., Borkova and Marsakov 2000). Thus, it has been shown

Chemical composition and galactic orbital elements of the nearest field stars

HD/BD	[Fe/H], dex	[Mg/Fe], dex	[Eu/Fe], dex	U, km s^{-1}	V, km s^{-1}	W, km s^{-1}	V_{pec}, km s^{-1}	R, kpc	Z_{max}, kpc	e	Code
400	−0.25	0.08	0.12	−27.2	−9.2	−8.4	37.2	9.7	0.0	0.12	1
3795	−0.64	0.39	0.56	50.4	−88.9	45.6	102.6	8.8	0.9	0.37	2
4614	−0.30	0.09	0.11	29.9	−10.0	−16.8	22.6	9.1	0.1	0.06	1
9407	0.03	0.01	−0.06	−50.4	−2.0	1.4	61.3	10.9	0.1	0.20	1
10 519	−0.64	0.43	0.38	96.5	−77.6	29.3	115.3	9.8	0.6	0.40	2
10 697	0.10	0.00	−0.08	−36.0	−27.5	16.2	54.0	9.4	0.3	0.17	1
18 757	−0.28	0.32	0.25	68.6	−79.2	−27.7	93.3	9.1	0.3	0.36	2
19 445	−1.99	0.47	–	−157.2	−122.0	−67.1	210.8	12.4	1.6	0.67	3
22 879	−0.86	0.44	0.42	108.9	−86.0	−44.8	130.7	10.1	0.6	0.45	2
25 329	−1.84	0.42	0.24	40.2	−189.0	19.9	183.9	8.6	4.4	0.85	3
29 907	−1.55	0.29	0.63	381.2	−142.0	27.8	395.7	44.8	3.0	0.94	4
30 649	−0.47	0.35	0.32	58.5	−80.6	−9.6	85.7	8.9	0.0	0.35	2
30 743	−0.45	0.14	0.13	−25.8	−5.4	−23.6	40.1	9.9	0.2	0.12	1
31 128	−1.49	0.34	0.44	59.4	−97.1	−26.1	102.1	8.9	0.3	0.42	2
34 328	−1.61	0.38	0.27	207.7	−352.0	95.6	407.9	15.4	4.7	0.67	4
37 124	−0.44	0.32	0.30	−28.7	−46.5	−43.7	65.2	9.0	0.6	0.20	2
43 042	0.04	0.00	−0.02	32.5	−18.4	−16.6	26.2	8.9	0.1	0.08	1
45 282	−1.52	0.37	0.60	245.8	−186.0	−43.7	297.0	15.9	8.2	0.91	4
52 711	−0.16	0.04	0.05	18.5	−77.5	−9.2	68.1	8.5	0.0	0.31	1
55 575	−0.36	0.17	0.20	79.5	−1.8	32.1	79.7	11.5	0.7	0.23	1
58 855	−0.32	0.12	–	−25.4	−15.1	−4.2	35.8	9.4	0.0	0.12	1
59 392	−1.59	0.27	0.68	−123.0	−325.0	−32.3	343.5	10.6	0.4	0.67	4
61 421	−0.01	0.06	0.01	−5.4	−8.3	−18.8	20.1	9.0	0.2	0.05	1
62 301	−0.69	0.30	0.36	5.5	−108.0	−23.4	100.1	8.5	0.2	0.45	2
64 606	−0.89	0.37	0.47	82.4	−65.2	1.4	91.3	9.5	0.1	0.33	2
65 583	−0.73	0.39	0.46	12.0	−88.6	−30.9	82.5	8.5	0.3	0.36	2
67 228	0.12	0.00	−0.13	−32.8	4.1	−15.9	46.1	10.7	0.1	0.15	1
68 017	−0.40	0.34	0.28	48.1	−60.4	−39.6	71.5	8.8	0.5	0.25	2
69 611	−0.60	0.43	0.36	38.3	−144.0	−43.4	142.4	8.6	0.6	0.62	2
74 000	−2.00	0.35	0.16	−245.7	−362.0	59.5	440.3	21.1	2.7	0.77	4
84 937	−2.07	0.36	–	−224.5	−238.0	−8.3	327.7	15.3	10.1	0.99	4
90 508	−0.33	0.22	0.26	−21.0	−94.2	22.4	94.1	8.7	0.4	0.39	2
97 320	−1.18	0.36	0.40	−73.1	−20.0	−37.5	89.4	11.0	0.5	0.27	2
99 383	−1.54	0.37	0.40	23.2	−204.0	129.0	237.1	8.9	7.3	0.79	3
102 158	−0.46	0.40	0.34	114.4	−118.0	10.1	151.5	9.9	0.2	0.57	2
102 200	−1.24	0.30	0.57	−86.5	−131.0	6.4	155.5	9.5	0.2	0.61	3
103 095	−1.35	0.28	0.55	−278.0	−160.0	−13.4	325.3	21.8	0.2	0.90	4
109 358	−0.21	0.07	–	30.8	−3.3	1.5	23.1	9.4	0.1	0.07	1
112 758	−0.43	0.36	0.28	75.7	−34.1	16.4	73.5	9.8	0.3	0.23	2
114 710	−0.03	0.01	0.01	50.6	8.7	8.5	47.0	10.9	0.2	0.16	1
114 762	−0.71	0.33	–	82.0	−70.5	57.8	113.6	9.5	1.3	0.34	2

Contd.

HD/BD	[Fe/H], dex	[Mg/Fe], dex	[Eu/Fe], dex	U, km s^{-1}	V, km s^{-1}	W, km s^{-1}	V_{pec}, km s^{-1}	R, kpc	Z_{max}, kpc	e	Code
117 176	−0.11	0.08	0.04	−13.7	−51.7	−3.8	48.0	8.6	0.0	0.20	1
121 560	−0.43	0.15	0.14	29.2	−20.1	−3.1	21.9	8.8	0.0	0.08	1
122 196	−1.71	0.16	0.24	171.8	−143.0	14.0	210.8	11.5	0.3	0.73	3
126 053	−0.35	0.14	0.14	−22.4	−15.2	−39.3	46.7	9.3	0.5	0.11	1
130 322	0.04	0.02	−0.04	9.4	−26.0	−11.0	16.8	8.5	0.1	0.07	1
132 142	−0.39	0.31	0.26	108.4	−55.9	19.6	111.6	10.5	0.4	0.37	2
134 987	0.25	0.00	−0.17	20.5	−40.2	20.8	41.7	8.5	0.3	0.14	1
142 373	−0.57	0.22	0.23	41.8	10.4	−68.2	72.8	11.3	1.3	0.16	1
144 579	−0.69	0.38	0.46	35.5	−58.2	−18.0	55.8	8.6	0.1	0.23	2
148 816	−0.78	0.41	0.30	−86.5	−262.0	−79.2	280.4	9.7	5.4	0.89	4
157 214	−0.34	0.38	0.34	−26.1	−80.4	−63.8	97.9	8.7	1.1	0.32	2
168 009	−0.03	0.04	−0.08	4.4	−61.7	−22.5	54.5	8.5	0.2	0.24	1
176 377	−0.27	0.07	–	38.5	−23.7	−4.7	31.7	8.9	0.0	0.11	1
179 957	−0.01	0.05	0.03	67.2	−44.0	35.5	78.4	9.4	0.7	0.23	1
179 958	0.02	0.05	0.00	66.6	−40.6	36.6	77.2	9.5	0.7	0.22	1
184 499	−0.51	0.40	0.33	64.6	−162.0	58.5	174.1	8.9	1.3	0.71	3
186 408	0.06	0.01	–	−18.1	−29.3	−0.1	34.6	8.9	0.1	0.13	1
187 691	0.07	0.03	−0.02	2.7	−2.7	−25.0	21.6	9.2	0.2	0.04	1
187 923	−0.17	0.21	0.13	−35.7	−51.7	19.7	67.0	9.0	0.3	0.24	1
188 512	−0.17	0.05	0.03	10.8	−48.3	−10.1	38.6	8.5	0.1	0.18	1
193 901	−1.08	0.18	0.44	156.1	−245.0	−73.2	284.8	11.1	7.1	0.96	4
194 598	−1.12	0.29	0.58	76.4	−277.0	−30.7	276.3	8.9	0.5	0.82	4
195 019	0.04	0.01	0.00	71.8	−75.6	−37.4	95.5	9.1	0.5	0.35	1
198 149	−0.14	0.07	0.01	34.7	−97.6	10.5	92.5	8.6	0.2	0.41	1
201 891	−1.05	0.41	0.42	−91.4	−115.0	−58.8	155.6	9.9	1.0	0.55	3
204 155	−0.63	0.41	0.32	35.7	−127.0	−43.3	125.6	8.5	0.6	0.54	2
207 978	−0.52	0.21	–	−13.6	15.8	−7.4	35.0	11.0	0.0	0.14	1
209 458	−0.06	0.03	0.10	6.4	−18.5	2.2	12.3	8.5	0.1	0.04	1
221 830	−0.36	0.38	0.43	64.9	−113.0	62.7	135.4	9.0	1.5	0.48	2
222 794	−0.69	0.40	0.38	71.9	−103.0	82.5	143.1	9.2	2.2	0.43	2
298 986	−1.34	0.16	0.54	−239.4	−144.0	153.3	325.1	22.4	13.4	0.82	4
−4°320	−2.23	0.34	–	104.0	−267.0	−94.3	287.7	10.0	5.2	0.88	4
18°342	−0.90	0.12	0.42	83.7	−263.0	−52.1	268.4	9.0	1.8	0.88	4
2°3375	−2.15	0.51	–	364.0	−251.0	78.5	436.5	37.2	14.2	0.96	4
34°247	−1.96	0.29	–	−292.5	−266.0	−149.3	421.4	29.7	21.6	0.97	4
66°26	−2.20	0.24	–	173.7	−419.0	−73.0	446.5	15.1	2.0	0.52	4

Note. U, V, W, and V_{pec} are the spatial velocity components of the stars and their total peculiar velocities with respect to the local standard of rest $(-10, 10, 6)$: U is positive toward the Galactic anticenter, V is in the direction of the Galactic rotation, and W is directed toward the north Galactic pole; R is the apogalactic radius; Z_{max} is the maximum distance from the Galactic plane; and e is the eccentricity. The code denotes the types of Galactic population: 1—thin disk, 2—thick disk, 3—protodisk halo, and 4—accreted halo. The elemental abundances are given on a logarithmic scale, in solar units.

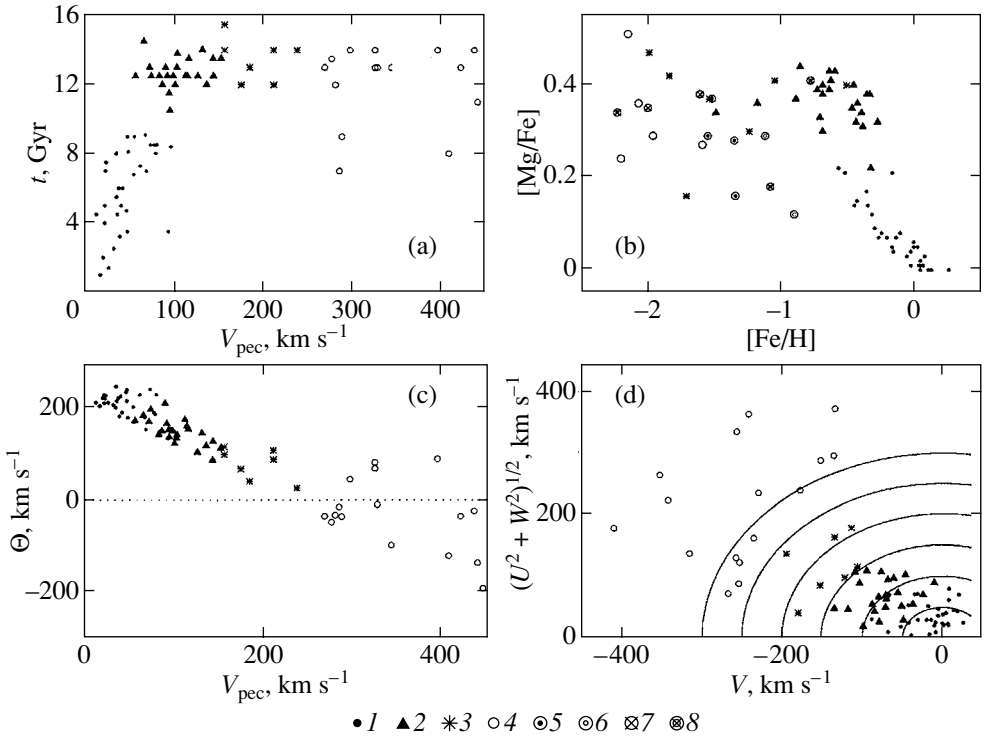

Fig. 1. Correlations between the peculiar stellar velocities relative to the local standard of rest and the stellar ages (a), between the metallicity and the relative Mg abundance (b), between the peculiar velocities and the stellar rotation velocities around the Galactic center (c), and between the peculiar stellar velocity components: *1*—thin-disk stars, *2*—thick-disk stars, *3*—protodisk-halo stars, and *4*—accreted halo stars. The following stars are additionally marked in the accreted halo in panel (b): *5*—stars with prograde orbits, *6*—stars of the cluster from (c) with coordinates of $V_{pec} \sim 280$ km s^{-1} and $\Theta \sim -30$ km s^{-1}, *7* and *8*—stars younger than 12.5 Gyr.

that the objects that constitute the accreted halo have apogalactic orbital radii larger than the Galactocentric distance of the Sun, high orbital eccentricities, high velocity dispersions, low rotation velocities (many of them are in retrograde orbits), often younger ages, and an underabundance of α-elements. The vertical and radial metallicity gradients are virtually equal to zero in the resulting subsystem. Studies of RR Lyrae variables show that a convenient criterion for field stars in the solar neighborhood is the total peculiar velocity of the star relative to the local standard of rest: when passing through some critical peculiar velocity (which is definitely higher than the circular velocity of Galactic rotation at the solar Galactocentric distance), the spatial–kinematic characteristics of the stars change abruptly. These changes suggest that all the low-metallicity population of field RR Lyrae variables is not homogeneous, but consists of at least two subsystems that differ in the volume occupied in the Galaxy (Borkova and Marsakov 2002, 2003). The most compelling argument for the extragalactic origin of a specific star is probably a close match between its orbital elements and chemical composition and the analogous parameters of the globular cluster for which it has been firmly established that it was accreted by our Galaxy in the past.

According to the hypothesis of the monotonic collapse of a protogalaxy from a halo to a disk suggested by Eggen *et al.* (1962), the stars that are genetically associated with the Galaxy cannot be in retrograde orbits. On the other hand, there must also be stars with prograde orbits among the stars accreted by the Galaxy. In any case, the velocity of the accreted stars with respect to the local centroid of the Sun must be very high. Therefore, the most natural criterion for separating accreted-halo stars seems to be the peculiar velocity. It follows from the $V_{pec}-\Theta$ diagram in Fig. 1c that stars with a negative tangential velocity, i.e., in retrograde orbits, appear when passing through $V_{pec} \geq 250$ km s^{-1}. The $V-\sqrt{U^2+W^2}$ diagram (see Fig. 1d) shows how the objects of the separated subsystems are distributed in the plane of the peculiar velocity components. Within the thin and thick disks, the total peculiar velocity increases mainly through a decrease in the rotation velocities of the stars around the Galactic center. At the same time, when going to the halo subsystems, the contributions from the other two velocity components

increase sharply. Note the very small number of stars in the protodisk halo compared to the number of stars that are assumed to have been captured from extragalactic space. As we pointed out above, observational selection is certain to have played a role here: mostly high-velocity stars were selected for the initial sample of low-metallicity stars. Recall, however, that globular clusters also exhibit a similar ratio of the numbers, although the accreted-halo objects were selected there by their internal property (the structure of the horizontal branch) rather than by their spatial position (Borkova and Marsakov 2000).

Let us consider the properties of the stars that we selected as accreted-halo candidates in more detail. We see from the $V_{\rm pec}-t$ diagram (Fig. 1a) that there are very young stars among them whose ages fall even within the range characteristic of the thin disk. As follows from Fig. 2 (crossed circles), the orbital elements are indicative of their obvious extragalactic origin. Four stars with prograde orbits could also raise doubts about their origin. In Fig. 2, they are highlighted by circles with a central dot. All of them have apogalactic orbital radii larger than 15 kpc; the maximum distance of three of the stars from the Galactic plane is larger than 3 kpc, and all four stars have highly eccentric ($e > 0.8$) orbits and old ages. These orbital elements fall within the range of parameters characteristic of the globular clusters that are assumed with a high probability to be accreted (Borkova and Marsakov 2000). Since no globular clusters with extremely blue branches (i.e., belonging to the protodisk halo) are observed at such large Galactocentric distances, we conclude that these four high-velocity stars with prograde orbits may have been lost by the accreted clusters and be extragalactic in origin.

The origin of yet another stellar group, the cluster of five stars in Fig. 1c with coordinates $V_{\rm pec} \sim 280$ km s^{-1} and $\Theta \sim -30$ km s^{-1} (HD 148816, 194598, 193901, BD$-4°3208$, $18°3423$), could also raise doubts. They are highlighted by small circles inside large circles in Fig. 2. It may well be that at the early evolutionary stages of a protogalaxy, some of the giant clouds could accidentally acquire a small negative rotation around the Galactic center through their natural velocity dispersion. In this case, these stars must be the oldest, their chemical composition must correspond to the composition of the first Galactic stars, and the maximum distances of the points of their orbits from the Galactic center and plane must be large. Their orbital eccentricities turned out to be actually very high ($e \approx 0.9$). However, their apogalactic radii are very small, the orbits for four of the five stars completely lie within the solar circle, and their ages lie within a wide range, so three of the five stars are younger than 12 Gyr (see Fig. 2). These properties are in conflict with the hypothesis that all these stars originated in a single protogalactic cloud. Note that the orbital elements of the stars from the group under discussion are in satisfactory agreement with those of the largest globular cluster ω Cen, which, as was pointed out above, is probably extragalactic in origin.

Note also the star HD 298986, whose orbital elements are equal, within the error limits, to the corresponding parameters of the accreted globular cluster Pal 5 (which probably belongs to dSph Srg). According to the Galactic model by Allen and Santillan (1991) used here, the parameters for the star and the cluster were found to be the following: apogalactic orbital radii of 22 and 19 kpc, perigalactic radii of 2 and 1.5 kpc, and $Z_{\rm max} = 13$ and 17 kpc, respectively. A comparison also indicates that the star and the cluster have not only similar [Fe/H] (-1.34 and -1.41 dex) and [α/Fe] (about 0.16 dex each), but also similar ages (about 13 Gyr each).

In the next section, we show that all of the stars attributed to the accreted halo by their kinematics exhibit sharp chemical anomalies.

THE CHEMICAL COMPOSITION OF ACCRETED-HALO STARS

The α- and r-elements are generally believed to be synthesized in stars with masses of $>10M_\odot$ and injected into the interstellar medium by SN II explosions. Therefore, the most probable [Eu/Mg] ratio for the Galactic stars must be equal to zero. However, the yield of α-elements increases with the mass of the SN II progenitor; the amount of magnesium increases by a factor of 10 to 20 as the mass of the SN progenitor changes from 13 to $25M_\odot$ (Thielemann *et al.* 1996). On the other hand, the yield of r-elements is related to the explosions of the lowest-mass type-II supernovae (see, e.g., Wheeler *et al.* 1998). Mashonkina *et al.* (2003) performed a comparative analysis of the relative abundances of magnesium (an α-element) and europium (an r-element). They found that the halo stars exhibit a significant spread in Eu abundances relative to Mg, while the thin- and thick-disk stars have [Eu/Mg] ≈ 0 with a smaller spread (the Galaxy was assumed to consist only of three subsystems.) These authors also considered all the possible causes of this abundance anomaly in the halo stars and concluded that the bulk of the Galactic europium and magnesium were produced in stars of different masses, and that the interstellar medium was weakly mixed in the early Galaxy. Figure 3 shows a [Fe/H]$-$[Eu/Mg] diagram for the same sample, but the stars were stratified into four Galactic subsystems. We see from the figure that all the accreted halo stars exhibit deviations from the most probable zero [Eu/Mg] ratio, while among the remaining

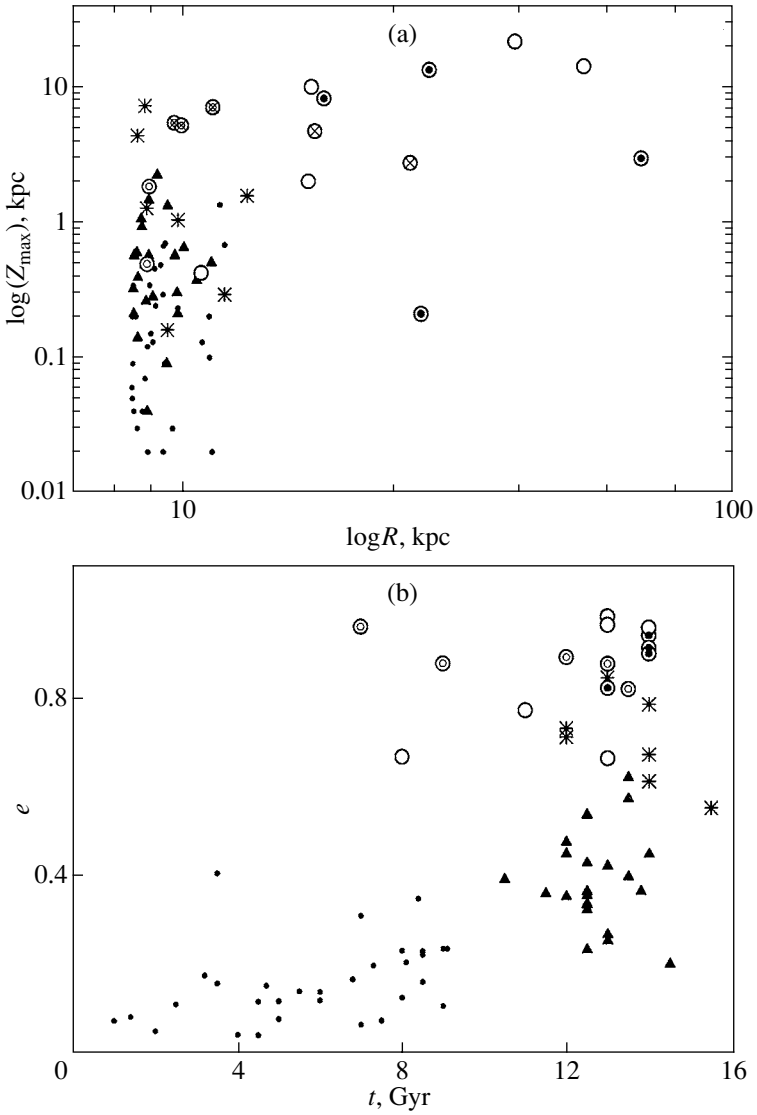

Fig. 2. Correlations between the maximum distances of the points of stellar orbits from the Galactic center and plane (a) and between the ages and the orbital eccentricities of stars (b). The notation is the same as that in Fig. 1.

stars, only two protodisk-halo stars (HD 25329 and HD 102200) exhibit such deviations.

We believe that the large spread in [Mg/Fe] is an argument for inefficient mixing of the interstellar medium in the halo. However, it follows from the [Fe/H]–[Mg/Fe] diagram (see Fig. 1b) that this spread is most likely associated with the accreted halo. Six of the seven protodisk-halo stars from our list have relative Mg abundances that lie within a narrow range, 0.32–0.47 dex (except the star HD 122196 with its anomalously low ratio, [Mg/Fe] = 0.16). Whereas the accreted-halo stars occupy the range from 0.12 to 0.51 dex, half of them (9 of the 16 stars) have Mg abundances <0.3 dex. In other words, the stars formed far from the Galactic center exhibit relative heavy-element abundances that often differ from those in the stars formed inside the protogalactic cloud. Clearly, the history of star formation cannot be the same as that of our Galaxy in all of the tidally disrupted dwarf galaxies. Because of the large number of disrupted galaxies and globular clusters as well as the large stellar dispersion within the tidal tails from them, the stars that were formed from protostellar clouds with different histories of enrichment with chemical elements will most likely be in the solar neighborhood.

As was pointed out above, the accuracy of determining the ages for low-mass main sequence stars is too low to obtain their statistically significant differences. Nevertheless, we formally divided all the accreted halo stars into two age groups. At the same time, the difference between the mean ages of

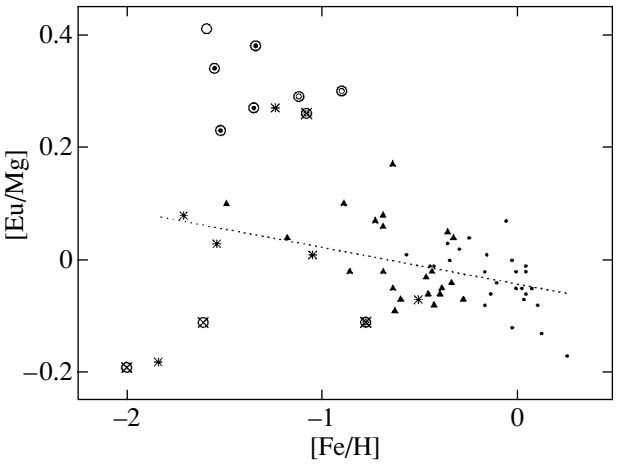

Fig. 3. Correlation between the iron abundances and [Eu/Mg] ratios for stars in the solar neighborhood. The notation is the same as that in Fig. 1. The dotted line represents an rms regression for the genetically associated stars ($r = 0.4 \pm 0.1$).

these stars exceeds the error limits ($\Delta t \approx 4 \pm 1$ Gyr). Therefore, let us consider the chemical composition of the stars in each age group. In Figs. 1b and 3, the open crossed circles highlight the accreted halo stars younger than $t < 12.5$ Gyr. For approximately the same Mg abundance as that for protodisk-halo and thick-disk stars, four of the highlighted young stars (except HD 193901) exhibit an Eu underabundance relative to Mg. (In the star BD−4°3208, which has a high ratio of [Mg/Fe] = 0.34, the Eu abundance has not been determined, probably because the line of this element is weak; therefore, we have attributed it to the group with a low [Eu/Mg] ratio.) Mashonkina *et al.* (2003) excluded two stars with an Eu underabundance (HD 34328 and HD 74000) by concluding that they "did not reflect the overall pattern of chemical evolution of the matter in our Galaxy." We believe that the very young low-metallicity stars with [Eu/Mg] < 0 were formed from matter that was mainly enriched by high-mass ($M > 30M_\odot$) SNe IIs. According to existing theories for the formation of chemical elements, the low metallicity of these stars at a high [Mg/Fe] ratio suggests that they are very old. Thus, the ages estimated from the evolutionary tracks are in conflict with their "chemical" ages. If the "isochronic" ages are actually accurate enough, then this contradiction can be resolved by assuming that the low metallicity for the anomalously young age of these stars is attributable to their formation from matter in which the primordial starburst occurred later than that in the single protogalactic cloud. Naturally, this assumption should be further tested on large statistical material.

The increasingly old accreted halo stars in Fig. 3 exhibit a significant overabundance, [Eu/Mg] > 0.2, with the Mg abundance relative to Fe being lower than that observed, on average, for the protodisk-halo and thick-disk stars: it follows from Fig. 1b that six of the seven protodisk-halo stars have [Mg/Fe] > 0.3, while this ratio for eight of the eleven old ($t >$ 12.5 Gyr) accreted halo stars is <0.3. The europium overabundance relative to magnesium in most of the old accreted halo stars suggests that the initial mass function of the stars formed outside the protogalaxy was cut off at high masses and began from $M \approx 10M_\odot$. As a result, the yield of α-elements was smaller than that within the single protogalactic cloud, where the masses of the SN progenitors were larger by several times. This interpretation also accounts for the low Mg abundance relative to iron in old accreted stars (see Fig. 1b). Indeed, the low [α/Fe] ratio for very old low-metallicity stars can be more naturally explained by the low masses of the SN II progenitors than by the injection of iron-group elements by SNe Ias, because an Eu underabundance would then also be simultaneously observed in these stars. However, as we see, europium is overabundant in these stars. Van den Bergh (2000) explained the low oxygen abundance in the stars of the very old low-metallicity globular cluster M 54, which was the center of the dwarf galaxy Srg, precisely by the deficit of high-mass SN II progenitors. It thus follows that the low abundance of α-elements alone in stars cannot unambiguously point to slow star formation in their parent protostellar cloud, as was suggested by Gilmore and Wyse (1998). This quantity is often taken as a "chemical" indicator of a young stellar age (see, e.g., Carney *et al.* 1997; King 1997; Hanson *et al.* 1998). Figure 1b also clearly shows that old stars with even lower relative Mg abundances appear near [Fe/H] ≈ −1.3 dex. Whereas nine of the eleven stars from the old group of accreted stars have [Mg/Fe] > 0.24 dex, the stars HD 298986 and BD 18°3423, falling in the range $-1.3 \le$ [Fe/H] ≤ -0.9 dex, exhibit [Mg/Fe] ≈ 0.15 dex (i.e., there is a difference exceeding the error limits). Although the isochronic ages of the two stars are within the error limits, they are still about one billion years younger than the oldest stars of extragalactic origin; i.e., a time long enough for SN I explosions to occur had elapsed by the time of their formation. HD 193901, which we included in the young group of accreted stars, lies in the same place in the diagram. This behavior can be understood by assuming that the intergalactic matter from which all the accreted stars in the old group were formed acquired their primordial injection of heavy elements at the same time as the protogalaxy, but from SNe II with masses much lower than those of the SNe that exploded inside the protogalaxy itself.

Subsequently, the star formation there was so slow that SNe Ia began to contribute appreciably to the iron abundance even at [Fe/H] ≈ -1.3.

Note the two properties that the genetically associated stars exhibit in Fig. 3. First, there is a spread in [Eu/Mg] in the protodisk halo: one of the stars that we attributed to this subsystem exhibits a large Eu abundance at a low Mg abundance (HD 102200), while another star exhibits a low Eu abundance at a high Mg abundance (HD 25329). Weak mixing of the interstellar medium appears to have actually taken place at the early evolutionary stages of our Galaxy, and stars were formed from clouds enriched by ejections from SNe II with different masses in its different places. Note also that all the remaining genetically associated stars show a tendency for [Eu/Mg] to decrease with increasing [Fe/H] at a relatively small spread (the correlation coefficient outside the 3σ limits is nonzero, $r = 0.4 \pm 0.1$). This behavior suggests that the maximum mass of the SN II progenitors formed inside the Galaxy increased with metallicity. The observed trend is also obtained if some amount of Mg is assumed to be additionally formed in AGB stars with $M < 8M_\odot$, but none of the existing theories for the synthesis of heavy elements makes this assumption. Here, however, it should be borne in mind that a systematic bias of the Mg and Eu abundance estimates as a function of metallicity can arise, because the abundances of these elements are determined from lines of different ionization stages, Mg I and Eu II.

DISCUSSION

Thus, the galactic orbital elements and the (α- and r-process) elemental abundances in the stars of the nearest regions of the solar neighborhood strongly suggest that some of them may be extragalactic in origin. The detected overabundance $\langle$[Eu/Mg]$\rangle = 0.30 \pm 0.03$ in all the old accreted stars of our sample (see Fig. 3) can be explained only by assuming that the initial mass function of the stars born outside the Galaxy is cutoff at high masses. The simple assumption about the weak mixing of the intergalactic matter with a single initial mass function for the entire Local System seems to be less tenable. Indeed, the natural isolation from one another of the explosion sites of SNe II with different masses must give rise to the next generations of stars, with an overabundance of both europium and magnesium. Moreover, since the yield of α-elements begins to overtake the yield of r-elements as the mass of the SN II progenitor increases, the probability of detecting Mg-overabundant stars should be much higher than that of detecting Eu-overabundant stars. However, interference from observational selection is possible here: the Eu lines used to estimate the Eu abundance in a star will be so weak that they will be lost in the spectral noise. Thus, the Eu abundance cannot be determined in a star where the amount of this element is small. As a result, a deficit of stars with [Eu/Mg] < 0 can arise in the sample. In our sample, we attributed 16 stars to the accreted halo. Eight and three of these stars exhibit [Eu/Mg] > 0.2 and less than zero, respectively. For five of the stars, the Eu abundance has not been determined. The metallicity of all five stars is approximately two orders of magnitude lower than the solar value. For two of them, [Mg/Fe] < 0.3 dex, while for the other three stars, the Mg abundance is comparable to that in the protodisk-halo and thick-disk stars. We may assume a relative Eu underabundance in the last three stars and an Eu overabundance in the first two stars. Thus, we have ten stars with an Eu underabundance and six stars with an Eu overabundance relative to Mg; i.e., only about a third of the stars could be formed from matter enriched by the explosions of high-mass SNe II. Four of the above six stars with [Eu/Mg] < 0 are younger than 12.5 Gyr (BD$-4°3208$, HD 74000, HD 34328, and HD 148816); above, we have assumed a later initial burst of star formation in the part of the extragalactic interstellar medium from which they were formed. Hence, high-mass SN progenitors began to explode in extragalactic space much later. The small number of accreted stars with an Eu underabundance in our sample most likely implies that high-mass SN progenitors outside the Galaxy do not determine the situation. However, for a Salpeter mass distribution of stars, SN progenitors with $M > 30M_\odot$ (which are believed to be the main suppliers of magnesium) must contaminate a much larger volume of the interstellar medium with α-elements than the volume that SNe IIs with masses of $8-10M_\odot$ (the main suppliers of europium) contaminate with r-elements. This is because the yield of α-elements in high-mass SN progenitors is a factor of about 20 larger than that in low-mass SN progenitors (Thielemann *et al.* 1977), while the yield of r-elements decreases (Wheeler *et al.* 1998). Thus, we believe that weak mixing of the extragalactic medium can explain only the general spread in [Eu/Mg] ratios in the accreted halo, while the dominance in it of stars with an Eu overabundance relative to Mg is probably attributable to the lower masses of the SN II progenitors outside the Galaxy relative to those in the Galaxy.

ACKNOWLEDGMENTS

We wish to thank L.I. Mashonkina for the opportunity to use the results of her doctoral dissertation, and for her helpful consultations and valuable remarks.

REFERENCES

1. C. Allen and A. Santillan, Rev. Mex. Astron. Astrofis. **22**, 255 (1991).
2. M. Barbier-Brossat and P. Figon, Astron. Astrophys., Suppl. Ser. **142**, 217 (2000).
3. D. L. Barris, C. A. Pilachowski, T. E. Armandroff, *et al.*, Astrophys. J. **544**, 302 (2000).
4. M. Bellazini and F. R. Ferraro, Astron. J. **125**, 188 (2003).
5. J. Bernkoff, A. Fiedler, and K. Fuhrmann, Astron. Soc. Pac. Conf. Ser. TNB **245**, 207 (2001).
6. T. V. Borkova and V. A. Marsakov, Astron. Zh. **77**, 750 (2000) [Astron. Rep. **44**, 665 (2000)].
7. T. V. Borkova and V. A. Marsakov, Astron. Zh. **79**, 510 (2002) [Astron. Rep. **46**, 460 (2002)].
8. T. V. Borkova and V. A. Marsakov, Astron. Astrophys. **398**, 133 (2003).
9. B. W. Carney, *Globular Clusters* (Univ. Chapel Hill, USA, 1999).
10. B. W. Carney, J. S. Wrigen, C. Sneden, *et al.*, Astron. J. **114**, 363 (1997).
11. D. Dinescu, S. R. Majewski, T. M. Girard, and K. M. Cudworth, Astron. J. **120**, 1892 (2000).
12. D. Dinescu, S. R. Majewski, T. M. Girard, and K. M. Cudworth, Astron. J. **122**, 1916 (2001).
13. B. Edvardsson, J. Andersen, B. Gustafsson, *et al.*, Astron. Astrophys. **275**, 101 (1993).
14. O. J. Eggen, D. Linden-Bell, and A. R. Sandage, Astrophys. J. **136**, 748 (1962).
15. K. Freeman, *IAU Symp. No. 153: Galactic Bulges,* Ed. by H. Dejonghe and H. J. Hobiug (Kluwer, Dordrecht, 1993), p. 263.
16. K. Furmann, Astron. Astrophys. **338**, 183 (1998).
17. K. Furmann, Astron. Nachr. (2003, in press).
18. G. Gilmore and R. F. G. Wyse, Astrophys. J. Lett. **367**, L55 (1991).
19. O. Yu. Gnedin and J. P. Ostriker, Astrophys. J. **474**, 223 (1997).
20. R. B. Hanson, C. Sneden, R. P. Kraft, and J. P. Fulbright, Astron. J. **116**, 1286 (1998).
21. R. Ibata, G. Gilmor, and M. Irvin, Nature **370**, 194 (1994).
22. L. R. King, Astron. J. **113**, 2302 (1997).
23. Larson, Astron. Soc. Pac. Conf. Ser. **92**, 241 (1996).
24. S. Leon, G. Meylan, and F. Combes, Astron. Astrophys. **359**, 907 (2000).
25. V. A. Marsakov and A. A. Suchkov, Astron. Zh. **54**, 1232 (1977) [Sov. Astron. **21**, 700 (1977)].
26. M. Mateo, Astron. Soc. Pac. Conf. Ser. **92**, 434 (1996).
27. L. Mashonkina, Astron. Astrophys. **364**, 249 (2000).
28. L. I. Mashonkina, Doctoral Dissertation in Mathematical Physics (St. Petersburg, 2003).
29. L. Mashonkina, T. Gehren, C. Travaglio, and T. Borkova, Astron. Astrophys. **397**, 275 (2003).
30. C. Palma and S. R. Majewski, Astrophys. J. **564**, 736 (2002).
31. F.-K. Thielemann, K. Nomatto, and G. Meyned, Astrophys. J. **460**, 408 (1977).
32. B. M. Tinsley, Astrophys. J. **229**, 1046 (1979).
33. T. Tshuchiya, D. Dinescu, and V. I. Korchagin, Astrophys. J. Lett. **589**, L29 (2003).
34. D. A. VandenBerg, Astrophys. J. **391**, 685 (1992).
35. D. A. VandenBerg, E. J. Swenson, F. J. Rogers, *et al.*, Astrophys. J. **532**, 430 (2000).
36. S. van den Bergh, Astrophys. J. **530**, 777 (2000).
37. J. C. Wheeler, J. J. Cowan, and W. Hillebrandt, Astrophys. J. Lett. **493**, L101 (1998).

Translated by V. Astakhov

Astronomy Letters, Vol. 30, No. 3, 2004, pp. 159–168. Translated from Pis'ma v Astronomicheskiĭ Zhurnal, Vol. 30, No. 3, 2004, pp. 185–195.

Determination of the Rotation Curve for Stars of the Gould Belt Using Bottlinger's Formulas

V. V. Bobylev*

Pulkovo Astronomical Observatory, Russian Academy of Sciences, Pulkovskoe shosse 65, St. Petersburg, 196140 Russia

Received May 14, 2003

Abstract—Based on the Hipparcos catalog and the radial velocities of stars published to date, we perform a kinematic analysis of OB stars. Parameters of the general Galactic rotation were determined from distant OB stars. We used the residual velocities of stars corrected for the general Galactic rotation to study the proper rotation of nearby OB stars. Geometrical characteristics of the Gould Belt were estimated by analyzing its kinematic parameters. We obtained parameters of peculiar solar motion as well as parameters of the proper rotation, expansion, and contraction for rotation around both the Galactic z axis and an axis perpendicular to the plane of symmetry of the disk. Kinematic parameters of the proper differential rotation were found for two age groups of nearby OB stars. Almost all of the nearby OB stars were shown to rotate in the same direction as the Galactic rotation. We constructed rotation curves. © *2004 MAIK "Nauka/Interperiodica"*.

Key words: *Gould Belt; Galaxy (Milky Way)*.

INTRODUCTION

Based on Hipparcos proper motions (ESA 1997) in combination with radial velocities, Palouš (1997), Comerón (1999), Torra *et al.* (2000), and Lindblad (2000) all performed a kinematic analysis of the Gould Belt stars. Palouš (1997) estimated the Oort constants A, B, C, and K for the youngest stars of the Gould Belt and concluded that the quadratic terms of the kinematic model are insignificant. Having analyzed the space velocities of the youngest Gould Belt stars, Comerón (1999) studied the gradient of the linear velocity W along the Galactic z axis. Based on a linear Oort–Lindblad model, Torra *et al.* (2000) estimated the Oort constants for a large number of stars as a function of their age. The individual ages of the stars were determined from Strömgren photometry. The mean age of the Gould Belt stars was shown to be 60×10^6 yr. Having analyzed the results by Comerón (1999) and Torra *et al.* (2000), Lindblad (2000) suggested a model for the proper differential rotation of the Gould Belt stars. This model takes into account the inclination of the axis of rotation to the Galactic plane, $i_G = 20°$, and the expansion of the stellar system; the magnitude of the angular velocity vector was found to be $|\omega_G| = 24$ km s^{-1} kpc^{-1}.

These authors disregarded the influence of general Galactic rotation on the motion of Gould Belt stars. One of our goals was to determine the proper-rotation parameters for the Gould Belt stars more accurately by using the space velocities of stars corrected for the general Galactic rotation.

Investigation of peculiar features in the motion of OB stars that are farther from the Sun than the presumed boundary of the Gould Belt, $r \sim 0.5$ kpc, is closely related both to the problems of general Galactic rotation and to the problems of studying the Gould Belt stars. Miyamoto and Zhu (1998) analyzed 1352 single O–B5 stars that were at heliocentric distances of up to 3 kpc and that did not belong to the Gould Belt. The analysis was based on a linear Ogorodnikov–Milne model using only the Hipparcos proper motions of the stars. The O–B5 stars were found to systematically rotate around the Galactic x axis with an angular velocity $2D_{32}^- = 3.8 \pm 1.1$ km s^{-1} kpc^{-1}.

Based on a nonlinear kinematic model and using the space velocities of stars, Dambis *et al.* (2001), Melnik *et al.* (2001), and Zabolotskikh *et al.* (2002) modeled the Galactic rotation and found a number of irregularities in the motion of OB associations at heliocentric distances of up to 3 kpc. Dambis *et al.* (2001) raised the question of the contraction of the distance scale for OB stars by 10–20%, which must be taken into account when determining the parameters of the general Galactic rotation.

Our goal here is to study the regular components in the motion (rotation, expansion, and con-

*E-mail: vbobylev@gao.spb.ru

traction) of nearby OB stars, most of which belong to the Gould Belt. We will analyze the kinematic features of nearby OB stars by using two data sets that were formed by separating the stars into luminosity classes, which is the same of a rough division into two age groups. This approach allows us to trace the evolutionary changes that happen to the cloud of hydrogen from which these OB stars were formed. Before studying these evolutionary changes on the basis of the complex Ogorodnukov–Milne kinematic model, particularly in the presence of both rotation and K effect, it is necessary to have an idea of the direction and center of rotation. This determines the choice of the simple rotation model based on Bottlinger's formulas used here.

THE WORKING DATA SETS

The following astrometric data were taken from the Hipparcos catalog (ESA 1997): the equatorial coordinates, parallaxes, and proper motions of the stars and their errors, spectral types, and luminosity classes. The radial velocities were taken from the catalog by Barbier-Brossat and Figon (2000). This catalog contains data on 4407 OB stars. Here, we use single stars (the astrometric orbital binaries marked by the symbol "O" in the catalog by Barbier-Brossat and Figon (2000) were discarded). We use only the stars for which both radial velocities and proper motions are available.

BASIC EQUATIONS

Here, we use a rectangular Galactic coordinate system with the axes directed away from the observer toward the Galactic center ($l = 0^\circ$, $b = 0^\circ$, the x axis), along the Galactic rotation ($l = 90^\circ$, $b = 0^\circ$, the y axis), and toward the Galactic north pole ($b = 90^\circ$, the z axis). The basic equations were derived from Bottlinger's standard formulas (Ogorodnikov 1965) in the form

$$\begin{aligned} V_r = &-u_\odot \cos b \cos(l - l_\mathrm{o}) \\ &- v_\odot \cos b \sin(l - l_\mathrm{o}) - w_\odot \sin b - R_\mathrm{o}(R - R_\mathrm{o}) \\ &\times \sin(l - l_\mathrm{o}) \cos b \omega'_\mathrm{o} - 0.5 R_\mathrm{o}(R - R_\mathrm{o})^2 \\ &\times \sin(l - l_\mathrm{o}) \cos b \omega''_\mathrm{o} + Kr \cos^2 b, \end{aligned} \quad (1)$$

$$\begin{aligned} kr\mu_l \cos b = &\, u_\odot \sin(l - l_\mathrm{o}) \\ &- v_\odot \cos(l - l_\mathrm{o}) - (R - R_\mathrm{o})(R_\mathrm{o} \cos(l - l_\mathrm{o}) \\ &- r \cos b)\omega'_\mathrm{o} - 0.5(R - R_\mathrm{o})^2 (R_\mathrm{o} \cos(l - l_\mathrm{o}) \\ &- r \cos b)\omega''_\mathrm{o} + r \cos b\, \omega_\mathrm{o}, \end{aligned} \quad (2)$$

$$\begin{aligned} kr\mu_b = &\, u_\odot \cos(l - l_\mathrm{o}) \sin b \\ &+ v_\odot \sin(l - l_\mathrm{o}) \sin b - w_\odot \cos b + R_\mathrm{o}(R - R_\mathrm{o}) \\ &\times \sin(l - l_\mathrm{o}) \sin b \omega'_\mathrm{o} + 0.5 R_\mathrm{o}(R - R_\mathrm{o})^2 \\ &\times \sin(l - l_\mathrm{o}) \sin b \omega''_\mathrm{o} - Kr \cos b \sin b. \end{aligned} \quad (3)$$

Here, $k = 4.740$, $r = 1/\pi$ is the heliocentric distance of the star, R_o is the distance from the Sun to the center of rotation, R is the distance from the star to the center of rotation, $u_\odot$, $v_\odot$, $w_\odot$ are the peculiar velocity components of the Sun with respect to the local standard of rest (LSR); the proper-motion components of the star $\mu_l \cos b$ and μ_b are in milliarcseconds per year (mas yr^{-1}), the radial velocity V_r is in km s^{-1}, the parallax π is in mas, and the distances R, R_o, and r are in kpc. The quantity ω_o is the angular velocity at distance R_o, ω'_o and ω''_o are the corresponding derivatives, K is the linear coefficient of radial expansion (or contraction), l_o is the direction of the center of rotation, and R can be calculated by using the expression

$$R^2 = (r \cos b)^2 - 2R_\mathrm{o} r \cos b \cos(l - l_\mathrm{o}) + R_\mathrm{o}^2. \quad (4)$$

Equations (1)–(3) contain seven sought-for unknowns: $u_\odot$, $v_\odot$, $w_\odot$, ω_o, ω'_o, ω''_o, and K, which can be determined by the least-squares method.

In contrast to Dambis *et al.* (2001), Melnik *et al.* (2001), and Zabolotskikh *et al.* (2002), who used two equations, (1) and (2), to determine the parameters of the Galactic rotation curve from distant OB stars, we also use Eq. (3). Since $|b|$ is close to 0° for distant OB stars, there is no particular need to use Eq. (3). For nearby OB stars, $|b| \sim 30^\circ$; therefore, Eq. (3) should be used.

Based on Eqs. (1)–(3), we will study the following two rotations:

(A) The general Galactic rotation; in this case, we assume that $l_\mathrm{o} = 0^\circ$.

(B) The proper rotation of nearby OB stars based on the residual (corrected for the general Galactic rotation) velocities of the stars. In this case, we make an attempt to also estimate the following geometrical characteristics by analyzing the kinematic parameters: l_o, R_o, and i_G—the inclination of the rotating disk to the Galactic plane. We will determine the kinematic parameters ω_o, ω'_o, ω''_o, and K for rotation around both the Galactic z axis and an axis perpendicular to the plane of symmetry of the disk (the following two quantities are required to characterize the direction of this axis: the inclination i_G and the direction of the ascending node Ω_G).

THE OORT CONSTANTS

We have gathered the independent determinations of the Oort constants published to date in the table. In their review article, Kerr and Lynden-Bell (1986) calculated the mean values of the Oort constants by using the large number of independent sources available at that time. Hanson (1987) determined the Oort

The Oort constants A and B

Source	A, km s^{-1} kpc^{-1}	B, km s^{-1} kpc^{-1}
Kerr and Lynden-Bell (1986)	$14.4_{(1.2)}$	$-12.0_{(2.8)}$
Hanson (1987)	$11.3_{(1.1)}$	$-13.9_{(0.9)}$
Lindblad (2000)	$13.7_{(1.0)}$	$-13.6_{(0.8)}$
Feast and Whitelock (1997)	$14.8_{(0.8)}$	$-12.4_{(0.6)}$
Feast *et al.* (1998)	$15.1_{(0.3)}$	
Bobylev (2002)	$12.9_{(1.3)}$	$-12.4_{(1.1)}$
Mean	$13.7_{(0.6)}$	$-12.9_{(0.4)}$

constants by analyzing the Lick Observatory absolute proper motions of 60 000 faint stars (of the 16th magnitude). Lindblad (1997) determined the Oort constants by using distant O and B stars from the Hipparcos catalog at $r \leq 2$ kpc that did not belong to the Gould Belt. Feast and Whitelock (1997) estimated the Oort constants from the Hipparcos proper motions of Cepheids. Feast *et al.* (1998) determined the Oort constant A using the available radial velocities of stars and a new zero point of the period–luminosity relation obtained from Hipparcos trigonometric parallaxes. Previously (Bobylev 2002), we estimated the Oort constants by analyzing the Pulkovo (PUL2 catalog) absolute proper motions of 31 452 faint stars (of the 15th magnitude). Based on the results listed in the table, we calculated the mean values of the Oort constants: $A = 13.7 \pm 0.6$ km s^{-1} kpc^{-1} and $B = -12.9 \pm 0.4$ km s^{-1} kpc^{-1}. These values are used here when taking into account the Galactic rotation on the basis of the Oort–Lindblad model (Ogorodnikov 1965).

RESULTS

Parameters of the Galactic Rotation

We formed a data set of distant OB stars (without their separation into luminosity classes) in the range of $0.3 < \pi < 1.5$ mas. Solving the system of Eqs. (1)–(3) yielded the following kinematic parameters: $(u_\odot, v_\odot, w_\odot) = (8.2 \pm 0.6, 11.6 \pm 0.7, 8.9 \pm 0.6)$ km s^{-1}

$$\begin{aligned} \omega_0 &= -28.0 \pm 0.6 \text{ km s}^{-1} \text{ kpc}^{-1}, \\ \omega_0' &= +4.17 \pm 0.14 \text{ km s}^{-1} \text{ kpc}^{-2}, \\ \omega_0'' &= -0.81 \pm 0.12 \text{ km s}^{-1} \text{ kpc}^{-3}, \\ K &= -3.0 \pm 0.4 \text{ km s}^{-1} \text{ kpc}^{-1}. \end{aligned} \quad (5)$$

The solution was obtained by analyzing 791 stars ($\overline{r} = 1.0$ kpc, the mean $\varepsilon_\pi/\pi = 1$). In Eqs. (1)–(4), we took $l_0 = 0°$ and the Galactocentric distance of the Sun $R_0 = 7.1$ kpc, which corresponds to the short distance scale (Dambis *et al.* 2001). The minus sign of ω_0 implies that the Galactic rotation is clockwise in the coordinate system under consideration. The peculiar velocity of the Sun and the apex coordinates are $V_\odot = 16.7 \pm 0.6$ km s^{-1}, $L_\odot = 55° \pm 2°$, and $B_\odot = 32° \pm 2°$. Next, Eqs. (1)–(3) were solved again, with the radial velocities and proper motions of the stars being corrected for the peculiar velocity of the Sun with respect to the LSR. For this purpose, we used the values from Dehnen and Binney (1998): $(u_\odot, v_\odot, w_\odot) = (10.0, 5.3, 7.2)$ km s^{-1}. As a result, we obtained the following components of the motion of distant OB stars with respect to the LSR: $(u_\odot, v_\odot, w_\odot) = (-1.8 \pm 0.6, 6.3 \pm 0.7, 1.8 \pm 0.6)$ km s^{-1}, $V_{\rm OB} = 6.8 \pm 0.6$ km s^{-1}. Since the peculiar velocity components of the Sun appear in Eqs. (1)–(3) with the opposite sign, the OB stars under consideration move in the direction specified by $L_{\rm OB} = 286° \pm 5°$ and $B_{\rm OB} = -15° \pm 5°$. The values of ω_0, ω_0', and ω_0'' obtained from distant OB stars may be considered as the parameters of the Galactic rotation. We also solved Eqs. (1)–(3) for the Galactocentric distance $R_0 = 8.5$ kpc recommended by the IAU (1986). The following kinematic parameters were obtained: $(u_\odot, v_\odot, w_\odot) = (8.3 \pm 0.6, 12.0 \pm 0.7, 8.9 \pm 0.6)$ km s^{-1},

$$\begin{aligned} \omega_0 &= -27.9 \pm 0.6 \text{ km s}^{-1} \text{ kpc}^{-1}, \\ \omega_0' &= +3.43 \pm 0.11 \text{ km s}^{-1} \text{ kpc}^{-2}, \\ \omega_0'' &= -0.55 \pm 0.10 \text{ km s}^{-1} \text{ kpc}^{-3}, \\ K &= -2.9 \pm 0.4 \text{ km s}^{-1} \text{ kpc}^{-1}. \end{aligned} \quad (6)$$

The Oort constants, which can be estimated by using the standard formulas (Ogorodnikov 1965) $A = 0.5 R_0 \omega_0'$ and $B = \omega_0 + 0.5 R_0 \omega_0'$, calculated from both solution (5), $A = 14.8 \pm 0.5$ km s^{-1} kpc^{-1} and $B = -13.2 \pm 0.8$ km s^{-1} kpc^{-1}, and solution (6),

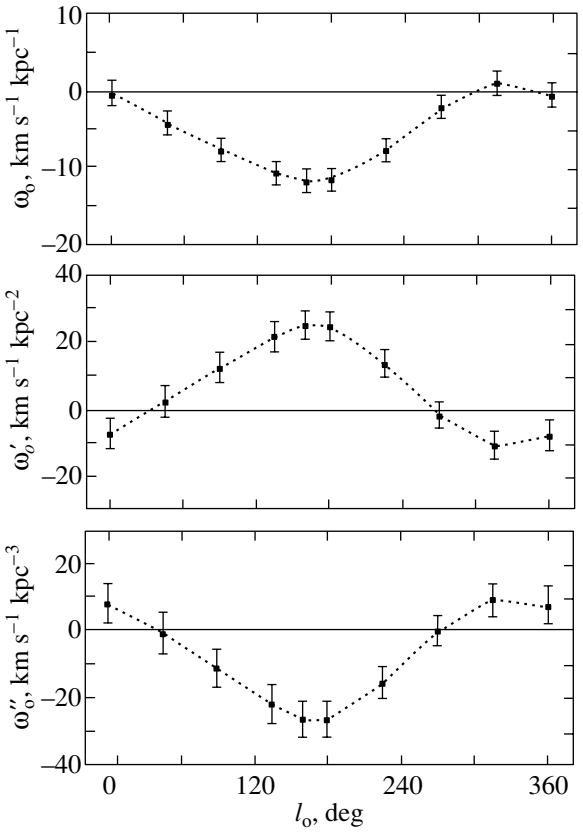

Fig. 1. Parameters of the rotation curve for nearby OB stars (group A) ω_o, ω'_o, and ω''_o versus l_o. R_o was taken to be 0.2 kpc.

$A = 14.6 \pm 0.5$ km s^{-1} kpc^{-1} and $B = -13.3 \pm 0.8$ km s^{-1} kpc^{-1}, are almost equal and are in good agreement with the values from them discussed above (table).

Proper Rotation of the Gould Belt Stars

Group A. Let us consider nearby OB stars that do not belong to the main sequence; stars of luminosity classes I, II, and III constitute most of these. We designate these stars as group A. The older Gould Belt stars (relative to the main-sequence OB stars) belong to this group. The stars were selected under the following conditions: 0.5 mas $< \pi$ ($r < 2$ kpc) and $\varepsilon_\pi/\pi < 1$; 1747 stars ($\overline{r} = 0.28$ kpc, the mean $\varepsilon_\pi/\pi = 0.37$) satisfy these conditions. We modeled the proper differential rotation of these stars by using Eqs. (1)–(3) in several steps:

(1) The radial velocities and proper motions of the stars were corrected for the Galactic rotation based on the rotation curve that we found at the previous step (solution (5)) by using Eqs. (1)–(3).

(2) The radial velocities and proper motions of the stars were corrected for the peculiar solar motion with respect to the LSR by using the values from Dehnen and Binney (1998): $(u_\odot, v_\odot, w_\odot) = (10.0, 5.3, 7.2)$ km s^{-1}.

(3) Based on the estimates of the distance to the center of rotation of the Gould Belt stars obtained by different authors (see Torra *et al.* 2000), we took $R_o = 0.2$ kpc as the initial value and used it to solve Eqs. (1)–(3) for various l_o.

The solutions are presented in Fig. 1. We see from the plots that ω_o, ω'_o, and ω''_o all have an extremum at $l_o = 160°$. In a wide range of latitudes, $l_o = 45°$–$225°$, at least one of the sought-for parameters differs significantly from zero.

The method of seeking for l_o needs to be explained. As can be seen from Eqs. (1)–(3), ω_o is determined only from Eq. (2) and does not depend on $l - l_o$, while we see an l_o-dependent wave in the upper panel of Fig. 1. If we introduce a phase angle $l - l_o = \theta$ and differentiate Eqs. (1)–(4) with respect to θ, then we obtain complex θ dependences of the quantities being determined. At the same time, as can be seen from Eq. (4), R depends on $\cos\theta$; therefore, it has an extremum at $\theta = 0°$ and $\theta = 180°$. When simultaneously solving Eqs. (1)–(3), this dependence $R = f(\theta)$ gives rise to the ω_o, ω'_o, and ω''_o waves (Fig. 1). The waves are asymmetric. The application of this method to distant stars in the case of modeling the Galactic rotation, where the change in l_o by 180° leads to a difference $\Delta R \sim 15$ kpc, shows that the asymmetry of the waves also manifests itself in the amplitudes of the parameters being determined. In analyzing the Gould Belt stars when $\Delta R \sim 0.5$ kpc, we can analyze only the phase shift, which is clearly seen in Fig. 1. The value of V_{OB} also depends on l_o. It has a maximum $V_{OB} = 8.50 \pm 0.35$ km s^{-1} at $l_o = 160°$ and a minimum $V_{OB} = 7.02 \pm 0.31$ km s^{-1} at $l_o = 45°$. Formally, two solutions are possible for the directions $l_o \approx 0°$ and 180°. We choose the solution for which l_o is in the second quadrant $90° < l < 180°$ (Olano 1982; Comerón and Torra 1991).

We solved Eqs. (1)–(3) with the adopted $l_o = 160°$ for various values of R_o in an effort to improve it. The solutions are presented in Fig. 2. All three of the parameters ω_o, ω'_o, and ω''_o differ significantly from zero over a wide R_o range: from 0.1 to 0.4 kpc. As can be seen from the plots, ω_o has a minimum at $R_o = 0.150$ kpc, while ω'_o and ω''_o share an extremum at $R_o = 0.220$–0.225 kpc. We took $R_o = 0.150$ kpc as the most probable distance to the center of rotation. A direct check (through construction of the rotation curves) indicates that changing R_o from 0.150 to 0.225 kpc causes the linear velocities to change by <0.25 km s^{-1}, which is not significant.

The OB stars under consideration move with respect to the LSR in the direction specified by $L_{OB} = 264° \pm 2°$ and $B_{OB} = +4° \pm 2°$ with a velocity $V_{OB} =$

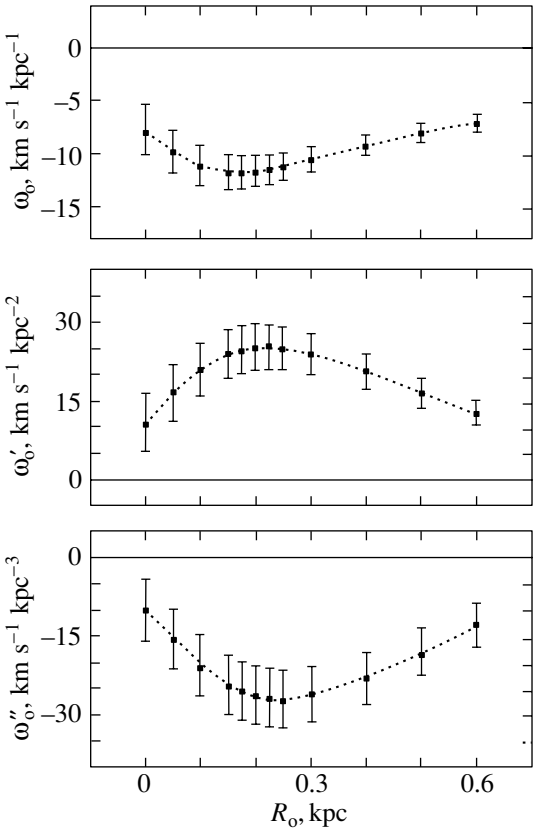

Fig. 2. Parameters of the rotation curve for nearby OB stars (group A) ω_o, ω'_o, and ω''_o versus R_o. The value of l_o was taken to be 160°.

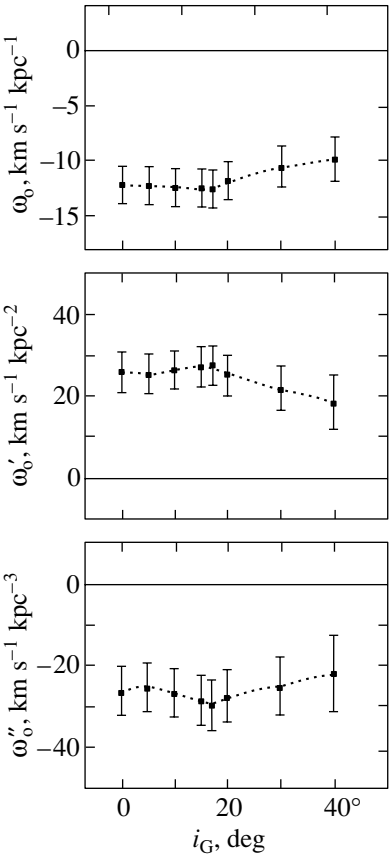

Fig. 3. Parameters of the rotation curve for nearby OB stars (group A) ω_o, ω'_o, and ω''_o versus inclination i_G for $R_o = 0.15$ kpc, $\Omega_G = 270°$, and $|z| < 0.2$ kpc; l_o was chosen to correspond to $l_o = 160°$ in the standard Galactic coordinate system.

7.1 ± 0.3 km s^{-1}. The kinematic parameters obtained for $l_o = 160°$, $i_G = 0°$, and $R_o = 0.15$ kpc are as follows: $(u_\odot, v_\odot, w_\odot) = (1.9 \pm 0.3, -8.2 \pm 0.3, -0.4 \pm 0.3)$ km s^{-1},

$$\begin{aligned} \omega_o &= -11.8 \pm 1.7 \text{ km s}^{-1} \text{ kpc}^{-1}, \\ \omega'_o &= +23.9 \pm 4.7 \text{ km s}^{-1} \text{ kpc}^{-2}, \\ \omega''_o &= -24.3 \pm 5.7 \text{ km s}^{-1} \text{ kpc}^{-3}, \\ K &= -6.0 \pm 0.6 \text{ km s}^{-1} \text{ kpc}^{-1}. \end{aligned} \qquad (7)$$

The Oort constants that characterize the proper differential rotation of the system of OB stars under consideration, as calculated using solution (7), are $A_G = +1.8 \pm 0.4$ km s^{-1} kpc^{-1} and $B_G = -10.0 \pm 1.7$ km s^{-1} kpc^{-1}.

We examined a method of correction for the Galactic rotation based on Eqs. (1)–(3) using the parameters that we obtained at $R_o = 8.5$ kpc (solution (6)). In this approach, for $l_o = 160°$ and $R_o = 0.15$ kpc, we found: $(u_\odot, v_\odot, w_\odot) = (1.8 \pm 0.3, -8.0 \pm 0.3, -0.4 \pm 0.3)$ km s^{-1}, $\omega_o = -11.4 \pm 1.7$ km s^{-1} kpc^{-1}, $\omega'_o = +23.6 \pm 4.7$ km s^{-1} kpc^{-2}, and $\omega''_o = -24.2 \pm 5.7$ km s^{-1} kpc^{-3}. This solution is virtually identical to solution (7). A direct check indicates that the rotation curves of the group-A stars have no significant differences.

We also considered a method of correction for the Galactic rotation based on a linear Oort–Lindblad model using the Oort constants $A = 13.7 \pm 0.6$ km s^{-1} kpc^{-1} and $B = -12.9 \pm 0.4$ km s^{-1} kpc^{-1}. In this approach, for $l_o = 160°$ and $R_o = 0.15$ kpc, we obtained: $(u_\odot, v_\odot, w_\odot) = (1.9 \pm 0.3, -8.3 \pm 0.4, -0.4 \pm 0.3)$ km s^{-1}, $\omega_o = -11.2 \pm 1.7$ km s^{-1} kpc^{-1}, $\omega'_o = +22.1 \pm 4.7$ km s^{-1} kpc^{-2}, and $\omega''_o = -24.4 \pm 5.7$ km s^{-1} kpc^{-3}. This solution differs from solution (7) in the derived value of ω''_o; this leads to a less distinct minimum of the rotation curve.

To improve the inclination of the rotating disk of Gould Belt stars to the Galactic plane, we solved Eqs. (1)–(3) for various values of i_G. We took the longitude of the ascending node from Torra *et al.* (2000) to be $\Omega_G = 270°$. In the above paper, the following geometrical characteristics were found from the sky distribution of Hipparcos stars: $i_G = 16°–20°$ and

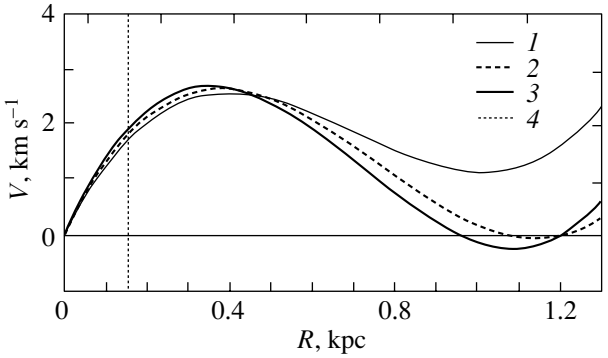

Fig. 4. Rotation curves for nearby OB stars (group A): *1*—the solution for $R_o = 0.15$ kpc, $l_o = 160°$, and $i_G = 0°$ (the correction for the Galactic rotation is based on the Oort–Lindblad model with the Oort constants $A = 13.7 \pm 0.6$ km s^{-1} kpc^{-1} and $B = -12.9 \pm 0.4$ km s^{-1} kpc^{-1}); *2*—for $R_o = 0.15$ kpc, $l_o = 160°$, and $i_G = 0°$ (solution (7)); *3*—for $R_o = 0.15$ kpc and $i_G = 17°$ (solution (8)) (the ascending node $\Omega_G = 270°$, while the direction of the center of rotation in the new Galactic coordinate system corresponds to $l_o = 160°$ in the standard coordinate system); *4*—the position of the Sun at $R_o = 0.15$ kpc.

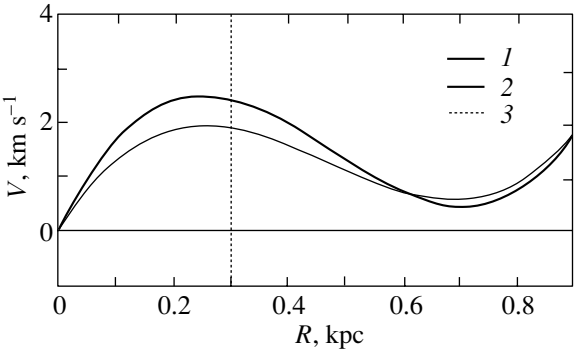

Fig. 5. Rotation curves for nearby OB stars (group B): *1* —for $R_o = 0.3$ kpc, $l_o = 160°$, and $i_G = 0°$; *2*—for $R_o = 0.3$ kpc and $i_G = 20°$, the direction of the center of rotation in the new Galactic coordinate system corresponds to $l_o = 160°$ in the standard coordinate system; *3*—the position of the Sun at $R_o = 0.3$ kpc.

$\Omega_G = 275°-295°$. We then passed to a new Galactic coordinate system associated with the plane of symmetry of the Gould Belt stars. Varying i_G over a wide range requires imposing a constraint on the distance of the star from the presumed plane of symmetry of the disk $z = r \sin b$; therefore, we used the condition $|z| < 0.2$ kpc. We chose l_o to correspond to $l_o = 160°$ in the standard Galactic coordinate system and $R_o = 0.15$ kpc. The solutions are presented in Fig. 3. All three of the parameters ω_o, ω_o', and ω_o'' differ significantly from zero in the i_G range from 0° to 20°. The extrema are indistinct; in fact, there are two extrema, at $i = 0°$ and $i = 17°$, because background stars have a significant effect. As a result, we took $i_G = 17°$ as the most probable value. The differential-rotation parameters for the Gould Belt stars obtained in the new coordinate system for the derived value of $i_G = 17°$ (and the adopted value of $\Omega_G = 270°$) are as follows:

$$\begin{aligned} \omega_o &= -12.5 \pm 1.7 \text{ km s}^{-1} \text{ kpc}^{-1}, \\ \omega_o' &= +27.4 \pm 5.0 \text{ km s}^{-1} \text{ kpc}^{-2}, \\ \omega_o'' &= -29.5 \pm 6.2 \text{ km s}^{-1} \text{ kpc}^{-3}, \\ K &= -6.3 \pm 0.6 \text{ km s}^{-1} \text{ kpc}^{-1}. \end{aligned} \qquad (8)$$

The Oort constants for the stellar system of the Gould Belt calculated using these parameters are $A_G = 2.1 \pm 0.4$ km s^{-1} kpc^{-1} and $B_G = -10.5 \pm 1.7$ km s^{-1} kpc^{-1}.

Figure 4 shows rotation curves for the group-A stars at inclinations of $i_G = 0°$ (solution (7)) and $i_G = 17°$ ($\Omega_G = 270°$) (solution (8)). As can be seen from the figure, the linear rotation velocity $V(R)$ is 2 km s^{-1} at $R = R_o$ and approaches 3 km s^{-1} at $R = 0.4$ kpc. We may conclude from the position of the minimum of the function $V(R)$ that the radius of the stellar system of the Gould Belt does not exceed 1 kpc. Using $\omega_o = -12.5$ km s^{-1} kpc^{-1} determined above (solution (8)), we obtain an estimate of the period in which the Gould Belt stars make one turn around the rotation axis: $T = 2\pi/\omega_o = 500 \times 10^6$ yr. Using the results from Torra *et al.* (2000) regarding the values of K as the calibration values ($K = -5.1 \pm 1.5$ km s^{-1} kpc^{-1} in the range $0.1 < r \leq 2.0$ kpc for ages $T > 60 \times 10^6$ yr), we may conclude that the group-A stars have a mean age of more than 60×10^6 yr.

Group B. We consider nearby main-sequence OB stars of luminosity classes IV and V. Let us designate these stars as group B. The relatively younger stars of the Gould Belt belong to this stellar group. The stars were selected under the following conditions: 1.0 mas $< \pi$ ($r < 1$ kpc) and $\varepsilon_\pi/\pi < 1$; 1443 stars ($\overline{r} = 0.21$ kpc, the mean $\varepsilon_\pi/\pi = 0.26$) satisfy these conditions.

We found that the OB stars under consideration move with respect to the LSR in the direction specified by $L_{OB} = 262° \pm 2°$ and $B_{OB} = 1° \pm 2°$ with a velocity $V_{OB} = 9.0 \pm 0.3$ km s^{-1}. Based on the method described above, we unambiguously determine the distance $R_o = 0.3$ kpc; the direction $l_o = 160°$ is determined less reliably (the range from 160° to 140°). The kinematic parameters obtained for $l_o = 160°$, $i_G = 0°$, and $R_o = 0.3$ kpc are as follow: $(u_\odot, v_\odot, w_\odot) = (2.0 \pm 0.3, -10.0 \pm 0.4, -0.1 \pm 0.3)$ km s^{-1},

$$\omega_o = -6.3 \pm 1.5 \text{ km s}^{-1} \text{ kpc}^{-1},$$

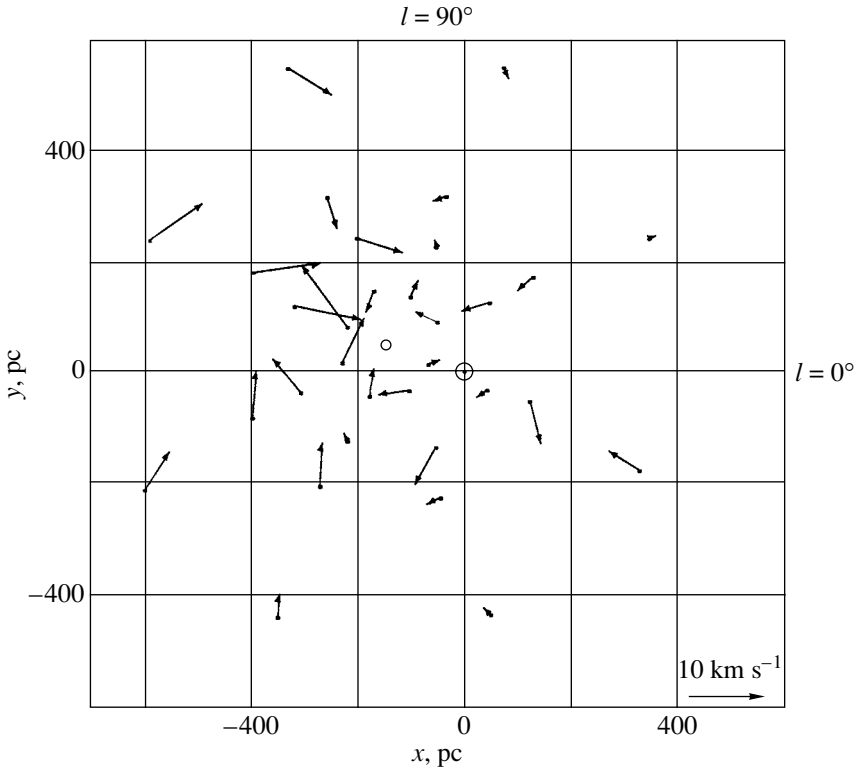

Fig. 6. Mean residual velocities U and V of nearby OB stars (group A) in projection onto the Galactic xy plane. The Sun is at the coordinate origin. The circle marks the center of rotation found: $l_o = 160°$ and $R_o = 0.15$ kpc.

$$\begin{aligned} \omega_0' &= +26.7 \pm 7.3 \text{ km s}^{-1} \text{ kpc}^{-2}, \\ \omega_0'' &= -65 \pm 18 \text{ km s}^{-1} \text{ kpc}^{-3}, \\ K &= -2.5 \pm 0.7 \text{ km s}^{-1} \text{ kpc}^{-1}. \end{aligned} \quad (9)$$

The Oort constants calculated by using these parameters are $A_G = +4.0 \pm 1.1$ km s^{-1} kpc^{-1} and $B_G = -2.3 \pm 1.9$ km s^{-1} kpc^{-1}. In contrast to the group-A stars, there is a distinct peak of the rotation parameters for the group-B stars when seeking i_G. The latter has been reliably determined: $i_G = 20°$. The kinematic parameters obtained for $l_o = 160°$, $i_G = 20°$ and $R_o = 0.3$ kpc are as follows: $(u_\odot, v_\odot, w_\odot) = (2.0 \pm 0.3, -10.0 \pm 0.4, -0.1 \pm 0.3)$ km s^{-1},

$$\begin{aligned} \omega_0 &= -8.1 \pm 1.5 \text{ km s}^{-1} \text{ kpc}^{-1}, \\ \omega_0' &= +35.2 \pm 7.6 \text{ km s}^{-1} \text{ kpc}^{-2}, \\ \omega_0'' &= -84 \pm 20 \text{ km s}^{-1} \text{ kpc}^{-3}, \\ K &= -2.0 \pm 0.8 \text{ km s}^{-1} \text{ kpc}^{-1}. \end{aligned} \quad (10)$$

Figure 5 shows the two rotation curves constructed from solutions (9) and (10).

The residual velocities U and V. Figure 6 shows the mean residual velocities of OB stars, U and V, in projection onto the Galactic xy plane for the group A stars. The velocities U and V were calculated using standard formulas (Kulikovskii 1985) in the standard Galactic coordinate system at $l_o = 0°$. The velocities of the stars were corrected for the general Galactic rotation, for the peculiar solar motion (relative to the apex; Dehnen and Binney 1998), and for the derived general linear motion of the OB stars. The coordinates of the stars within $r = 850$ pc were referred to the found center of rotation, broken down into 45° sectors, and divided into four distance zones in each sector. In each of the 32 parts, we calculated the mean residual velocities, which are shown in the figure. There are four velocity vectors on each of the eight rays emanating from the center of rotation, each of which can be decomposed into tangential and radial components. As can be seen from the figure, on each of the eight rays, the tangential component satisfactorily reproduces our rotation curve (the rotation from the y axis to the x axis) (Fig. 4). The two rays of quadrant I, $0° < l < 90°$, constitute an exception. We also clearly see the radial component toward the center (the negative K-effect), the magnitude of which reaches $\approx$4 km s^{-1} for stars far from the center (particularly in quadrants II and III). Figure 7 shows the mean residual velocities of OB stars, U and V, in projection onto the xy plane for the group-B stars. As can be seen from the figure, the residual velocities of these stars are of a more distinct, local nature. More specifically, the velocities are high within $\approx$0.3 kpc

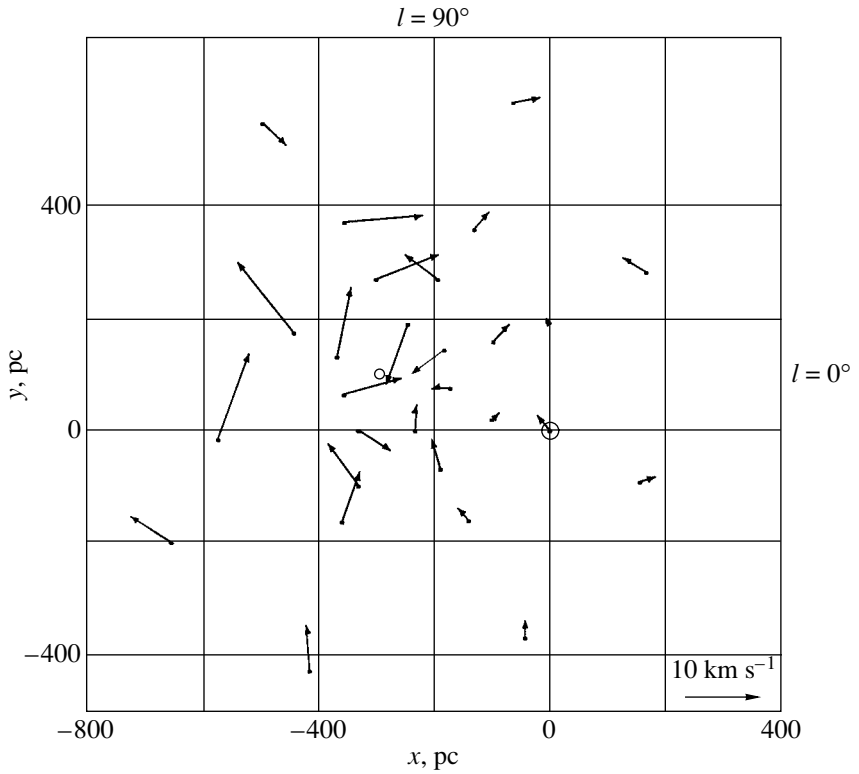

Fig. 7. Mean residual velocities U and V of nearby OB stars (group B) in projection onto the Galactic xy plane. The Sun is at the coordinate origin. The circle marks the center of rotation found: $l_o = 160^\circ$ and $R_o = 0.3$ kpc.

of the stellar center of the Gould Belt; at larger distances, their distribution is random in nature.

DISCUSSION

Our kinematic parameters of distant OB stars (solution (5)) agree well with the kinematic parameters of 59 distant ($\overline{r} = 1.9$ kpc) OB associations found by Dambis *et al.* (2001): $(u_\odot, v_\odot, w_\odot) = (8.2 \pm 1.3, 11.9 \pm 1.1, 9.5 \pm 0.9)$ km s^{-1}, $\omega_o = -29.1 \pm 1.0$ km s^{-1} kpc^{-1}, $\omega_o' = +4.57 \pm 0.20$ km s^{-1} kpc^{-2}, and $\omega_o'' = -1.32 \pm 0.14$ km s^{-1} kpc^{-3} at $R_o = 7.1$ kpc and with the results by Melnik *et al.* (2001): $(u_\odot, v_\odot) = (7.5 \pm 0.9, 11.2 \pm 1.3)$ km s^{-1}, $\omega_o = -30.2 \pm 0.8$ km s^{-1} kpc^{-1}, $\omega_o' = +5.0 \pm 0.2$ km s^{-1} kpc^{-2}, and $\omega_o'' = -1.5 \pm 0.2$ km s^{-1} kpc^{-3} at $R_o = 7.1$ kpc and $w_\odot = 7$ km s^{-1}, where they were determined from 132 distant OB associations. Our kinematic parameters of distant OB stars at $R_o = 8.5$ kpc (solution (6)) are in agreement with the parameters of the Galactic rotation curve found by Zabolotskikh *et al.* (2002): $(u_\odot, v_\odot, w_\odot) = (7.21 \pm 2.10, 12.33 \pm 1.76, 8.24 \pm 1.61)$ km s^{-1}, $\omega_o = -26.61 \pm 1.35$ km s^{-1} kpc^{-1}, $\omega_o' = +3.66 \pm 1.35$ km s^{-1} kpc^{-2}, and $\omega_o'' = -0.73 \pm 0.19$ km s^{-1} kpc^{-3} at $R_o = 8.5$ kpc, where they were determined from distant classical Cepheids and open star clusters (the signs of ω_o were changed here to reconcile them with our coordinate system). This agreement leads us to conclude that our correction for the general Galactic rotation is reliable.

The direction of the center of rotation of the Gould Belt stars and the distance that we found for it here, $l_o = 160^\circ$ and $R_o = 0.15$ kpc (group A), are in agreement with the direction of the center of rotation of the neutral hydrogen cloud, $l_o = 131^\circ$ and $R_o = 0.166$ kpc, obtained by Olano (1982) as well as with the estimates made by Comerón and Torra (1991) for the Gould Belt stars: $l_o = 146^\circ$ and $R_o = 0.080$ kpc. The inclination of the rotation axis of nearby OB stars that we obtained here, $i_G = 17^\circ - 20^\circ$, agrees well with the inclination of the system of Gould Belt stars, $i_G = 16^\circ - 20^\circ$, found by Torra *et al.* (2000).

The value of $2D_{32}^-$ found by Miyamoto and Zhu (1998) may be considered as a component of the angular velocity of the Gould Belt stars along the Galactic x axis. It is important to emphasize that the component of the vector of rigid-body rotation around the x axis is free from the influence of the general Galactic rotation. Taking $i_G = 20^\circ$ and $\Omega_G = 270^\circ$, we obtain $|\omega_o| = 2D_{32}^-/\cos 70^\circ = 11.1 \pm 3.2$ km s^{-1} kpc^{-1}. In this case, the plus sign of D_{32}^- corresponds to the

rotation of the Gould Belt stars with the minus sign in our coordinate system. In this approach, there is agreement between our value of the angular velocity ω_o (solutions (7) and (9)) and the results by Miyamoto and Zhu (1998).

Our maximum value of ω_o (solution (8)) is a factor of two smaller than the estimate by Lindblad (2000): $\omega_G = B - A_\omega = -24$ km s^{-1} kpc^{-1}; Lindblad used $A_\omega = 6.4$ km s^{-1} kpc^{-1} and $B = -17.4$ km s^{-1} kpc^{-1}. This difference arises, first, from A_G. In our case, as analysis of solutions (7) and (8) shows, it is small, $A_G = 2.1$ km s^{-1} kpc^{-1}, and makes no appreciable contribution to the angular velocity ω_G. Second, the value of $B = -17.4$ km s^{-1} kpc^{-1} found by Torra *et al.* (1997) and used by Lindblad was not corrected for the general Galactic rotation. We may conclude that Lindblad's value of $\omega_G = -24$ km s^{-1} kpc^{-1} was overestimated by a factor of 2.

A comparison of the rotation curves indicates that the contribution of the second derivative ω''_o (Fig. 4) to the decomposition of the angular velocity of Galactic rotation leads to a linear velocity difference of ~ 1 km s^{-1} at $R \sim 1$ kpc. The correction for the Galactic rotation made by using Eqs. (1)–(3) (solutions (7) and (8)) is more accurate if the second derivative characterizes precisely the Galactic rotation. This question is related to the establishment of a distance scale if the latter is established by analyzing OB stars (Dambis *et al.* 2001). Indeed, in the presence of the proper rotation of OB stars with the minus sign, the angular velocity of Galactic rotation estimated from these stars will be overestimated, which will lead to a contraction of the distance scale.

A comparison of the rotation curves, solutions (7), (8) and (9), (10) (see also Figs. 4 and 5), indicates that allowing for the inclination i_G does not lead to any significant linear velocity difference. Therefore, for applications, for example, to correct the observed motions for the proper rotation of nearby OB stars, it is convenient to use solution (7), (9) and Eqs. (1)–(3).

CONCLUSIONS

The parameters of the general Galactic rotation determined from distant ($0.67 < r < 3.0$ kpc) OB stars, $\omega_o = -28.0 \pm 0.6$ km s^{-1} kpc^{-1}, $\omega'_o = +4.17 \pm 0.14$ km s^{-1} kpc^{-2}, $\omega''_o = -0.81 \pm 0.12$ km s^{-1} kpc^{-3}, and $K = -3.0 \pm 0.4$ km s^{-1} kpc^{-1}, ($R_o = 7.1$ kpc), allow the residual velocities of nearby OB stars to be estimated reliably.

Our analysis of the motions of nearby OB stars performed with their separation into two groups by luminosity classes leads us to several important conclusions about the kinematic evolution of the hydrogen cloud from which all the stars of the Gould Belt were formed. By kinematic evolution we mean the rotation, expansion, and contraction, and the possible precession of the rotation axis. First, we have shown that linear translational motion with respect to the LSR with $V_{OB} = 7$–9 km s^{-1} in the direction $l \approx 270°$ is common to all the nearby OB stars, implying that these stars were formed from a single hydrogen cloud that filled the interarm circumsolar space within up to $r = 1$–1.5 kpc. Second, proper rotation around the z axis with an angular velocity of from $\approx$–10 km s^{-1} kpc^{-1} is common to all the nearby OB stars. Third, for the overwhelming majority of nearby OB stars, there is a negative K effect, implying that the gas from which the stars were formed is in a state of contraction. We may conclude that the youngest and least numerous stars of the Gould Belt with a known positive K effect (expansion) were probably formed 20–30×10^6 yr ago (Torra *et al.* 2000) after the explosion of the hydrogen cloud (Olano 1982), and their motion reflects the instantaneous state of the long existing rotating hydrogen cloud.

The nearby OB stars, which mostly belong to the Gould Belt, have been shown for the first time to have a significant second derivative in the decomposition of the angular velocity of their proper rotation.

The kinematic parameters of the proper differential rotation of nearby ($\overline{r} = 0.29$ kpc) OB stars with luminosity classes I, II, and III were found to be the following: $\omega_o = -12.5 \pm 1.7$ km s^{-1} kpc^{-1}, $\omega'_o = +27.4 \pm 5.0$ km s^{-1} kpc^{-2}, $\omega''_o = -29.5 \pm 6.2$ km s^{-1} kpc^{-3}, and $K = -6.3 \pm 0.6$ km s^{-1} kpc^{-1}, for the distance to the center of rotation $R_o = 0.15$ kpc found in our modeling in the direction $l_o = 160°$ and for the inclination of the rotating disk to the Galactic plane $i_G = 17°$ ($\Omega_G = 270°$).

In contrast to the standard localization of the Gould Belt ($r < 500$ pc) based on an analysis of the spatial distribution of the youngest OB stars (Torra *et al.* 2000), our kinematic parameters of the proper rotation of stars with luminosity classes I, II, and III show that rotation takes place up to distances $r \sim 1$ kpc. This rotation should be taken into account in a kinematic analysis of distant ($r > 0.5$ kpc) OB stars.

The kinematic parameters of the proper differential rotation of nearby ($\overline{r} = 0.21$ kpc) main-sequence OB stars are $\omega_o = -8.1 \pm 1.5$ km s^{-1} kpc^{-1}, $\omega'_o = +35.2 \pm 7.6$ km s^{-1} kpc^{-2}, $\omega''_o = -84.2 \pm 19.9$ km s^{-1} kpc^{-3}, and $K = -2.0 \pm 0.8$ km s^{-1} kpc^{-1}, for the distance to the center of rotation $R_o = 0.3$ kpc found in our modeling in the direction $l_o = 160°$ and for the inclination of the

rotating disk to the Galactic plane $i_G = 20°$ ($\Omega_G = 270°$). The minus sign of ω_0 implies that the Gould Belt stars rotate in the same direction as the Galactic rotation.

In general, we conclude that the systematic linear velocity components of nearby OB stars depend on two effects: rotation and contraction. The proper rotation of the Gould Belt dominates at a distance of $r = 0.3$ kpc from the center ($R_0 = 0.2$–0.3 kpc in the direction $l = 160°$). In this case, the mean linear velocity reaches 3 ± 1 km s^{-1} and rapidly decreases to zero with increasing r. The contraction effect dominates outside the boundary of $r = 0.3$ kpc (from the Sun). As r increases, this effect leads to an increasing component in the stellar velocities, and the mean linear velocity reaches -3 ± 0.3 km s^{-1} even at the $r = 0.5$ kpc boundary, for example, for relatively old OB stars.

ACKNOWLEDGMENTS

I wish to thank the referees for their valuable remarks. I am grateful to V.V. Vityazev, E.V. Khrutskaya, and A.T. Baikova for their help and useful discussions of the results. This work was supported by the Russian Foundation for Basic Research (project no. 02-02-16570).

REFERENCES

1. M. Barbier-Brossat and P. Figon, Astron. Astrophys., Suppl. Ser. **142**, 217 (2000).
2. V. V. Bobylev, Izv. GAO Pulkovo **216**, 57 (2002).
3. F. Comerón, Astron. Astrophys. **351**, 506 (1999).
4. F. Comerón and J. Torra, Astron. Astrophys. **241**, 57 (1991).
5. A. K. Dambis, A. M. Melnik, and A. S. Rastorguev, Pis'ma Astron. Zh. **27**, 68 (2001) [Astron. Lett. **27**, 58 (2001)].
6. W. Dehnen and J. J. Binney, Mon. Not. R. Astron. Soc. **298**, 387 (1998).
7. M. W. Feast, F. Pont, and P. A. Whitelock, Mon. Not. R. Astron. Soc. **298**, L43 (1998).
8. M. W. Feast and P. A. Whitelock, Mon. Not. R. Astron. Soc. **291**, 683 (1997).
9. R. B. Hanson, Astron. J. **94**, 409 (1987).
10. F. J. Kerr and D. Lynden-Bell, Mon. Not. R. Astron. Soc. **221**, 1023 (1986).
11. P. G. Kulikovskii, *Stellar Astronomy* (Nauka, Moscow, 1985) [in Russian].
12. P. O. Lindblad, Astron. Astrophys. **363**, 154 (2000).
13. P. O. Lindblad, J. Palouš, K. Lodén, *et al.*, in *HIPPARCOS Venice'97,* Ed. by B. Battrick (ESA Publ. Div., Noordwijk, 1997), p. 507.
14. A. M. Melnik, A. K. Dambis, and A. S. Rastorguev, Pis'ma Astron. Zh. **27**, 611 (2001) [Astron. Lett. **27**, 521 (2001)].
15. M. Miyamoto and Z. Zhu, Astron. J. **115**, 1483 (1998).
16. K. F. Ogorodnikov, *Dynamics of Stellar Systems* (Fizmatgiz, Moscow, 1965) [in Russian].
17. C. A. Olano, Astron. Astrophys. **112**, 195 (1982).
18. J. Palouš, in *Reference System and Frames in the Space Era: Present and Future Astrometric Programmes,* Ed. by J. Vondrák and N. Capitane (Prague, 1997), p. 157.
19. *The Hipparcos and Tycho Catalogues* (ESA SP-1200, 1997).
20. J. Torra, D. Fernández, and F. Figueras, Astron. Astrophys. **359**, 82 (2000).
21. J. Torra, A. E. Gómez, F. Figueras, *et al.*, in *HIPPARCOS Venice'97,* Ed. by B. Battrick (ESA Publ. Div., Noordwijk, 1997), p. 513.
22. M. V. Zabolotskikh, A. S. Rastorguev, and A. K. Dambis, Pis'ma Astron. Zh. **28**, 516 (2002) [Astron. Lett. **28**, 454 (2002)].

Translated by V. Astakhov

Astronomy Letters, Vol. 30, No. 3, 2004, pp. 169–178. Translated from Pis'ma v Astronomicheskiĭ Zhurnal, Vol. 30, No. 3, 2004, pp. 196–206.

Magnetic Field Rearrangement by Accelerated Particles Near a Shock Front

A. Z. Dolginov, N. I. Podol'skaya, and I. N. Toptygin*

St. Petersburg State Technical University, ul. Politekhnicheskaya 29, St. Petersburg, 195251 Russia

Received June 30, 2003

Abstract—We solve the self-consistent problem of the generation of a static magnetic field by the electric current of accelerated particles near a strong plane MHD shock front. We take into account the back reaction of the field on the particle diffusion tensors and the background plasma parameters near the front. Various states that differ significantly in static magnetic-field strength are shown to be possible near a strong front. If the initial field has a component normal to the front, then its components parallel to the front are suppressed by accelerated particles by several orders of magnitude. Only the component perpendicular to the front remains. This field configuration for uniform particle injection at the front does not lead to the generation of an additional field, and, in this sense, it is stable. If the initial field is parallel to the front, then either its significant enhancement by two or three orders of magnitude or its suppression by several orders of magnitude is possible. The phenomenon under consideration is an example of the self-organization of plasma with a magnetic field in a strongly nonequilibrium system. It can significantly affect the efficiency of particle acceleration by the shock front and the magnetobremsstrahlung of the accelerated particles.

Key words: *plasma astrophysics, hydrodynamics and shocks, particle acceleration, magnetic field, self-organization.*

INTRODUCTION

The high efficiency of mechanical energy transfer to accelerated particles was pointed out even in the pioneering papers devoted to the acceleration of charged particles by strong MHD shock fronts in a turbulent medium (Axford *et al.* 1978; Bell 1978; Krymskii 1981; Völk and McKenzie 1982). They can acquire an energy that accounts for several tens of percent of the energy of a hydrodynamic flow. As a result, accelerated particles have a noticeable back reaction on the plasma flow velocity and the turbulence near the shock front. Various aspects of these phenomena have been investigated by many authors (Jones and Ellison 1991; Berezhko *et al.* 1996; Toptygin 1997). In the above and other papers, it was shown that accelerated particles deform the hydrodynamic flow velocity profile and may cause the thermal discontinuity to be completely smeared; they also intensively generate hydromagnetic (mainly Alfvén) disturbances with wavelengths on the order of the Larmor radius of the accelerated particles by a resonant mechanism. Recently, the last topic (the generation of Alfvén turbulence by accelerated particles) has again been expanded upon by Lucek and Bell (2000) and Bell and Lucek (2001).

In this paper, we consider yet another aspect of this problem—the possible generation of a static magnetic field with a scale length on the order of the thickness of the preshock region, $L \approx \kappa_1/u_1$, by the electric current of accelerated relativistic particles. Here, κ_1 is the component of the relativistic particle diffusion tensor normal to the front, and u_1 is the normal component of the hydrodynamic plasma velocity. For nonrelativistic shocks, this scale length is much larger than the Larmor radius of relativistic particles. Previously, we noted (Dolginov and Toptygin 2003) that relativistic particles (cosmic rays) can contribute to the generation of the large-scale Galactic field. Here, we show that relativistic particles in the individual sources in which they are generated can also affect noticeably the magnetic field. These sources include the strong shock fronts of supernova remnants and presupernova stellar winds. In most of the cases that we studied, the initial field components parallel to the front are strongly weakened.

Let a plane shock front ($z = 0$) be the source of accelerated protons the mean energy of which will be specified below. Since atomic nuclei heavier than protons and electrons constitute a small fraction of the accelerated particles, we disregard them. The background plasma and the background neutral medium are also assumed to be purely hydrogen ones. The

*E-mail: cosmos@IT10242.spb.edu

1063-7737/04/3003-0169$26.00

plasma moves along the Oz axis; its normal velocity component undergoes a jump $\Delta u = u_z(0) - u_2 > 0$ at the front and is constant and equal to u_2 downstream of the front. The preshock ($z < 0$) velocity $u_z(z)$ can decrease smoothly from u_1 far from the front to a value of $u_z(0) < u_1$ if an appreciable fraction of the shock energy is spent on the acceleration of particles and the generation of a magnetic field.

Since the particles are accelerated near the front, we specify the source of energetic particles at the front in the form

$$Q(z) = q_0\delta(z), \tag{1}$$

which corresponds to uniform particle injection from the background plasma into acceleration by the shock front. The injection intensity q_0 can be expressed in terms of the dimensionless parameter $\chi < 1$—the fraction of the particle flux injected into acceleration: $q_0 = n_0 u_1 \chi$, where n_0 is the total preshock density of the hydrogen ions and neutral atoms. Neutral atoms are ionized at the front. Since the accelerated protons are drawn from the thermal background, we should specify a sink $Q_{\rm th}$ of thermal protons at the front,

$$Q_{\rm th}(z) = -Q(z), \tag{2}$$

which ensures that the electric charge and the number of particles are conserved.

We assume that there are an initial large-scale magnetic field $\mathbf{B}_1$ upstream of the front whose direction is specified by the polar angles θ and α and turbulent pulsations that contain random small-scale particle-scattering magnetic fields. In a turbulent medium, the relativistic and thermal particles will follow random paths. It is important that the direction of the magnetic field not coincide with the direction of the normal to the front. Otherwise, for uniform particle injection into acceleration at the front, the current can flow only along the Oz axis and, by symmetry, will not generate a magnetic field. The diffusion coefficients κ of the relativistic protons and the analogous coefficients D^p and D^e of the background nonrelativistic protons and electrons are different along and across the large-scale magnetic field. In addition, they are different in the preshock and postshock regions. Since the diffusion is anisotropic, the relativistic and background particles will produce an electric current that can have components along all three axes. Here, our goal is to estimate the magnetic field produced by this current.

Equations for the magnetic field in turbulent plasma with the extraneous current $\mathbf{j}$ generated by relativistic particles were derived previously (Dolginov and Toptygin 2003). However, in the problem considered here, the diffusion coefficients, the magnetic field, and the plasma parameter depend on the coordinates. Therefore, the equations for the magnetic field should also include the inhomogeneity of the medium:

$$\frac{\partial \mathbf{B}}{\partial t} = -\nabla\times(\nu\nabla\times\mathbf{B}) + \nabla\times[\mathbf{u}\times\mathbf{B}] + \frac{4\pi}{c}\nabla\times\nu_{\rm m}\mathbf{j}, \qquad \nabla\cdot\mathbf{B} = 0. \tag{3}$$

Here, $\nu_{\rm m}$ is the collisional magnetic viscosity averaged over an ensemble of turbulent pulsations, $\nu_{\rm turb} = \langle u'^2\rangle\tau_{\rm c}/3$ is the turbulent magnetic viscosity, $\nu = \nu_{\rm turb} + \nu_{\rm m}$ is the total viscosity, $\mathbf{u}$ is the regular velocity of the medium, $\mathbf{u}'$ is the turbulent velocity, and $\tau_{\rm c}$ is the turbulence correlation time. The quantities ν, $\nu_{\rm m}$, and $\mathbf{u}$ are assumed to be z-dependent.

CALCULATING THE CURRENT

The total extraneous current in a plasma is produced by relativistic protons as well as by background protons and electrons: $\mathbf{j} = \mathbf{j}^p + \mathbf{j}^e$. The currents produced by protons and electrons can be written as ($z \neq 0$)

$$j^p_\alpha = -e\kappa_{\alpha\beta}\frac{\partial N}{\partial x_\beta} - eD^p_{\alpha\beta}\frac{\partial n_p}{\partial x_\beta} + eu_\alpha(N + n_p) + \sigma^p_{\alpha\beta}E_\beta, \tag{4}$$

$$j^e_\alpha = eD^e_{\alpha\beta}\frac{\partial n_e}{\partial x_\beta} - eu_\alpha n_e + \sigma^e_{\alpha\beta}E_\beta, \tag{5}$$

where N is the density of the accelerated protons, n_p and n_e are the nonequilibrium additions to the background proton and electron densities, and $\mathbf{E}$ is the electric field that is produced by charge separation and that satisfies the electrostatic equation

$$\nabla\cdot\mathbf{E} = 4\pi e(N + n_p - n_e). \tag{6}$$

The quantities σ^e and σ^p are the electrical conductivities of the background plasma. The latter are related to its diffusion coefficients by (Alfvén and Fälthammer 1963)

$$\sigma^{e,p}_{\alpha\beta} = \frac{D^{e,p}_{\alpha\beta}}{4\pi r^2_{\rm D}}, \tag{7}$$

where $r_{\rm D} = \sqrt{T/4\pi n_0 e^2}$ is the Debye length, T is the temperature, and n_0 is the equilibrium density of the background protons or electrons.

In the steady-state case, the total current $\mathbf{j} = \mathbf{j}^p + \mathbf{j}^e$ as well as the individual proton and electron currents satisfy the equations

$$\nabla\cdot\mathbf{j} = \nabla\cdot\mathbf{j}^p = \nabla\cdot\mathbf{j}^e = 0. \tag{8}$$

Below, we consider the one-dimensional case and assume that the densities and currents are functions of one spatial coordinate z. Since the influence of the

self-consistent electric field on relativistic particles is negligible, it will suffice to include only the particle diffusion and convective transport by the motion of the medium in the equation for the density N. For steady-state acceleration, the equation is

$$\frac{d}{dz}\left\{-\kappa_{1,2}\frac{dN_{1,2}}{dz}+u_{1,2}N_{1,2}\right\}=q_0\delta(z). \quad (9)$$

Here, the subscripts 1 and 2 refer to the preshock and postshock regions, respectively; and $\kappa_{1,2}$ are the values of the diffusion coefficient κ_{zz} in the corresponding regions. Below, we use similar notation for the coefficients D^p and D^e. The diffusion coefficients κ and D themselves will be interpreted as the quantities averaged over the energy spectra of the relativistic and thermal particles, respectively, that generally depend on z.

Substituting the boundary conditions (Toptygin 1983) for the source on the right-hand side of Eq. (9),

$$N_1=N_2,$$
$$\kappa_1\frac{dN_1}{dz}-\kappa_2\frac{dN_2}{dz}-\Delta uN_{1,2}=q_0 \text{ at } z=0, \quad (10)$$

we find the solution of Eq. (9):

$$N_1(z)=N_0e^{-\zeta(z)}, \quad N_0=\frac{q_0}{u_2},$$
$$\zeta(z)=\int_z^0\frac{u_z(z')dz'}{\kappa_1(z')}, \quad z\le 0; \quad (11)$$
$$N_2=N_0, \quad z\ge 0.$$

The condition $\zeta(L)\approx 1$ specifies the distance L to which the accelerated particles can move upstream of the flow.

The nonrelativistic particle densities are adjusted to the relativistic proton distribution and should be determined at $z>0$ from Eqs. (4)–(8). These equations are

$$\frac{d}{dz}\left(-eD_1^p\frac{dn_p}{dz}+eu_z(z)n_p+\sigma_{zz}^pE_z\right)=0, \quad (12)$$
$$\frac{d}{dz}\left(eD_1^e\frac{dn_e}{dz}-eu_z(z)n_e+\sigma_{zz}^eE_z\right)=0.$$

Integrating this system and using (7), we obtain

$$E_z=4\pi er_{\rm D}^2\left(\frac{dn_p}{dz}-\frac{u_z(z)}{D_1^p}n_p\right) \quad (13)$$
$$=-4\pi er_{\rm D}^2\left(\frac{dn_e}{dz}-\frac{u_z(z)}{D_1^e}n_e\right).$$

This relation allows us to write the components of the total current by using Eqs. (4) and (5) as

$$j_x=-e\kappa_{xz}\frac{dN}{dz}+eu_z(z) \quad (14)$$
$$\times\left\{\frac{D_{xz}^e}{D_1^e}n_e-\frac{D_{xz}^p}{D_1^p}n_p\right\},$$
$$j_y=-e\kappa_{yz}\frac{dN}{dz}+eu_z(z)\left\{\frac{D_{yz}^e}{D_1^e}n_e-\frac{D_{yz}^p}{D_1^p}n_p\right\},$$
$$j_z=0,$$

where $N(z)$ is given by Eqs. (11), and all the diffusion coefficients can depend on z. Further calculations cannot be performed in general form and require additional approximations:

(1) The parameter

$$\left(\frac{ur_{\rm D}}{\kappa_1}\right)^2=\left(\frac{3ur_{\rm D}}{v\Lambda_{||}}\right)^2\ll 1 \quad (15)$$

is small in the phases of the interstellar medium under consideration. The ratio $3u/v<1$ for nonrelativistic shocks. The parameter $r_{\rm D}/\Lambda_{||}$ is very small, no larger than 10^{-13}, if we take $\Lambda_{||}\approx 10^{18}$ cm averaged over the Galactic disk (see Berezinskii *et al.* 1990). Even the growth of the magnetic field and turbulent pulsations near the front by several orders of magnitude cannot compensate for this smallness.

Since the above parameter is small, the plasma quasi-neutrality condition $N+n_p-n_e\approx 0$ follows from Eqs. (6) and (13). This condition is satisfied to within values on the order of this parameter. The nonuniformity scale length in the background particle distribution is the same as that for the accelerated protons; therefore, in order of magnitude, $n'_{p,e}\approx(u/\kappa_1)n_{p,e}$.

If the diffusion coefficients of the thermal particles are small,

$$D_1^{p,e}\ll\kappa_1, \quad (16)$$

and the terms with the derivatives in Eq. (13) may be disregarded; this yields $n_p/n_e\approx -D_1^p/D_1^e$. The quasi-neutrality condition gives

$$n_p\approx -N(z)\frac{D_1^p}{D_1^p+D_1^e}, \quad n_e\approx N(z)\frac{D_1^e}{D_1^p+D_1^e} \quad (17)$$

and allows us to obtain the preshock current density in this approximation:

$$j_x=eu_z(z)\left\{\frac{D_{xz}^e+D_{xz}^p}{D_1^e+D_1^p}-\frac{\kappa_{xz}}{\kappa_1}\right\}N(z), \quad (18)$$
$$j_y=eu_z(z)\left\{\frac{D_{yz}^e+D_{yz}^p}{D_1^e+D_1^p}-\frac{\kappa_{yz}}{\kappa_1}\right\}N(z),$$
$$j_z=0.$$

(2) If condition (16) is not satisfied, but the thermal particle diffusion is ambipolar, as is the case in neutral clouds and warm phase (Ruzmaikin *et al.* 1988), then the protons and electrons diffuse together with the

similar diffusion coefficients $D^e_{\mu\nu} \approx D^p_{\mu\nu}$, which are close, in order of magnitude, to the smaller coefficient. Using the quasi-neutrality condition, we find from Eq. (14) that

$$j_x = eu_z(z)\left\{\frac{D^p_{xz}}{D^p_1} - \frac{\kappa_{xz}}{\kappa_1}\right\}N(z), \qquad (19)$$

$$j_y = eu_z(z)\left\{\frac{D^p_{yz}}{D^p_1} - \frac{\kappa_{yz}}{\kappa_1}\right\}N(z),$$

$$j_z = 0.$$

For ambipolar diffusion, expressions (18) and (19) are identical.

The derived expressions show that a nonzero current density can arise in the model under consideration only in the presence of cross diffusion coefficients κ_{xz} and κ_{yz} and analogous diffusion coefficients for the background particles. In this case, the curl of the current that appears in Eq. (3) as the source is nonzero. If we denote the particle transport mean free path along the regular magnetic field $\mathbf{B}$ by Λ, then we will have the longitudinal, transverse, and Hall diffusion coefficients (see, e.g., Toptygin 1983)

$$\kappa_{||} = \frac{1}{3}v\Lambda, \quad \kappa_\perp = \kappa_{||}\frac{r_g^2}{r_g^2+\Lambda^2}, \qquad (20)$$

$$\kappa_{\rm H} = \kappa_{||}\frac{r_g\Lambda}{r_g^2+\Lambda^2}.$$

Here, v is the particle velocity, and $r_g = cp/eB_0$ is the particle gyroradius. The diffusion coefficients of the thermal particles can be expressed in a similar way, but their Larmor radii are much smaller than those of the relativistic protons, and their mean free paths are determined by distinctly different physical factors. Therefore, the mutual cancellation of the terms in the braces in Eqs. (18) and (19) is highly unlikely.

The diffusion coefficients in Eqs. (18) and (19) can be expressed in terms of (20) as

$$\kappa_{xz} = (\kappa_{||} - \kappa_\perp)\sin\theta\cos\theta\cos\alpha \qquad (21)$$

$$- \kappa_{\rm H}\sin\theta\sin\alpha,$$

$$\kappa_{yz} = (\kappa_{||} - \kappa_\perp)\sin\theta\cos\theta\sin\alpha + \kappa_{\rm H}\sin\theta\cos\alpha,$$

$$\kappa_1 = \kappa_{||}\cos^2\theta + \kappa_\perp\sin^2\theta.$$

The angles θ and α specify the direction of the large-scale field in a coordinate system with the polar axis directed along the normal to the plane of the front. The background particle diffusion coefficients have a similar structure. When interchanging the subscripts x, z and y, z on the left-hand sides of Eqs. (21), the sign of $\kappa_{\rm H}$ on their right-hand sides should be reversed.

Note that the existence of an electric current in a system in which the electric charge was offset with a high accuracy and exhibits no macroscopic motion is attributable to the nonuniformity in the distribution of the Larmor circles of individual (accelerated and background) particles. The current under consideration is similar to the magnetization current $\mathbf{j} = c\,\mathrm{curl}\,\mathbf{M}$ in macroscopic electrodynamics, where $\mathbf{M}$ is the nonuniform magnetization of the medium.

SELF-CONSISTENT CALCULATION OF THE MAGNETIC FIELD

An upper limit on the strength of the magnetic field produced by the mechanism under consideration can be estimated from the energy conservation law. The energy density of the preshock gas flow is $n_0 m_p u_1^2/2$ (the internal energy is disregarded). In our case, the relativistic particles, which may account for several tens of percent of the flow energy, act as an intermediate agent (Berezhko and Krymskii 1988; Toptygin 1997). Taking 20% for this fraction and assuming that $u_1 \approx 3\times10^8$ cm s^{-1} (a value typical of supernova explosions and strong stellar winds (Lozinskaya 1986)), we obtain an estimate of the magnetic field

$$\mathcal{B}_{\max} = \sqrt{0.1\times 8\pi n_0 m_p u_1^2}. \qquad (22)$$

These estimates for the main three known phases of the interstellar medium are given in Table 1. They are larger than the observed values of $B_{\rm obs}$ (see, e.g., Ruzmaikin *et al.* 1988; Beck 2001) in the corresponding phases by several orders of magnitude, which may suggest that the effect under consideration is significant. For this reason, we must find a self-consistent solution of the problem that is based on conservation laws and that takes into account the dependence of the parameters of the problem on the magnetic field being calculated.

We write the conservation laws by assuming that the plasma upstream of the shock front is cold and its pressure is negligible, $P_g \approx 0$. The plasma velocity u_1 far from the front has only a z component; i.e., it is normal to the front. However, a tangential component determined by the magnetic field appears near the front. The corresponding system of equations should include the magnetic field, and, in this sense, it generalizes the relations given by Toptygin (1997). We obtain the following system that expresses the constancy of the mass, momentum, and energy fluxes:

$$J = m_p n(z)u_z(z) = m_p n_0 u_1 = \mathrm{const}, \qquad (23)$$

$$Ju_z(z) + P_{\rm c}(z) + \frac{B_{\rm t}^2(z)}{8\pi} = Ju_1 + \frac{B_{1\rm t}^2}{8\pi}, \qquad (24)$$

$$J\mathbf{u}_{\rm t}(z) - \frac{1}{4\pi}B_{1z}\mathbf{B}_{\rm t}(z) = -\frac{1}{4\pi}B_{1z}\mathbf{B}_{1\rm t}, \qquad (25)$$

Table 1

n_0, protons cm^{-3}	$\mathcal{B}_{\max}$, G	$\nu_{\rm m}$, cm^2 s^{-1}	$B_{\rm obs}$, G	Note
20	2.8×10^{-3}	5×10^{21}	1.5×10^{-5}	Neutral clouds
0.2	2.8×10^{-4}	3×10^{20}	2×10^{-6}	Intercloud warm medium
2×10^{-3}	2.8×10^{-5}	5×10^{17}	?	Hot bubbles

$$\frac{1}{2}Ju_z^2(z)+\frac{\gamma_{\rm c}}{\gamma_{\rm c}-1}u_z(z)P_{\rm c}(z) \qquad (26)$$
$$-\frac{\kappa_1(z)}{\gamma_{\rm c}-1}\frac{dP_{\rm c}}{dz}+\frac{1}{4\pi}u_z(z)B_{\rm t}^2(z)+q_{\rm m}(z)$$
$$=\frac{1}{2}Ju_1^2+\frac{1}{4\pi}u_1B_{1\rm t}^2.$$

Here, $J=m_pn_0u_1$ is the mass flux density, $\gamma_{\rm c}$ is the Poisson adiabatic index of the relativistic gas of accelerated particles, $q_{\rm m}(z)$ is the energy flux of the escaping particles (for the latter to be calculated, we must know the energy spectrum of the accelerated particles), and $\mathbf{B}_{\rm t}=(B_x(z),B_y(z))$ denotes the projection of the total magnetic field onto the (x,y) plane parallel to the front. It includes both the initial field $\mathbf{B}_1$ and the additional field generated by the accelerated particles. By analogy, $B(z)=\sqrt{B_x^2(z)+B_y^2(z)+B_{1z}^2}$ is the magnitude of the total magnetic field.

The Maxwell equations (3) for the one-dimensional case under consideration take the form

$$\frac{d}{dz}\left(\nu\frac{dB_x}{dz}-u_zB_x-\frac{4\pi}{c}\nu_{\rm m}j_y\right)=0, \qquad (27)$$
$$\frac{d}{dz}\left(\nu\frac{dB_y}{dz}-u_zB_y+\frac{4\pi}{c}\nu_{\rm m}j_x\right)=0,$$
$$\frac{dB_z}{dz}=0.$$

The first integrals of system (27) can be easily determined:

$$\nu(z)\frac{dB_x}{dz}-u_z(z)B_x=\frac{4\pi}{c}\nu_{\rm m}(z)j_y(z)-u_1B_{1x}, \qquad (28)$$
$$\nu(z)\frac{dB_y}{dz}-u_z(z)B_y=-\frac{4\pi}{c}\nu_{\rm m}(z)j_x(z)-u_1B_{1y},$$
$$B_z(z)=B_{1z}=\text{const}.$$

The dependence of all diffusion coefficients on the total magnetic field should be taken into account in a self-consistent calculation. In particular, the trigonometric functions in (21) should be expressed as follows:

$$\cos\theta=\frac{B_{1z}}{B(z)},\quad \sin\theta\cos\alpha=\frac{B_x(z)}{B(z)}, \qquad (29)$$
$$\sin\theta\sin\alpha=\frac{B_y(z)}{B(z)}.$$

The ambipolar coefficient of collisional magnetic viscosity also depends on the magnetic field.

The solution of Eqs. (28) is significantly determined by the relation between the diffusion coefficients of the accelerated particles and the magnetic field. Since the nonuniformity in the magnetic field distribution is produced by the accelerated particles, the derivative $|B'_{x,y}|\le(u_1/\kappa_1)|B_{x,y}|$. It can be easily verified by estimation that, in most cases, the turbulent viscosity near the shock front is small compared to the collisional viscosity and $\nu\approx\nu_{\rm m}$. Thus, the relative role of the two terms on the left-hand sides of Eqs. (28) is determined by the factor $\nu_{\rm m}/\kappa_1$. Let us consider the following two cases:

(1) $\nu_{\rm m}/\kappa_1\ll1$. The term with the derivative may be disregarded, and the solution is

$$B_x(z)=-\frac{4\pi\nu_{\rm m}(z)}{cu_z(z)}j_y(z)+\frac{u_1}{u_z(z)}B_{1x}, \qquad (30)$$
$$B_y(z)=\frac{4\pi\nu_{\rm m}(z)}{cu_z(z)}j_x(z)+\frac{u_1}{u_z(z)}B_{1y}.$$

(2) $\nu_{\rm m}/\kappa_1\gg1$. In this case, an analytical solution can be obtained only for constant diffusion coefficients:

$$B_x(z)=\frac{4\pi\kappa_1}{cu_1}j_y(z)+B_{1x}, \qquad (31)$$
$$B_y(z)=-\frac{4\pi\kappa_1}{cu_1}j_x(z)+B_{1y}.$$

Solution (31) obtained for constant diffusion coefficients is also suitable, in order of magnitude, when there is a z dependence of the diffusion coefficients and the plasma velocity, if this dependence is smooth enough. In our case, this condition is satisfied, because the magnetic field changes appreciably only on the macroscopic scale $L=\kappa_1/u_1$.

Let us now estimate the field at the front. Let us specify the fraction η of the dynamic pressure of the

plasma flow transferred to the accelerated particles and the magnetic field generated by them:

$$\eta = \frac{P_c(0) + B^2(0)/8\pi - B_1^2/8\pi}{Ju_1}. \qquad (32)$$

We find from Eq. (24) that

$$\frac{u_z(0)}{u_1} = 1 - \eta. \qquad (33)$$

Below, in our numerical estimation, we specify η at a level that does not exceed 20%, although it can be larger by several times for intense acceleration.

The flux density $q_0 = N_0 u_2$ of the particles injected into acceleration can also be expressed in terms of the relative dynamic pressure η. We take into account the relation between the pressure P_c of the relativistic particles and their mean kinetic energy $\bar{T}$:

$$P_c = \frac{1}{3}\int vpN(p)p^2dp = \frac{\overline{vp}}{3}N_0 \qquad (34)$$
$$= (\gamma_c - 1)\bar{T}N_0.$$

Using (32), we obtain

$$q_0 = \frac{n_0 u_2}{(\gamma_c - 1)}\frac{m_p u_1^2}{\bar{T}}\left(\eta - \frac{B_t^2(0) - B_{1t}^2}{8\pi J u_1}\right). \qquad (35)$$

We begin our estimation of the field at the front with the case $\nu_m \gg \kappa_1$. We use Eqs. (19) for the current and write expressions (31) for the fields at the $z = 0$ front as

$$B_x(0) = -\frac{4\pi e q_0 \kappa_H}{cu_2}\left\{\frac{\kappa_{yz}}{\kappa_H} - \frac{\kappa_1}{\kappa_H}\frac{D_{yz}^p}{D_1^p}\right\} + B_{1x}, \qquad (36)$$

$$B_y(0) = \frac{4\pi e q_0 \kappa_H}{cu_2}\left\{\frac{\kappa_{xz}}{\kappa_H} - \frac{\kappa_1}{\kappa_H}\frac{D_{xz}^p}{D_1^p}\right\} + B_{1y}.$$

Let us consider intense particle acceleration at the front. In this regime, the transport mean free path takes on the lowest possible value of $\Lambda \approx r_g$, i.e., becomes on the order of the gyroradius (Bohm limit). This case is most likely in light of the studies of the generation of MHD turbulence by accelerated particles carried out by Lucek and Bell (2000) and Bell and Lucek (2001). They obtained very high turbulence levels.

In this case, relations (20) yield

$$\kappa_{||} = \frac{\overline{vp}}{3}\frac{c}{eB} = 2\kappa_\perp = 2\kappa_H. \qquad (37)$$

Here, the bar denotes an averaging over the spectrum of the accelerated particles. This averaging can be performed by using relation (34). Regarding the tensor $D_{\mu\nu}^p$, we only assume that $D_H^p \approx 0$, because the Larmor radii of thermal particles are small and because these coefficients have opposite signs for protons and electrons. In this case, the condition $D_{||}^p \gg D_\perp^p$ need not be satisfied, because the random magnetic field component can partially isotropize these coefficients. Let us also introduce the following dimensionless quantities under the assumption of $B_{1z} \neq 0$, $B_{1y} \neq 0$, and $B_{1x} = 0$:

$$X = \frac{B_x(0)}{B(0)}, \qquad Y = \frac{B_y(0)}{B(0)}, \qquad (38)$$
$$B^2(0) = \frac{B_{1z}^2}{1 - X^2 - Y^2}, \qquad d = \frac{D_\perp^p}{D_{||}^p - D_\perp^p} \geq 0.$$

Using (21), (29), and (34), we reduce Eqs. (36) to

$$X = -\left[\frac{b^2}{B_{1z}^2}(1 - X^2 - Y^2) - \frac{\gamma_c}{4}\right] \qquad (39)$$
$$\times \left[X + \frac{B_{1z}}{|B_{1z}|}\frac{(d-1)\sqrt{1 - X^2 - Y^2}}{d + 1 - X^2 - Y^2}Y\right],$$
$$Y = \left[\frac{b^2}{B_{1z}^2}(1 - X^2 - Y^2) - \frac{\gamma_c}{4}\right]$$
$$\times \left[-Y + \frac{B_{1z}}{|B_{1z}|}\frac{(d-1)\sqrt{1 - X^2 - Y^2}}{d + 1 - X^2 - Y^2}X\right]$$
$$+ \frac{B_{1y}}{|B_{1z}|}\sqrt{1 - X^2 - Y^2}.$$

Here, the parameter b^2, which has the dimensions of the square of the field, characterizes the free energy density of the gas flow with the initial magnetic field:

$$b^2 = 2\pi\gamma_c J u_1 \eta + \gamma_c B_1^2/4. \qquad (40)$$

The Poisson adiabatic index of the relativistic gas is $\gamma_c \approx 4/3$. The magnetic field b is of the same order of magnitude as the field $\mathcal{B}_{max}$ calculated above (see (22) and Table 1). For a strong shock, it is at least two orders of magnitude stronger than the observed field in the corresponding phases.

The possible field strengths at the front should be determined from the system of equations (39). Let us show that this system for $b^2 \gg B_{1z}^2$ has solutions at $X \ll 1$ and $Y \ll 1$. We retain the terms not higher than the first order in X, Y in system (39) and find from the linear system of equations

$$X = -\frac{b^2}{B_{1z}^2}\left[X + \frac{B_{1z}(d-1)}{|B_{1z}|(d+1)}Y\right], \qquad (41)$$
$$Y = \frac{b^2}{B_{1z}^2}\left[-Y + \frac{B_{1z}(d-1)}{|B_{1z}|(d+1)}X\right] + \frac{B_{1y}}{|B_{1z}|},$$

that

$$B_x(0) = -\frac{B_{1y}B_{1z}}{|B_{1z}|}\frac{\delta}{\xi(1+\delta^2)}, \qquad (42)$$
$$B_y(0) = \frac{B_{1y}}{\xi(1+\delta^2)},$$

where we introduced the auxiliary designations $\xi = b^2/B_{1z}^2$ and $\delta = (d-1)/(d+1)$. Here, $\xi \gg 1$ and δ does not exceed unity: $0 \le \delta^2 \le 1$. Therefore, the parallel components of the initial field at the front are suppressed by the secondary field generated by the electric current of accelerated particles. The suppression factor (on the order of 10^4 for intense acceleration) is large. Even when the fraction of the energy transferred to the accelerated particles decreases to $\eta = 10^{-4}$, a tenfold suppression of the field components directed along the front is retained. Other regimes of the shock transition, if available, should be determined from the nonsimplified system of equations (39). However, its numerical solution shows that all the real roots of this system are small compared to unity. Therefore, formulas (42) exhaust all the possible solutions; i.e., for uniform particle injection, only the magnetic field component normal to the front essentially remains near the front.

The solutions obtained do not allow passage to the limit $B_{1z} \to 0$, because, in this case, the conditions $X \ll 1$ and $Y \ll 1$ are incompatible with the equation $X^2 + Y^2 = 1$. The case of $B_{1z} = 0$ is probably also incompatible with the above inequality $\nu_m \gg \kappa_1$, because $\nu_m \propto B^2$ and $\kappa_1 \propto B^{-1}$ in the cold and warm phases, and this inequality is violated when the field is suppressed by the particles.

Let us now analyze the case of $\kappa_1 \gg \nu_m$. According to (30), the generated field is proportional to the collisional magnetic viscosity ν_m. It may be represented as $\nu_m = \nu_0(B(z)/B_1)^2$ in neutral clouds and a warm medium and as $\nu_m = \nu_0(B_1/B(z))$ in bubbles, where B_1 is the mean field in the corresponding phase, and ν_0 is the magnetic viscosity that corresponds to the mean field (Ruzmaikin *et al.* 1988). To generalize the equations to both cases, we assume that $\nu_m(z) = \nu_0\beta(z)$, where

$$\beta(z) = \begin{cases} B^2(z)/B_1^2, & \text{in neutral clouds and a warm medium} \\ B_1/B(z), & \text{in bubbles.} \end{cases} \qquad (43)$$

When substituting these quantities and components (19) of the current expressed in terms of the magnetic field, Eqs. (30) take the from

$$B_x(0) = \frac{B_{1x}}{1-\eta} + \beta(0)\left(H - \frac{B^2(0)}{h}\right) \qquad (44)$$
$$\times \left\{\frac{(\kappa_{||}/\kappa_\perp - 1)B_{1z}B_y(0) + (\kappa_H/\kappa_\perp)B(0)B_x(0)}{(\kappa_{||}/\kappa_\perp - 1)B_{1z}^2 + B^2(0)} - \frac{(D^p_{||}/D^p_\perp - 1)B_{1z}B_y(0) + (D^p_H/D^p_\perp)B(0)B_x(0)}{(D^p_{||}/D^p_\perp - 1)B_{1z}^2 + B^2(0)}\right\},$$

$$B_y(0) = \frac{B_{1y}}{1-\eta} - \beta(0)\left(H - \frac{B^2(0)}{h}\right) \qquad (45)$$
$$\times \left\{\frac{(\kappa_{||}/\kappa_\perp - 1)B_{1z}B_x(0) - (\kappa_H/\kappa_\perp)B(0)B_y(0)}{(\kappa_{||}/\kappa_\perp - 1)B_{1z}^2 + B^2(0)} - \frac{(D^p_{||}/D^p_\perp - 1)B_{1z}B_x(0) - (D^p_H/D^p_\perp)B(0)B_y(0)}{(D^p_{||}/D^p_\perp - 1)B_{1z}^2 + B^2(0)}\right\}.$$

Here, the factors H and h have the dimensions of magnetic induction:

$$H = \frac{1}{h}(8\pi J u_1 \eta + B_1^2), \quad h = \frac{2(\gamma_c - 1)c\bar{T}}{e\nu_0}. \qquad (46)$$

Regarding the particle diffusion coefficients, we make the same assumptions as those for the previous case (the Bohm limit). In variables X, Y and for $B_{1x} = 0$, the system of equations for neutral clouds and a warm medium takes the form

$$X = \left(\frac{H}{B_1} - \frac{B_{1z}^2}{hB_1(1 - X^2 - Y^2)}\right) \qquad (47)$$

$$\times \frac{|B_{1z}|}{B_1\sqrt{1-X^2-Y^2}} \times \left\{ \frac{X}{2-X^2-Y^2} + \frac{B_{1z}}{|B_{1z}|} \frac{Y\sqrt{1-X^2-Y^2}(d-1)}{(2-X^2-Y^2)(1+d-X^2-Y^2)} \right\},$$

$$Y = \frac{B_{1y}\sqrt{1-X^2-Y^2}}{|B_{1z}|(1-\eta)} - \left(\frac{H}{B_1} - \frac{B_{1z}^2}{hB_1(1-X^2-Y^2)} \right) \times \frac{|B_{1z}|}{B_1\sqrt{1-X^2-Y^2}} \left\{ -\frac{Y}{2-X^2-Y^2} + \frac{B_{1z}}{|B_{1z}|} \frac{X\sqrt{1-X^2-Y^2}(d-1)}{(2-X^2-Y^2)(1+d-X^2-Y^2)} \right\}. \quad (48)$$

The mean energy of an accelerated particle in (46) depends on the shape of the energy spectrum. For sufficiently strong acceleration, the spectral index in phase space is close to 4. In this case, the mean energy is (Toptygin 1997)

$$\bar{T} = \frac{cp_0}{3(\gamma_c - 1)} \ln\left(\frac{2p_m}{m_p c}\right),$$

where $p_0 \approx m_p u_1$ is the injection momentum, and p_m is the maximum momentum to which the particle is accelerated (below, we take $p_m = 100 m_p c$). This yields $\bar{T} \approx 0.8 \times 10^{-4}$ erg.

The ratio $H/B_1 \approx 10^2$–$10^5 \gg 1$ for typical parameters in the warm phase and in neutral clouds. In this case, system (47) and (48), like (39), has a solution at $X \ll 1$ and $Y \ll 1$. Linearizing the equations, we obtain

$$B_x(0) = B_{1y} \frac{2B_1^2 B_{1z}\delta}{B_{1z}^2 H(1-\eta)(1+\delta^2)}, \quad (49)$$

$$B_y(0) = -B_{1y} \frac{2B_1^2}{|B_{1z}|H(1-\eta)(1+\delta^2)}.$$

For bubbles, $B_1^2 H/B_{1z}^2$ should be substituted for H in (49).

Numerical solution of the nonsimplified system (47) and (48) shows that it has no real roots on the order of unity. Thus, only the magnetic field component normal to the front remains, as in the previous case.

However, result (49) is inapplicable for $B_{1z} \to 0$, and the orientation of the initial field along the front should be considered separately. We assume that $B_{1z} = B_{1x} = 0$ and $|B_{1y}| = B_1 \neq 0$ in system (44) and (45) and introduce the variables $X = B_x(0)/B_1$ and $Y = B_y(0)/B_1$. We seek a solution with $X = 0$. We obtain the following equation for Y:

$$Y^4 - \frac{hH}{B_1^2} Y^2 + \pm\frac{h}{B_1} Y \mp \frac{h}{B_1(1-\eta)} = 0. \quad (50)$$

Here, the upper and lower signs correspond to the conditions $B_y(0) > 0$ and $B_y(0) < 0$, respectively. The coefficients of Eq. (50) differ significantly in value: $hH/B_1^2 > 10^4$ and $h/B_1 < 10$ in the warm phase and neutral clouds for $\eta \approx 20\%$. Therefore, the equation has large and small roots that can be found approximately by omitting, in turn, the small terms in the equation. For $Y \ll 1$, we omit the term Y^4 in (50) and find from the quadratic equation that

$$Y = \pm\sqrt{\mp\frac{B_{1y}}{H(1-\eta)}} \pm \frac{B_1}{2H} \approx \pm\sqrt{\mp\frac{B_{1y}}{H(1-\eta)}}.$$

The solution obtained may be written as

$$B_y(0) = \mp B_{1y}\sqrt{\frac{|B_{1y}|}{H(1-\eta)}} \ll B_1. \quad (51)$$

For $Y \gg 1$, we retain the first two terms in (50) and find that

$$B_y(0) = \pm\sqrt{hH}, \qquad |B_y(0)| \gg B_1. \quad (52)$$

The numerical solutions of Eq. (50) are given in Table 2 for the cold and warm phases at $u_1 = 3 \times 10^8$ cm s^{-1}, $\gamma_c = 4/3$, and $\bar{T} = 8 \times 10^{-5}$ erg.

Thus, in this case, there are two states of the shock front for each set of parameters h, H, and η with small and large magnetic field strengths $B_y(0)$ at the front. The numerical values of all parameters are given in Table 2. We calculated h and H by using formulas (46) and the two values of $B_y(0)$ by using formulas (51) and (52). The possibility of several (in our case, two) steady-state solutions is a natural result for an open nonlinear and strongly nonequilibrium system. Whether the corresponding regimes occur in nature should be established by studying their stability against small perturbations. This is a separate problem that is not considered here.

DISCUSSION AND CONCLUSIONS

(1) We have solved the nonlinear self-consistent problem of the generation of a static magnetic field by the electric current of the particles accelerated at a flat unbounded MHD shock front. The parameters of the medium and the shock front were assumed to be close to those known from the observations of supernova explosions and presupernova stellar winds. We took into account the back reaction of the generated field on the particle diffusion tensors and the background plasma parameters near the front. We assumed that

Table 2

Phase	h, G	$\eta = 1\%$		$\eta = 20\%$	
		H, G	$B_y(0)$, G	H, G	$B_y(0)$, G
Cold					
$n_0 = 20$ protons cm^{-3}	6.66×10^{-7}	1.14	5.48×10^{-8}	22.72	1.36×10^{-8}
$\nu_0 = 5 \times 10^{21}$ cm^2 s^{-1}			8.7×10^{-4}		3.9×10^{-3}
$B_1 = 1.5 \times 10^{-5}$ G					
Warm					
$n_0 = 0.2$ protons cm^{-3}	1.11×10^{-5}	6.82×10^{-4}	1.1×10^{-7}	1.36×10^{-2}	2.71×10^{-8}
$\nu_0 = 3 \times 10^{20}$ cm^2 s^{-1}			8.7×10^{-5}		3.89×10^{-4}
$B_1 = 2 \times 10^{-6}$ G					

the particles were injected into acceleration at the shock front uniformly in space and stationarily in time (a uniform stationary injection). The preshock turbulence pulsation level was assumed to be fixed and constant.

We showed that the behavior of the solution depends significantly on the presence of a normal component of the external magnetic field in the preshock region far from the front. If this component is present, then the problem has a unique solution that corresponds to the absence of field components parallel to the front: they decrease by several orders of magnitude compared to their initial values. At the same time, the normal component does not change. Thus, in this case, the magnetic field lines in the preshock region acquire a direction perpendicular to the front. The secondary field generated by the accelerated particles destroys the parallel components of the initial field. The thickness of the preshock region is defined by the parameter $L = \kappa_1/u_1$, where $\kappa_1 \equiv \kappa_{1zz}$ is the diffusion coefficient of the accelerated particles, and u_1 is the front velocity. The magnetic field from the preshock region rearranged by accelerated particles is carried by the plasma flow into the postshock region.

The conclusion about the radial pattern of the magnetic field near the shock front has received observational confirmation. It follows from the polarization data for synchrotron radio emission (Reynolds and Gilmore 1993) that the mean magnetic field in young supernova remnants (the Tycho and Kepler supernovae, SN 1006) has a radial structure. We are planning to make a more detailed comparison of the theory being developed with observations in a special paper.

If the external field far from the front is parallel to the front, then the problem has two solutions. As in the previous case, one of them corresponds to the suppression of the initial field by several orders of magnitude. The second solution yields a strong field parallel to the front that can be two orders of magnitude stronger than the mean field known from observations in the cold (neutral) and warm phases of the interstellar medium.

The question as two which of these possibilities occurs in nature must be solved through observations and by studying the stability of both regimes of the shock transition. Here, we did not analyze the stability. However, on general physical grounds, we may hypothesize that a state with a weak field is stable. It corresponds to Prigogine's theorem on minimum entropy production in the steady state of a weakly nonequilibrium system under fixed external conditions. Clearly, in a state with a strong field, the entropy production is much larger than that in a state with a weak field. However, the system under consideration is a strongly nonequilibrium one. Therefore, its stability should be studied by a different method, for example, by the method of small perturbations. A similar study for a strong shock front, but with the generation of a magnetic field being disregarded, was carried out by Toptygin (1999).

It should be emphasized that the assumption of uniform particle injection into acceleration is of great importance in the problem under consideration. If the injection is nonuniform, which may stem, for example,

from the fact that the density of the medium upstream of the front is nonuniform, then currents parallel to the front will inevitably arise in the preshock region. These currents can generate an additional parallel field.

Significant limitations in our study are also the assumption that the plane front is unbounded and the fact following from it that the problem is one-dimensional. In reality, since the shock fronts in physical objects are bounded, each front acts as the source of a large-scale electric current that spreads over the Galaxy and that is capable of generating a magnetic field far from the front and not only in the preshock region (Dolginov and Toptygin 2003). Such more realistic problems in a nonlinear self-consistent statement with nonuniform (and nonstationary) injection and with bounded shock front can probably be solved only numerically.

ACKNOWLEDGMENTS

We wish to thank the referees for their valuable constructive remarks. This work was supported in part by the Russian Foundation for Basic Research (project nos. 01-02-16654 and 03-02-17433).

REFERENCES

1. V. Aksford, E. Lir, and Dzh. Skadron, in *Proceedings of X Leningrad Seminar on Cosmophysics* (Izd. FTI im. Ioffe, Leningrad, 1978), p. 125.
2. H. Alfvén and Fälthammer, *Cosmical Electrodynamics* (Oxford, 1963; Mir, Moscow, 1967).
3. R. Beck, Space Sci. Rev. **99**, 243 (2001).
4. A. R. Bell, Mon. Not. R. Astron. Soc. **182**, 147 (1978).
5. A. R. Bell and S. G. Lucek, Mon. Not. R. Astron. Soc. **321**, 433 (2001).
6. E. G. Berezhko, K. V. Elshin, and L. T. Ksenovantov, Zh. Éksp. Teor. Fiz. **109**, 3 (1996) [JETP **82**, 1 (1996)].
7. E. G. Berezhko and G. F. Krymskii, Usp. Fiz. Nauk **154**, 49 (1988) [Sov. Phys. Usp. **31**, 27 (1988)].
8. V. S. Berezinskii, S. V. Bulanov, V. L. Ginzburg, *et al.*, in *Cosmic Ray Astrophysics,* Ed. by V. L. Ginzburg (North-Holland, Amsterdam, 1990).
9. A. Z. Dolginov and I. N. Toptygin, Pis'ma Astron. Zh. **29**, 426 (2003) [Astron. Lett. **29**, 374 (2003)].
10. F. C. Jones and D. C. Ellison, Space Sci. Rev. **58**, 259 (1991).
11. G. F. Krymskii, Izv. Akad. Nauk SSSR, Ser. Fiz. **45**, 461 (1981).
12. T. A. Lozinskaya, *Supernovae and Stellar Wind. Interaction with Galactic Gas* (Nauka, Moscow, 1986).
13. S. G. Lucek and A. R. Bell, Mon. Not. R. Astron. Soc. **314**, 65 (2000).
14. S. P. Reynolds and D. M. Gilmore, Astron. J. **106**, 272 (1993).
15. A. A. Ruzmaikin, D. D. Sokolov, and A. M. Shukurov, *Magnetic Fields of Galaxies* (Nauka, Moscow, 1988) [in Russian].
16. I. N. Toptygin, *Cosmic Rays in Interplanetary Magnetic Fields* (D. Reidel, Dordrecht, Holland, 1985).
17. I. N. Toptygin, Zh. Éksp. Teor. Fiz. **112**, 1584 (1997) [JETP **85**, 862 (1997)].
18. I. N. Toptygin, Pis'ma Astron. Zh. **25**, 40 (1999) [Astron. Lett. **25**, 34 (1999)].
19. H. J. Völk and J. M. McKenzie, Astron. Astrophys. **116**, 191 (1982).

Translated by V. Astakhov

Astronomy Letters, Vol. 30, No. 3, 2004, pp. 179–186. Translated from Pis'ma v Astronomicheskiĭ Zhurnal, Vol. 30, No. 3, 2004, pp. 207–215.

Possible Crossing of the Termination Shock in the Solar Wind by the Voyager 1 Spacecraft

V. B. Baranov[1]* and E. A. Pushkar'[2]

[1] *Institute for Problems of Mechanics, Russian Academy of Sciences, pr. Vernadskogo 101, Moscow, 117526 Russia*

[2] *Moscow State Industrial University, Moscow, Russia*

Received July 29, 2003

Abstract—The solution of the classical problem of two-dimensional magnetohydrodynamic (MHD) interaction between two shocks (the angle between the interacting shocks and the slope of the magnetic field are arbitrary) obtained by Pushkar' (1995) is applied to the problem of interaction between interplanetary shocks and the solar wind termination shock (TS). The self-consistent kinetic–gasdynamic model of solar wind interaction with the supersonic flow of a three-component (electrons, protons, and hydrogen atoms) interstellar medium developed for the axisymmetric, steady-state case by Baranov and Malama (1993) is used as the stationary background against which the physical phenomenon under consideration takes place. The main physical process in this model is the resonant charge exchange between protons and hydrogen atoms. This paper is a natural continuation of our previous papers (Baranov *et al.* 1996a, 1996b). However, whereas attention in these papers was focused on the TS interaction with an interplanetary forward shock moving away from the Sun, here we consider the TS interaction with an interplanetary reverse shock (RS) moving toward the Sun with a velocity lower than the solar-wind velocity. We show that the TS–RS interaction can give rise to a new TS' that moves toward the Sun, i.e., toward Voyager 1 and Voyager 2. This phenomenon may be responsible for the unexpected suggestion made by some of the scientists that Voyager 1 already crossed TS in the past year. This conclusion was drawn from the interpretation of the intensity, energy spectra, and angular distributions of ions in the energy range from 10 keV to 40 MeV measured from this spacecraft. Our results show that Voyager 1 could cross TS' rather than TS. © *2004 MAIK "Nauka/Interperiodica"*.

Key words: *interplanetary medium, shock waves, heliosphere, interplanetary magnetic field.*

INTRODUCTION

The interaction of the solar wind with the gas flow of the local interstellar medium (LISM) gives rise, in particular, to a termination shock in the solar-wind plasma flow. The supersonic solar-wind velocity becomes subsonic when passing through this shock, which is below referred to as TS. According to theoretical models (see, e.g., the recent review by Baranov 2002), the heliocentric distance to TS in the head-on section of the heliosphere (from the incoming LISM flow) was estimated to be in the range from 80 to 100 AU, although this distance strongly depends on the poorly known LISM proton density.

Naturally, the attention of scientific community concerned with the heliospheric structure is riveted on Voyager 1. This spacecraft, first, is currently at the largest heliocentric distance (about 88 AU) compared to the other spacecraft (Voyager 2 and Pioneer 11) and, second, moves toward the incoming LISM flow. Therefore, the time this spacecraft will cross TS is of particular interest.

Until now, the experimental data obtained from Voyager 1 have given no reason to believe that it has crossed TS. Estimates of its trajectory and the most recent predictions based on improved parameters in the local interstellar medium suggested that the crossing will take place in 2004 or 2005. However, at an International conference of the European Geophysical Society in Nice, France (April 2003), Decker *et al.* (2003a) and Krimigis *et al.* (2003) presented the results of their measurements of the intensities, energy spectra, and angular distributions of ions in the energy range from 10 keV to 40 MeV with the LECP (Low Energetic Charged Particles) instruments onboard Voyager 1 and Voyager 2. These results were obtained from mid-2002 until early 2003, when Voyager 1 was at a heliocentric distance of 85–88 AU (at 34° north heliographic latitude), while Voyager 2 was at a heliocentric distance of 67–70 AU (at 24° south heliographic latitude). Since mid-2002,

*E-mail: baranov@ipmnet.ru

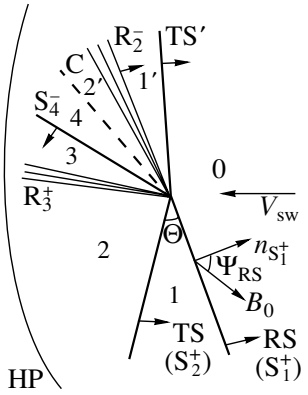

Fig. 1. Schematic pattern of the strong discontinuities and rarefaction waves produced by the interaction of an interplanetary reverse shock (RS) with the solar-wind termination shock (TS): 0, 1, 2, 3, 4, 1′, and 2′ are, respectively, the regions of the undisturbed solar wind between the fast shocks TS (S_2^+) and RS (S_1^+) (their classical MHD notation is given in parentheses), between TS and the fast rarefaction MHD wave R_3^+, between the last rarefaction wave and the slow MHD shock S_4^-, between the last shock and the contact discontinuity C, between the new TS′ formed after the interaction and the slow rarefaction MHD wave R_2^-, and between the last rarefaction wave and the contact discontinuity; HP and V_{SW} are the heliopause and the direction of the solar-wind velocity relative to TS; Θ and Ψ_{RS} are the angles between TS and RS and between the normal to RS and the direction of the interplanetary magnetic field B_0, respectively.

Voyager 1 detected a sharp increase in the ion intensity in this energy range, which had remained high for six months. This effect was not detected on Voyager 2, which was at an appreciably smaller heliocentric distance.

The question that the increase in the ion intensity at the energies under consideration could result from the TS crossing by Voyager 1 was unexpectedly raised at the above conference (Izmodenov 2003), because the interpretation of these measurements in terms of the Compton–Getting effect suggested a decrease in the solar-wind velocity to 100 km s^{-1}, which was attributed by Decker *et al.* (2003b) to the TS crossing. Since there were no plasma instruments operating onboard this spacecraft, data from the instrument that records magnetic fields at distances from 85 to 88 AU would be crucial. Unfortunately, such data have not yet been presented in detail in the literature.

Here, we explore one of the possibilities of the TS motion toward the spacecraft moving away from the Sun that is related to the TS interaction with strong (tangential, Alfvén, shock) discontinuities propagating in the interplanetary medium due to nonstationary processes on the Sun. Naturally, in this case, first, the encounter of Voyagers with TS will occur earlier, and, second, the parameters downstream of the new TS′ produced by this interaction will differ from the parameters downstream of TS (see, e.g., Baranov 2002). In contrast to our previous papers (Baranov *et al.* 1996a, 1996b), where we considered the TS interaction with interplanetary shocks moving relative to the frame of reference associated with the solar wind away from the Sun (the so-called forward shocks), here we consider the TS interaction with reverse shocks moving toward the Sun in the frame of reference associated with the solar wind. As previously (Baranov *et al.* 1996a, 1996b), we consider the interaction of an interplanetary shock incident on TS at an arbitrary angle (a two-dimensional problem), in contrast to Barnes (1993, 1994) and Naidu and Barnes (1994a, 1994b), who considered a one-dimensional problem.

In this short paper, we do not discuss other possibilities of the TS motion toward the Sun (the decrease in solar-wind dynamic pressure, the influence of interstellar magnetic fields, the enhanced LISM proton densities, etc.). The specific calculations for the problem considered below are based on the fundamental analytical study by Pushkar' (1995).

MATHEMATICAL FORMULATION OF THE PROBLEM

The result of the calculation of the interaction between the termination shock (TS) in the solar wind and the interplanetary shock (IS) incident on it depends on five dimensionless parameters:

$$\mathrm{M}_{\mathrm{TS}} = V_{\mathrm{TS}}/a_0, \quad \mathrm{M}_{\mathrm{RS}} = V_{\mathrm{RS}}/a_0,$$
$$\beta = 8\pi p/B^2, \Theta; \Psi_{\mathrm{RS}},$$

where M is the Mach number, V is the shock velocity relative to the solar wind, a_0 is the speed of sound in the plasma undisturbed by the shock, B is the magnitude of the magnetic induction vector, p is the static pressure, Θ is the angle of incidence of one shock on the other, and Ψ_{RS} is the angle between the interplanetary magnetic field (IMF) vector and the normal to the interplanetary shock front. The subscripts TS and RS refer, respectively, to the termination shock in the solar wind and the interplanetary reverse shock. The geometrical pattern of the shock interaction under consideration is shown in Fig. 1. It should be noted that Barnes (1993, 1994) and Naidu and Barnes (1994a, 1994b) carried out their studies for $\Theta = 0$ and $\Psi_{\mathrm{RS}} = \pi/2$, i.e., in the one-dimensional formulation. Below, the problem is considered in the two-dimensional formulation (for

arbitrary Θ and Ψ_{RS}). The mathematical formulation of the problem and the methods of solution were presented in detail previously (Pushkar' 1995; Baranov *et al.* 1996b).

As the model associated with the TS parameters, we will consider the axisymmetric, kinetic–gasdynamic model by Baranov and Malama (1993). According to this model, a spherically symmetric solar wind interacts with a supersonic flow of partially ionized LISM hydrogen plasma. Since the Knudsen number for neutral hydrogen atoms (the ratio of their mean free path during resonant change exchange with protons to the characteristic dimensions of the problem) is on the order of unity, the motion of hydrogen atoms can be described only in the kinetic approximation. In the model by Baranov and Malama (1993) under consideration, the Monte Carlo method with trajectory splitting developed by Malama (1991) is used instead of solving the linear Boltzmann equation for H atoms (the proton distribution function is assumed to be Maxwellian). The atom–atom collisions may be disregarded, because the mean free path for such collisions is much larger than the characteristic dimensions of the problem (in our case, the dimension of the heliopause, which is a tangential discontinuity that separates the solar-wind plasma and the LISM plasma). Figure 2 shows the geometrical pattern of the surfaces of strong discontinuities (the bow shock BS, the heliopause HP, and the termination shock TS in the solar wind) calculated by Baranov and Malama (1993) for the following parameters in the local interstellar medium (subscript ∞) and at the Earth's orbit (subscript E):

$$n_E(H^+) = 7\ \mathrm{cm}^{-3}, \quad V_E = 450\ \mathrm{km\ s}^{-1}, \quad M_E = 10,$$
$$n_\infty(H^+) = 0.07\ \mathrm{cm}^{-3}, \quad V_\infty = 25\ \mathrm{km\ s}^{-1},$$
$$\mu = 0.75, \quad n_\infty(H) = 0.14\ \mathrm{cm}^{-3}.$$

Here, $n(H^+)$ and $n(H)$ are the densities of the protons and the hydrogen atoms, respectively; and the parameter μ determines the ratio of the gravitational force of solar attraction to the force of radiative repulsion. At present, these values are taken as the reference values on the basis of the most recent measurements of the LISM and solar-wind parameters (see, e.g., the detailed review by Lallement 2001).

Interestingly, when interpreting the experimental data on scattered solar Lyman-alpha radiation from before 1985, the influence of the structure of the region between BS and TS on the penetration of hydrogen atoms from the LISM into the Solar system was completely ignored in the scientific literature (see, e.g., Bertaux *et al.* 1985), although Wallis (1975) and Baranov *et al.* (1979) showed at qualitative and quantitative levels, respectively, that the region between BS and HP (the outer heliosheath) is a good filter for the penetration of interstellar H atoms into the Solar system through their charge exchange with the protons decelerating in this region. For this reason, before 1985, the densities of the LISM H atoms were specified to be much lower than the above reference value. In fact, the low densities of the H atoms ($\sim$0.06 cm^{-3}) referred to the region upstream of TS rather than to the LISM.

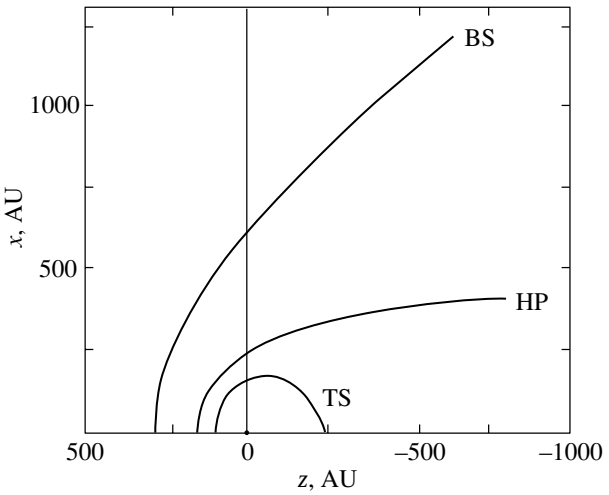

Fig. 2. Shapes and locations of the bow shock (BS), the heliopause (HP), and the solar-wind termination shock (TS) in the steady-state, axisymmetric model by Baranov and Malama (1993). The results of the numerical calculations for the parameters at the Earth's orbit and in the local interstellar medium presented in the text.

Since the problem of shock interaction is considered in the vicinity of the point of interaction, the curvature of the shocks may be disregarded (for more detail on the solution of such problems, see, e.g., Baranov *et al.* 1996a, 1996b; Barmin and Pushkar' 1990, 1991; Pushkar' 1995).

CALCULATIONS OF THE INTERACTION BETWEEN TS AND AN INTERPLANETARY REVERSE SHOCK

As was mentioned above, the reverse shock (RS) moves toward the Sun in the frame of reference associated with the solar wind, although it recedes from the Sun in the heliocentric frame of reference. This implies that region 1 between TS and RS in Fig. 1 is the state downstream of the the latter shock, and region 0 in this figure is the state before the passage of this shock, i.e., the state of the undisturbed solar wind. Interestingly, when the forward shock falls on TS, regions 1 and 0 are interchanged (Baranov *et al.* 1996a, 1996b).

In general, in addition to new shocks, the interaction between two MHD shocks can give rise to fast and slow rarefaction waves as well as Alfvén,

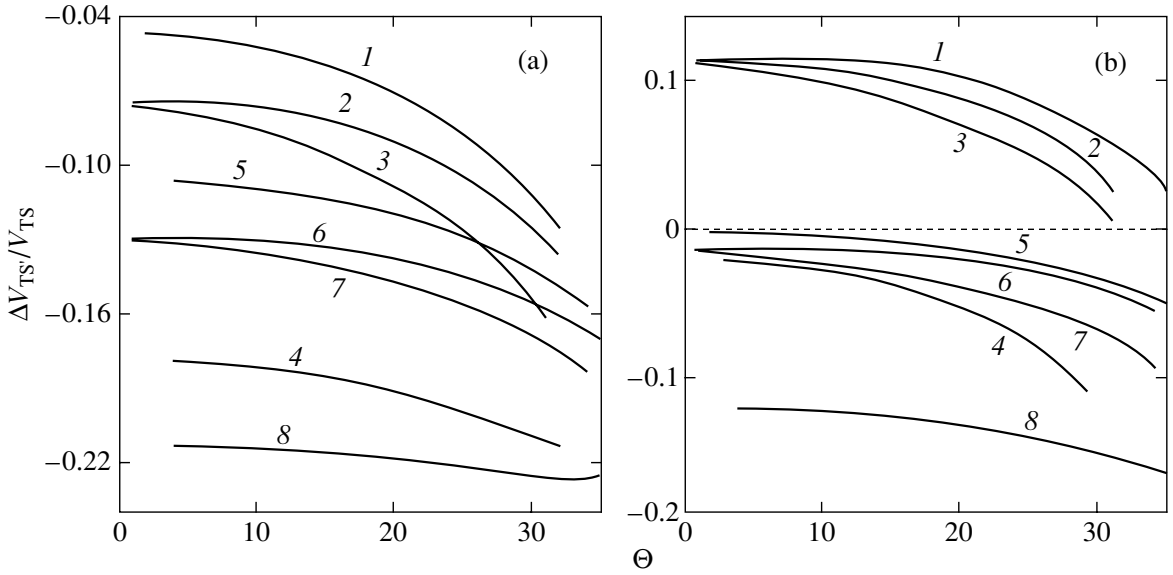

Fig. 3. Dimensionless velocity of the termination shock (TS′) formed after the interaction between TS and RS versus angle of inclination Θ between them for various angles Ψ_{RS}: (a) for $M_{RS} = 3$, $M_{TS} = 3.5$ (*1–4*), and 5 (*5–8*); for these curves, $\Psi_{RS} = 90°$, 50°, −50°, and 0°, respectively; (b) for $M_{RS} = 2$, $M_{TS} = 2$ (*1–4*), and 3.5 (*5–8*); for these curves, $\Psi_{RS} = 70°$, 90°, −70°, and 0°, respectively.

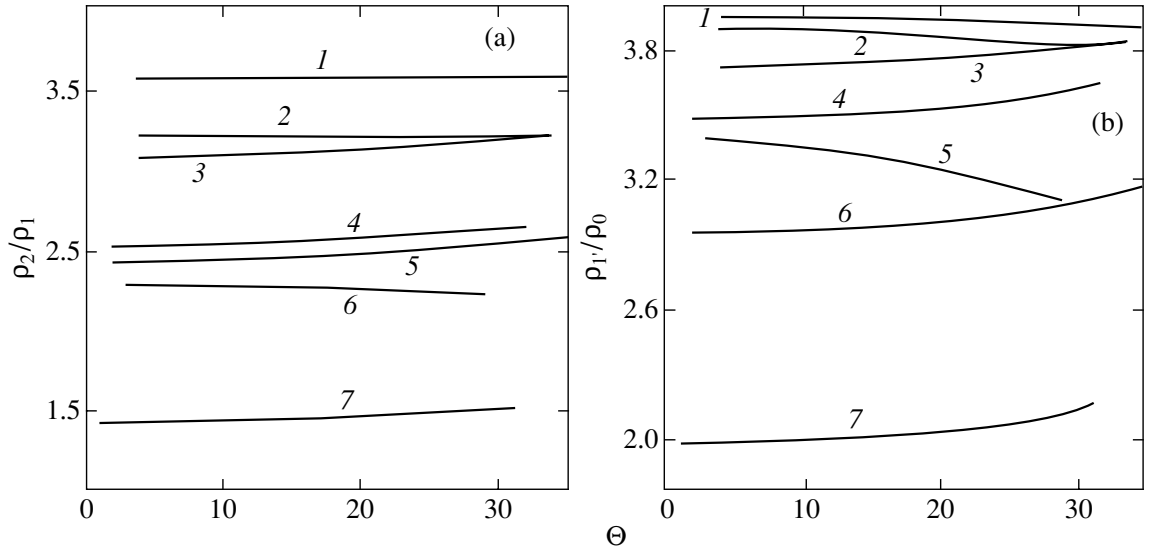

Fig. 4. Density jumps ρ_2/ρ_1 in TS (a) and $\rho_{1'}/\rho_0$ in TS′ (b) versus Θ for various M_{RS}, M_{TS}, and Ψ_{RS}: *1* and *2* for fixed $M_{RS} = 3$, $\Psi_{TS} = 0$, and $M_{TS} = 5$ and 3.5, respectively; *3* same as *1*, but for $\Psi_{RS} = 90°$; *4* same as *2*, but for $M_{TS} = 3.5$; curves *5*, *6*, and *7* were computed for a weak RS with a Mach number $M_{RS} = 2$; in this case, *5* for $M_{TS} = 3.5$ and $\Psi_{RS} = 90°$, *6* and *7* for $M_{TS} = 2$ and $\Psi_{RS} = 0°$ and 90°, respectively.

contact, and tangential discontinuities (Barmin and Pushkar' 1990, 1991; Pushkar' 1995; Baranov *et al.* 1996a, 1996b). As an example, Fig. 1 shows the result of the interaction between RS and TS. Here, TS transforms into TS′, while RS transforms into a fast rarefaction wave R_3^+, a slow shock S_4^-, a contact discontinuity C, and a slow rarefaction wave R_2^-.

We performed three series of calculations to determine the velocity of TS′ as well as the plasma density and the magnitude of the magnetic field downstream of it as functions of the angles Θ and Ψ_{RS} for various M_{TS} and M_{RS} and $\beta = 1$: (a) $M_{TS} = 3.5$; $M_{RS} = 2$, (b) $M_{TS} = 5$; $M_{RS} = 3$, (c) $M_{TS} = 2$; $M_{RS} = 2$. Case (a) approximately corresponds to the parameters used to compute the geometrical pattern shown

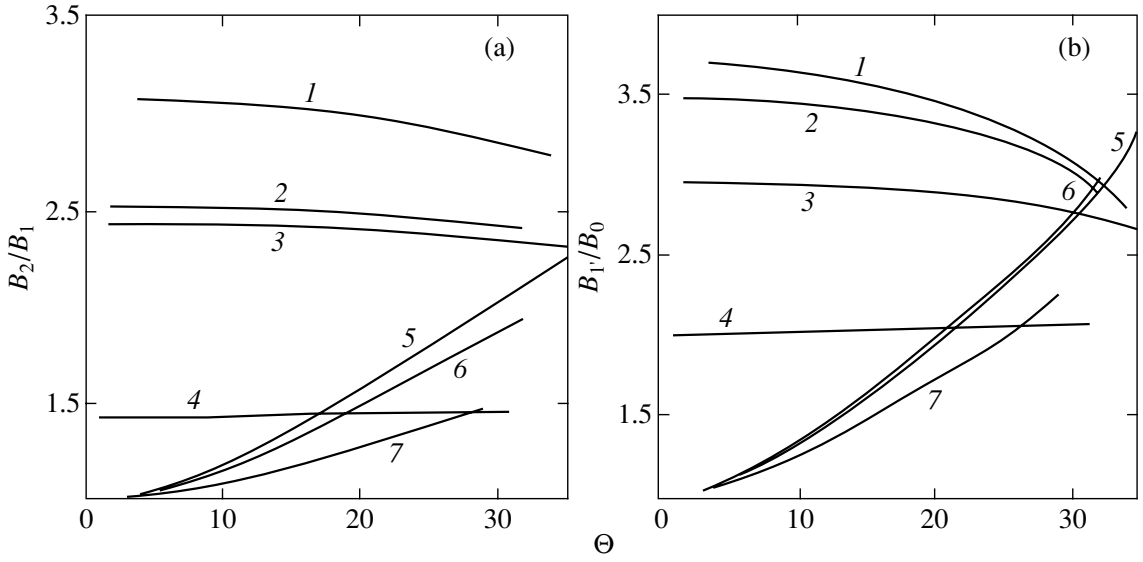

Fig. 5. Jumps in the magnitude of the magnetic field in TS (B_1/B_0) (a) and in TS′ ($B_{1'}/B_0$) (b) versus Θ for various M_{RS}, M_{TS}, and Ψ_{RS}: *1* and *2* for $M_{RS} = 3$, $\Psi_{RS} = 90°$, and $M_{TS} = 5$ and 3.5, respectively; *3* same as *2*, but for $M_{RS} = 2$; *4* same as *3*, but here (and in all such cases) the small Mach number for TS ($M_{TS} = 2$) was taken to simulate the passage of the forward shock through it; *5* and *6* for $M_{RS} = 3$, $\Psi_{RS} = 0$, and $M_{TS} = 5$ and 3, respectively; *7* same as *4*, but for $\Psi_{RS} = 0$.

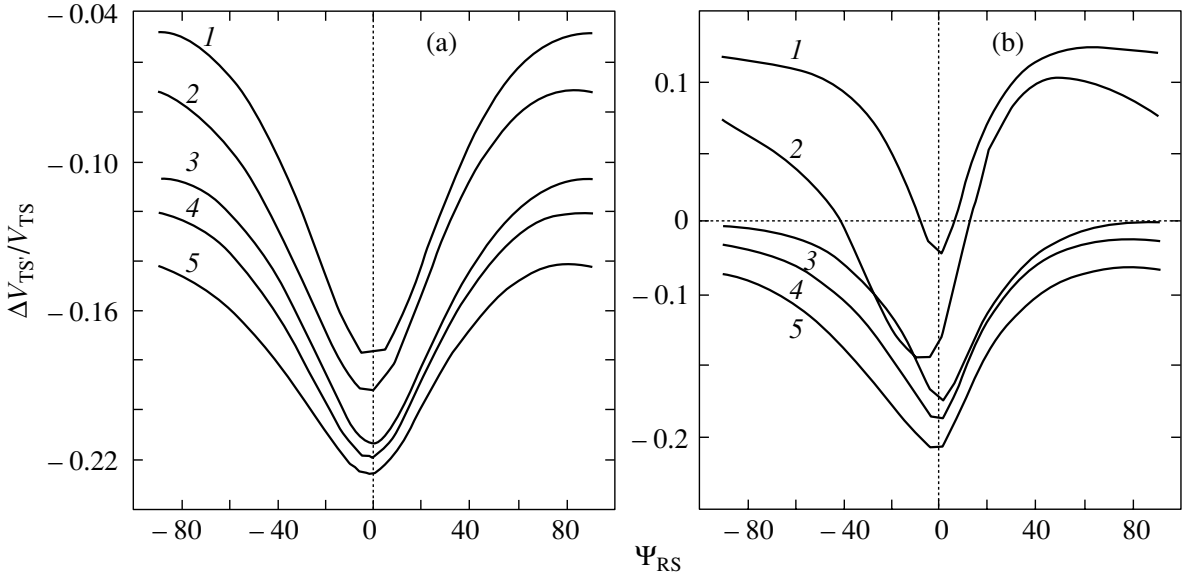

Fig. 6. Computed dimensionless velocity of the new termination shock TS′ after the interaction between TS and RS versus Ψ_{RS} for various angles Θ: (a) for $M_{RS} = 3$, *1* and *2* for $M_{TS} = 3.5$ and $\Theta = 5°$ and 20°, respectively, *3–5* for $M_{TS} = 5$ and $\Theta = 5°$, 20°, and 30°, respectively; (b) for a weak RS ($M_{RS} = 2$), *1* and *2* for $M_{TS} = 2$ and $\Theta = 5°$ and 25°, respectively, *3–5* for $M_{TS} = 3.5$ and $\Theta = 0°$, 20°, and 30°, respectively.

in Fig. 1 for a fairly weak RS; case (b) was computed for a slightly reduced density of the hydrogen atoms in the local interstellar medium (~ 0.1 cm^{-3}) at which the Mach number of the termination shock increases and for a fairly intense RS; and case (c) was used as a simulation of the preliminary interaction between TS and the forward shock.

The influence of resonant charge exchange leads to a deceleration and heating of the supersonic solar wind (Baranov 2002; Baranov and Malama 1993). For this reason, the Mach numbers for TS given

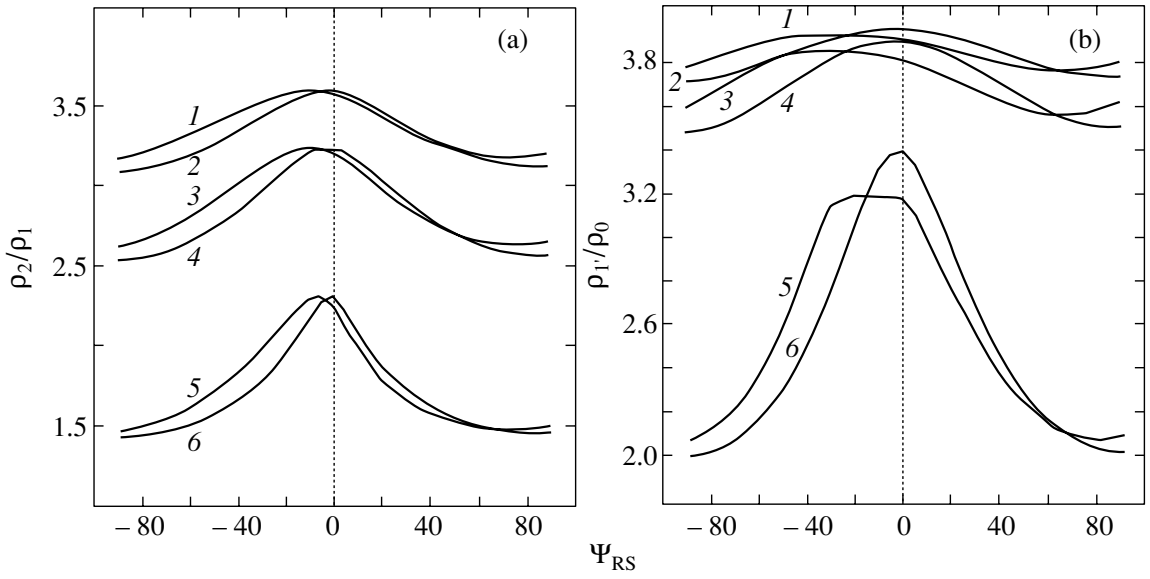

Fig. 7. Density jumps ρ_2/ρ_1 in TS (a) and $\rho_{1'}/\rho_0$ in TS′ (b) versus Ψ_{RS}: *1* and *2* for $M_{RS} = 3$, $M_{TS} = 5$ and $\Theta = 30°$ and 5°, respectively; *3* same as *1*, but for $M_{TS} = 3.5$; *4* same as *3*, but for $\Theta = 5°$; *5* and *6* for $M_{RS} = M_{TS} = 2$ and $\Theta = 25°$ and 5°, respectively.

above are much smaller than the Mach number for the solar wind at the Earth's orbit (at 1 AU). Figures 3–5 show the computed dependences for the dimensionless velocity of TS′ ($\Delta V_{TS'}/V_{TS} = (V_{TS} - V_{TS'})/V_{TS}$) in projection onto the normal to TS as well as the jumps in plasma density and magnetic field at this shock and at TS (after the RS passage) as functions of Θ for various angles Ψ_{RS}; Figs. 6–8 show the same computed parameters as functions of Ψ_{RS} for various angles Θ.

As we see from Fig. 3, the interaction of a weak RS ($M_{RS} = 2$) with TS that first interacted with the forward shock ($M_{TS} = 2$) can lead to the motion of TS′ away from the Sun (positive $\Delta V_{TS'}/V_{TS}$). Curve *4* in Fig. 3b, which corresponds to $\Psi_{RS} = 0$, constitutes an exception. Since the azimuthal IMF component far from the Sun is much larger than the radial IMF component, this case can be realized in polar heliospheric regions where $\Psi_{RS} \approx 0$.

In all the remaining cases, TS′ in the heliocentric frame of reference moves toward the Sun (toward Voyager 1 and Voyager 2). The velocity of the newly formed TS′ increases with Θ and M_{TS}. In the plane of the ecliptic, the IMF is almost parallel to the TS front. According to our calculations, this is possible, in particular, for $\Psi_{RS} \approx 90°$ and $\Theta \approx 0°$. Our calculations indicate that, in this case, the velocity of TS′ is $V_{TS'} \approx 0.1V_{TS}$ (curve *5* in Fig. 3a) or $V_{TS'} \approx 37.5$ km s^{-1} for the parameters used (see the table from the paper by Baranov *et al.* 1996a).

The jumps in densities and magnetic field in TS and TS′ are plotted against Θ for various M_{RS}, M_{TS}, and Ψ_{RS} in Figs. 4 and 5, respectively. Clearly, the solar-wind density ρ_1 and the magnetic field B_1 downstream of RS differ from the density ρ_0 and the magnetic field $B_0 \equiv B_{SW}$ in the undisturbed solar wind upstream of TS′. In particular, it follows from Fig. 4 that the density jump depends only slightly on the angle between the interacting MHD shocks RS and TS, although it strongly depends on their intensity and the inclination of RS to the interplanetary magnetic field. It follows from Fig. 5 that the jump in magnetic field in TS and TS′ also depends only slightly on Θ. The case where RS is a quasi-parallel shock (curves *5–7*) constitutes an exception. In this case, there is almost no jump in magnetic field at small angles Θ. Curves *4* in Fig. 5 show that the TS disturbance produced by the passage of the forward shock through it greatly reduces the jump in magnetic field.

Figures 6–8 show the same quantities as those in Figs. 3–5, but as functions of Ψ_{RS}. In these figures, we see a distinct strong dependence on the angle between the interplanetary magnetic field and RS. The minimum for almost all the calculated parameters occurs at small angles Ψ_{RS}. Interestingly, for a weak RS ($M_{RS} = 2$) and with an "effective" allowance made for the TS disturbance by the forward shock ($M_{TS} = 2$), regions of large angles Ψ_{RS} at which the reverse shock will recede from the Sun (positive $\Delta V_{TS'}$) appear. In all the remaining cases, the new TS′ produced

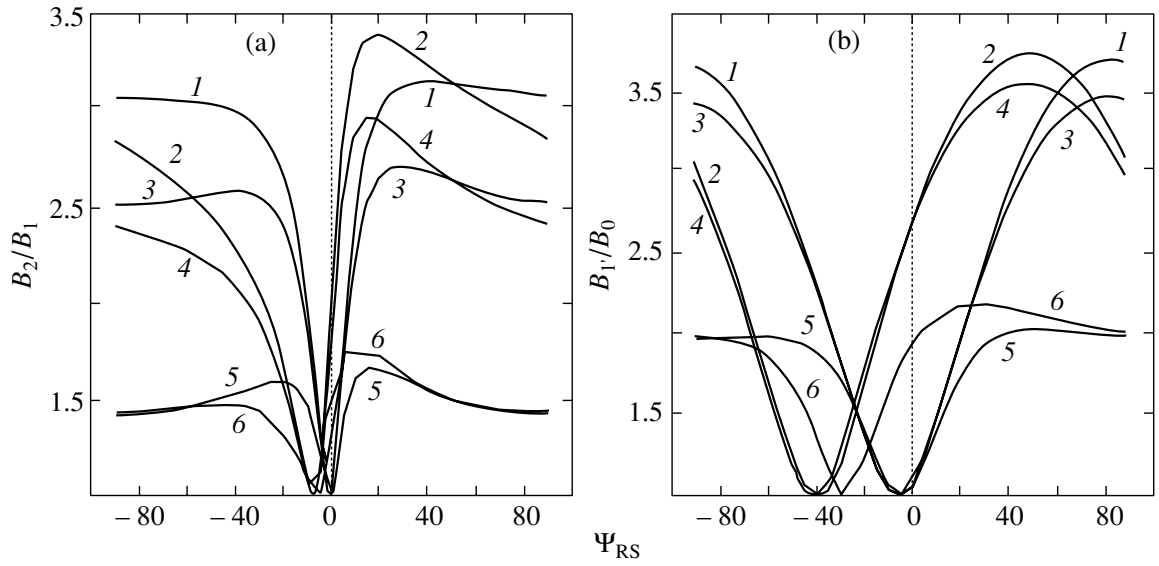

Fig. 8. Jumps in the magnitude of the magnetic field B_2/B_1 in TS (a) and $B_{1'}/B_0$ in TS′ (b) versus Ψ_{RS}: *1* и *2* for $M_{RS} = 3$, $M_{TS} = 5$ and $\Theta = 5°$ and 30°, respectively; *3* and *4* same as *1* and *2*, but for $M_{TS} = 3.5$; *5* and *6* for $M_{RS} = M_{TS} = 2$ and at $\Theta = 5°$ and 25°, respectively.

by the interaction of TS with RS will move toward the Sun, i.e., toward Voyager 1 and Voyager 2.

CONCLUSIONS

This paper is a continuation of our previous papers (Baranov *et al.* 1996a, 1996b), in which we considered the problem of interaction between an interplanetary forward shock and the solar-wind termination shock (TS) as an example of the general MHD problem of two-dimensional interaction between strong discontinuities (including shocks). We showed that, in most cases, the interaction of the interplanetary reverse shock with TS gives rise to a new TS′ that moves toward the Sun in the heliocentric frame of reference (as was shown in the above papers, the interaction of TS with the forward shock causes TS′ to move away from the Sun).

It follows from these results that Voyager 1 could cross TS′ much earlier than TS. It may well be that the interpretation of this crossing in the past year in terms of the Compton–Getting effect is correct. However, its seems that a careful analysis of the data from the magnetometer that operated during this time onboard Voyager 1 will be crucial. The motion of TS′ toward the Sun as a result of the MHD interaction between TS and RS also gives hope that Voyager 2 will possibly encounter with this shock in the near future. Since there are plasma instruments operating onboard Voyager 2, we hope that our comprehensive calculations of all parameters downstream of TS′ will help in interpreting the results of future measurements.

ACKNOWLEDGMENTS

Dr. Baranov wishes to thank the Russian Foundation for Basic Research (project nos. 01-01-00759 and 01-02-17551), INTAS (grant no. 01-270), the Program of Basic Research of OEMMPY of the RAS, and the International Space Study Institute (ISSI, Bern, the Physics of the Heliotail program) for their financial support. Pushkar' wishes to thank the RF Presidential Grant program (no. NSh-1697.2003.1) for Support of Young Russian Scientists and Leading Scientific Schools.

REFERENCES

1. V. B. Baranov, Usp. Mekh. **1**, 3 (2002).
2. V. B. Baranov, A. A. Barmin, and E. A. Pushkar', Pis'ma Astron. Zh. **22**, 620 (1996) [Astron. Lett. **22**, 555 (1996a)].
3. V. B. Baranov, A. A. Barmin, and E. A. Pushkar', J. Geophys. Res. **101**, 27 465 (1996b).
4. V. B. Baranov, M. G. Lebedev, and M. S. Ruderman, Astrophys. Space Sci. **66**, 441 (1979).
5. V. B. Baranov and Yu. G. Malama, J. Geophys. Res. **98**, 15 163 (1993).
6. A. A. Barmin and E. A. Pushkar', Izv. Akad. Nauk SSSR, Ser. Mekh. Zhidk. Gaza, No. 1, 131 (1990).
7. A. A. Barmin and E. A. Pushkar', Izv. Akad. Nauk SSSR, Ser. Mekh. Zhidk. Gaza, No. 3, 132 (1991).
8. A. Barnes, J. Geophys. Res. **98**, 15 137 (1993).
9. A. Barnes, J. Geophys. Res. **99**, 6553 (1994).
10. J. L. Bertaux, R. Lallement, V. G. Kurt, and E. N. Mironova, Astron. Astrophys. **150**, 1 (1985).
11. R. B. Decker, S. M. Krimigis, E. C. Roelof, and M. E. Hill, Geoph. Res. Abstracts **5**, 03301 (2003a).

12. R. B. Decker, S. M. Krimigis, E. C. Roelof, and M. E. Hill, in *Proceedings of the 28th International Cosmic Ray Conference* (Universal Acad. Press, 2003), p. 3773.
13. V. V. Izmodenov, private communication (2003).
14. S. M. Krimigis, R. B. Decker, and E. C. Roelof, Geophys. Res. Abstr. **5**, 03299 (2003).
15. R. Lallement, *The Century of Space Science* (Kluwer Acad., 2001), p. 1191.
16. Yu. G. Malama, Astrophys. Space Sci. **176**, 21 (1991).
17. K. Naidu and A. Barnes, J. Geophys. Res. **99**, 11 153 (1994a).
18. K. Naidu and A. Barnes, J. Geophys. Res. **99**, 17 673 (1994b).
19. E. A. Pushkar', Izv. Ross. Akad. Nauk, Ser. Mekh. Zhidk. Gaza, No. 6, 127 (1995).
20. M. Wallis, Nature **254**, 202 (1975).

Translated by V. Astakhov

Astronomy Letters, Vol. 30, No. 3, 2004, pp. 187–193. Translated from Pis'ma v Astronomicheskiĭ Zhurnal, Vol. 30, No. 3, 2004, pp. 216–223.

Characteristics of Weak Bursts of the Soft Component of Solar X-ray Radiation

I. K. Mirzoeva* **and O. B. Likin**

Space Research Institute, Russian Academy of Sciences, ul. Profsoyuznaya 84/32, Moscow, 117997 Russia

Received May 23, 2003

Abstract—We used the RF-15I-2 X-ray detector to study bursts of the soft component of the solar X-ray radiation. Weak bursts with fluxes less than 10^{-8} W m^{-2} were detected, and their characteristics were determined. © *2004 MAIK "Nauka/Interperiodica".*

Key words: *Sun*.

INTRODUCTION

The simplified physical mechanism of a solar flare can be described by dividing it into three phases: initial, explosive, and decay (hot) phases. Each phase has its own dominant mechanism: the turbulent heating of the current sheet, the generation of accelerated particles through the fracture or fractures of the current sheet, and the cooling of the hot region for the initial, explosive, and decay phases, respectively (Syrovatskii 1972). One might expect mostly thermal X-ray bursts in the energy range from 2 to 15 keV at the initial phase of the flare and mostly bremsstrahlung X-ray bursts in the harder X-ray spectral range superimposed on the thermal background due to the plasma heating in and near the current sheet at the explosive and decay phases. However, this mechanism seems to be too simplified, and the real pattern must be much more complex, especially since we have to deal with the softer X-ray spectral range where the burst amplitudes are small and the boundary between the thermal background and the X-ray burst proper produced by the flare is arbitrary.

Krucker *et al.* (2002) analyzed low-energy X-ray flares in the energy range from 3 to 12 keV using the RHESSI spectrometer, which is designed to detect the soft component of the solar X-ray radiation and to image the solar disk. These authors showed that the seven X-ray microflares detected during one hour are a superposition of the thermal and nonthermal components and are characterized by a very low energy content: 10^{26}–10^{27} erg.

Recall that the standard classification of X-ray bursts appears as follows:

Burst class	Burst flux (W m^{-2})
X	10^{-4}–10^{-3}
M	10^{-5}–10^{-4}
C	10^{-6}–10^{-5}
B	10^{-7}–10^{-6}
A	10^{-8}–10^{-7}

In this study, we were interested in low-flux ($<10^{-7}$ W m^{-2}) solar events that occurred at energies <15 keV. We also raised the question as to whether X-ray bursts with fluxes $<10^{-8}$ W m^{-2} could exist, i.e., whether there exists a class of weak X-ray bursts below the threshold of the above

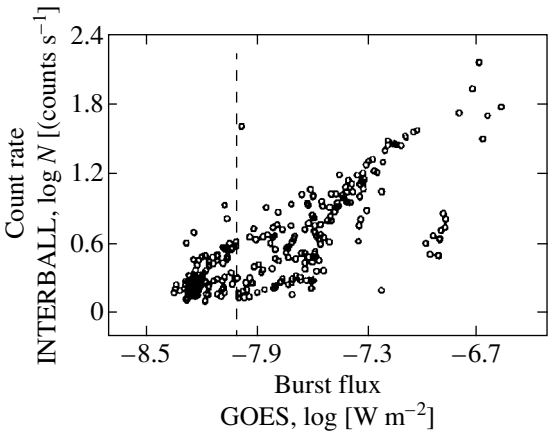

Fig. 1. Comparative diagram for weak bursts of the soft component of the solar X-ray radiation constructed from GOES and INTERBALL data from September through December 1995.

*E-mail: ikir@ares.iki.rssi.ru

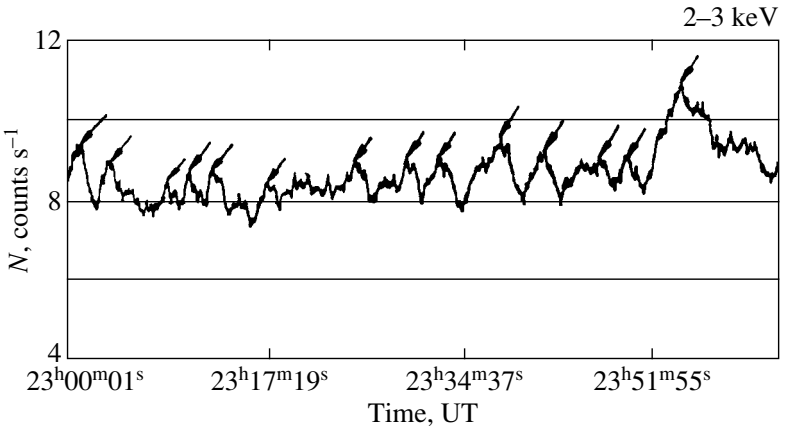

Fig. 2. Weak bursts of the soft component of the solar X-ray radiation recorded in the 2–3 keV channel on December 7, 1995, from 23^h00^m until 23^h59^m.

classification of X-ray bursts (below designated as class 0).

Interest in the lower threshold during observations of X-ray bursts was aroused by the idea that the explosive phase of the flare can be represented as a superposition of elementary flare bursts (Syrovatskii *et al.* 1982; Pisarenko and Likin 1995). According to Pisarenko and Likin (1995), a flare is a superposition of a number of elementary energy release events.

In 1998, a group of authors, including the designers of the RF-15I-2 instrument, detected X-ray bursts of very low flux ($< 10^{-7}$ W m^{-2}). These bursts have the following preliminary parameters: a rise time of 15–20 s, a duration of 40–45 s, a nearly triangular shape, and a statistically significant excess above the background (Likin *et al.* 1998).

DESCRIPTION OF THE EXPERIMENT

The Space Research Institute of the Russian Academy of Sciences together with the Astronomical Institute of the Czech Academy of Sciences and the Space Research Center of the Polish Academy of Sciences developed the RF-15I-2 instrument, a tail probe designed to study solar X-ray bursts, to carry out an experiment onboard the INTERBALL satellite. The instrument consists of a set of detectors to record the soft (2–15 keV) and hard (30–240 keV) components of the solar X-ray radiation.

The soft component was studied by using a proportional counter with a 100-μm-thick beryllium window and an area of 0.05 cm^2. Higher-energy bursts were recorded by using a scintillation counter with a NaI(Tl) crystal 8-mm in thickness and 50 mm in diameter. The proportional counter recorded X-ray radiation in four energy bands spanning the range from 2 to 15 keV, and the scintillation counter recorded X-ray radiation in four energy bands spanning the range from 15 to 240 keV (Farnick *et al.* 1995): (1) 2–3 keV; (2) 3–5 keV; (3) 5–8 keV; (4) 10–15 keV; (5) 15–30 keV; (6) 30–60 keV; (7) 60–120 keV, and (8) 120–240 keV. The time resolution was 0.1 and 2 s for channels 4–8 and 1–3, respectively. This time resolution and the relatively high sensitivity of the detector made it possible to study the fine structure of X-ray bursts (Likin *et al.* 1998).

RESULTS OF THE OBSERVATIONS

A detailed analysis of the data for X-ray bursts in 1995–2000 has revealed several characteristics of very weak X-ray bursts and allowed them to be determined accurately (Mirzoeva and Likin 2002a, 2002b).

In analyzing the numerical parameters of weak solar X-ray bursts, we chose the period that was most favorable for observations: from September to December 1995, when the passage to solar maximum began and when the number of bursts in the observed energy range was optimal, i.e., moderately large, which reduced the number of cases of the mutual superposition of events. We selected several periods from the data for this year in which no intense solar events were observed: September 2, 3, 4, and 23; October 20, 21, 23, and 24; November 4, 10, 11, 15, 16, 29, and 30; and December 7, 8, 11, 12, 14, 15, 22, and 23.

The total number of bursts recorded over the period under consideration was 296. Of these, there were:

16 bursts with 10^{-7}–10^{-6} W m^{-2} (class B);

139 bursts with 10^{-8}–10^{-7} W m^{-2} (class A); and

141 bursts with 10^{-9}–10^{-8} W m^{-2} (class 0).

Table 1. Parameters of weak bursts of the soft component of the solar X-ray radiation on December 7 and 15, 1995, measured onboard INTERBALL and GOES

INTERBALL				GOES				
time			maximum intensity above background, counts s^{-1}	time			burst flux, W m^{-2}	Class
beginning	end	maximum	background, counts s^{-1}	beginning	end	maximum		
December 7, 1995								
$18^h13^m46^s$	$18^h22^m02^s$	$18^m17^m08^s$	$\frac{2.275}{7}$	18^h14^m	18^h22^m	18^h16^m	8.67×10^{-9}	0
18 25 59	19 16 23	18 34 23	$\frac{23.65}{7}$	18 25	19 16	18 36	6.47×10^{-8}	A
19 48 59	19 58 45	19 54 11	$\frac{2.875}{7}$	19 49	19 59	19 53	9.25×10^{-9}	0
22 59 59	23 01 35	23 00 41	$\frac{1.375}{8}$	23 00	23 02	23 01	6.87×10^{-9}	0
23 01 35	23 06 15	23 03 15	$\frac{1}{8}$	23 01	23 06	23 04	6.55×10^{-9}	0
23 07 23	23 09 29	23 08 19	$\frac{0.475}{8}$	23 07	23 10	23 09	6.37×10^{-9}	0
23 09 29	23 10 55	23 10 07	$\frac{0.675}{8}$	23 09	23 11	23 10	6.48×10^{-9}	0
23 10 55	23 13 17	23 12 59	$\frac{0.6}{8}$	23 10	23 13	23 12	6.43×10^{-9}	0
23 16 01	23 17 39	23 16 21	$\frac{1.475}{7}$	23 19	23 21	23 20	6.68×10^{-9}	0
23 23 19	23 25 19	23 24 19	$\frac{1.1}{8}$	23 23	23 25	23 24	8.02×10^{-9}	0
23 27 47	23 29 43	23 28 37	$\frac{1.15}{8}$	23 28	23 30	23 29	7.64×10^{-9}	0
23 29 43	23 32 35	23 31 15	$\frac{1.13}{8}$	23 29	23 32	23 31	6.84×10^{-9}	0
23 32 35	23 38 17	23 36 37	$\frac{1.6}{8}$	23 32	23 38	23 35	8.38×10^{-9}	0
23 38 37	23 41 23	23 40 23	$\frac{1.3}{8}$	23 39	23 43	23 42	8.28×10^{-9}	0
23 41 23	23 46 15	23 45 38	$\frac{1.25}{8}$	23 41	23 46	23 45	8.13×10^{-9}	0
23 46 15	23 48 29	23 47 09	$\frac{1.75}{8}$	23 46	23 48	23 47	9.1×10^{-9}	0
23 48 29	23 59 25	23 51 49	$\frac{2.975}{8}$	23 48	23 59	23 56	9.66×10^{-9}	0

Table 1. (Contd.)

INTERBALL				GOES				
time			maximum intensity above background, counts s^{-1}	time			burst flux, W m^{-2}	Class
beginning	end	maximum	background, counts s^{-1}	beginning	end	maximum		
December 15, 1995								
$0^h17^m37^s$	$0^h38^m45^s$	$0^h27^m17^s$	$\frac{5.8}{8}$	0^h17^m	0^h38^m	0^h26^m	1.56×10^{-8}	A
1 31 57	1 35 39	1 33 45	$\frac{2.4}{8}$	1 31	1 35	1 32	8.71×10^{-9}	0
2 27 17	2 28 59	2 27 59	$\frac{2.25}{8}$	2 27	2 28	2 28	7.67×10^{-9}	0
2 53 29	2 54 29	2 54 11	$\frac{2.05}{8}$	2 53	2 54	2 52	6.92×10^{-9}	0
3 18 51	3 21 13	3 20 11	$\frac{1.5}{8}$	3 18	3 21	3 20	7.33×10^{-9}	0
3 21 45	3 36 53	3 22 23	$\frac{1.55}{8}$	3 21	3 36	3 23	7.64×10^{-9}	0
3 41 19	3 45 15	3 42 39	$\frac{2.5}{7}$	3 41	3 45	3 42	7.67×10^{-9}	0
4 21 31	4 24 45	4 23 57	$\frac{2.45}{7}$	4 21	4 24	4 23	6.58×10^{-9}	0
8 18 07	8 20 37	8 19 13	$\frac{2.3}{7}$	8 19	8 21	8 18	5.66×10^{-9}	0
9 44 35	9 46 11	9 45 13	$\frac{2.25}{7}$	9 44	9 46	9 45	6.05×10^{-9}	0
10 23 15	10 25 39	10 24 59	$\frac{2.25}{7}$	10 23	10 25	10 24	5.71×10^{-9}	0
12 34 25	12 36 47	12 35 33	$\frac{2.4}{7}$	12 35	12 37	12 36	6.32×10^{-9}	0

Below, we compare the GOES and INTERBALL data (Fig. 1). We used the GOES data to confirm the existence of weak bursts. The close match between the data from the two independent detection sources gives hope that the solar events under study are real. We took the GOES data from the Internet at www.ngdc.noaa.gov.

In Fig. 1, the count rate of the RF-15I-2 detector in the 2–3 keV channel (INTERBALL) is along the vertical axis, and the flux of X-ray bursts in the 1.5–12 keV channel (GOES) is along the horizontal axis. The dotted line on the horizontal axis indicates a 10^{-8} W m^{-2} level. It can be easily seen that 0-class bursts in this diagram lie in the tail of the distribution of fluxes below the 10^{-8} W m^{-2} level—to the left of the dotted boundary. The diagram shown in Fig. 1 represents a linear relation.

According to Kurochka (1987), who analyzed the

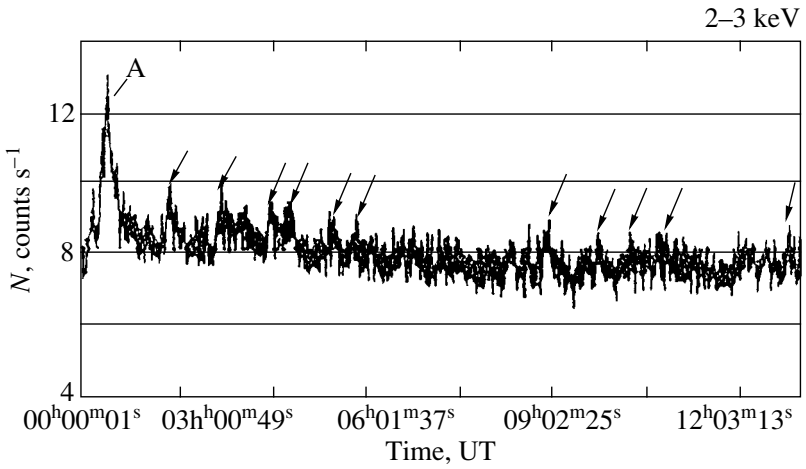

Fig. 3. Weak bursts of the soft component of the solar X-ray radiation recorded in the 2–3 keV channel on December 15, 1995, from 0^h0^m until 12^h48^m.

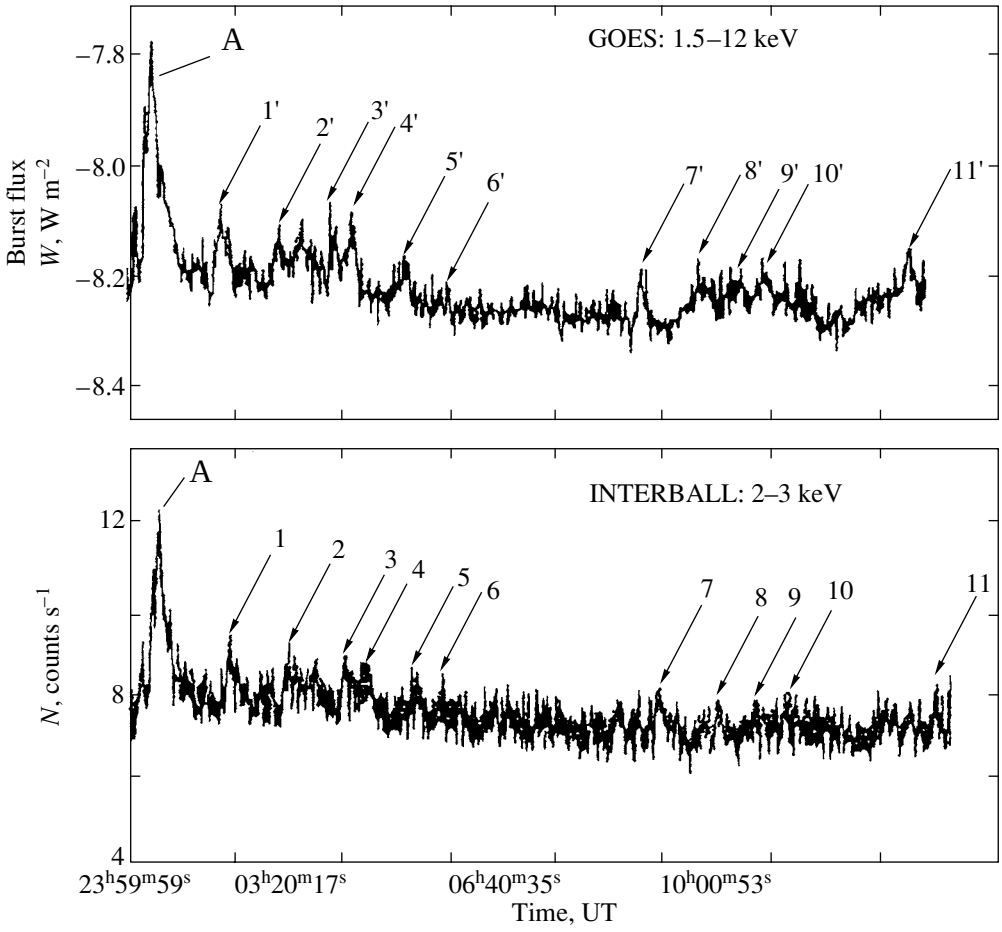

Fig. 4. Comparison of the time profiles for the weak bursts of the soft component of the solar X-ray radiation recorded on board GOES and INTERBALL on December 15, 1995, from $0^h17^m37^s$ until $12^h35^m33^s$.

Table 2. Mean parameters for weak class-0 bursts of solar soft X-ray radiation

Date, 1995	Mean duration	Mean rise time	Mean maximum intensity above background	Mean background level	Mean burst flux, W m^{-2}
November 11	8^m44^s	4^m48^s	3.65	10	2.04×10^{-9}
November 30	8 20	3 42	3.15	7	8.91×10^{-9}
December 7	4 07	2 04	1.4	8	7.7×10^{-9}
December 8	4 04	1 34	1.5	7	5.95×10^{-9}
December 12	1 47	1 24	1.1	9	9.95×10^{-9}
December 14	2 23	1 20	1.2	8	7.8×10^{-9}
December 15	3 42	1 12	2.2	7.5	6.93×10^{-9}
December 22	5 07	2 42	1.6	6.6	5.8×10^{-9}
December 23	6 06	2 26	1.5	9	9.5×10^{-9}
Generalized means					
	4^m58^s	2^m22^s	2.2	8	7.1×10^{-9}

energy distribution of 15 000 solar flares observed in 1978–1979, their number rapidly increases with decreasing energy to 10^{28} erg. As the energy of the flares decreases further, their number rapidly decreases, and the maximum in the distribution cannot be the result of incompleteness of the observational data. In our view, the energy distribution of solar flares may have a lower limit. If there were no lower limit on the flux of X-ray bursts, then the number of weak solar events would increase infinitely with decreasing flux. However, no such behavior has been observed so far. We detected a comparable number of class-A (139) and class-0 (141) bursts during the period under consideration.

Table 1 gives parameters of the weak bursts of the soft component of the solar X-ray radiation on December 7 and 15, 1995. All INTERBALL observations of weak bursts are confirmed by GOES measurements. Figures 2 and 3 show time intensity profiles for the weak bursts of the soft component of the solar X-ray radiation recorded by the RF-15I-2 instrument in the 2–3 keV channel from $23^h01^m35^s$ until $23^h51^m49^s$ on December 7 and from $0^h17^m37^s$ until $12^h35^m33^s$ on December 15, 1995. The class-0 bursts are marked by arrows. The amplitudes of the bursts recorded on December 7 and 15 lie within the ranges 0.5–3 and 1.5–2.5 counts s^{-1}, respectively. The class-0 bursts recorded on December 7 and 15 have fluxes of 6.4×10^{-9}–9.7×10^{-9} and 5.7×10^{-9}–8.7×10^{-9} W m^{-2}, respectively. The class-A burst recorded on December 15 has the following parameters: it began at $0^h17^m37^s$, it ended at $0^h38^m45^s$, it reached its maximum at $0^h27^m17^s$, and it had an amplitude of 5.8 counts s^{-1} at a thermal background level of 8 counts s^{-1}, and a burst flux of 1.7×10^{-8} W m^{-2}.

Figure 4 compares the time profiles for the weak bursts of solar X-ray radiation recorded onboard GOES and INTERBALL on December 15, 1995, from $0^h17^m37^s$ until $12^h35^m33^s$ (the time resolution of the GOES data is 1 min). The class-0 bursts are marked by arrows and denoted by the corresponding numbers. The time profiles are seen to closely coincide.

Table 2 gives the mean parameters of the weak class-0 bursts for the period under consideration. As we see from Table 2, the mean burst duration is 5 ± 2^m, the mean maximum burst intensity is 2.2 counts s^{-1} above the background level (for background levels 8–2 counts s^{-1}), the shape is nearly triangular, and the mean burst flux is 7.1×10^{-9} W m^{-2}. On December 14 and 22, 1995, solar events with the smallest duration and burst flux, respectively, were recorded:

—December 14. The minimum duration is 36 s (the beginning at $18^h30^m39^s$, the end at $18^h31^m15^s$, the maximum at $18^h30^m57^s$), the rise time is 18 s, the maximum burst intensity above the background is 1.5 counts s^{-1} (at a background level of 8 counts s^{-1}), and the burst flux is 6.5×10^{-9} W m^{-2}.

—December 22. The minimum burst flux is 4.5×10^{-9} W m^{-2} (the beginning is at $18^h43^m24^s$, the end

is at $18^h46^m06^s$, and the maximum is at $18^h45^m02^s$), the duration is 2^m42^s, and the maximum burst intensity above the background level is 1.2 counts s^{-1} (for a background level of 6 counts s^{-1});

CONCLUSIONS

A total of 139 class-A and 141 class-0 bursts were detected from September 2 through December 23, 1995.

The class-0 X-ray burst recorded in the energy range from 2 to 15 keV has the following parameters:

—duration 36–300 s,

—burst flux 4.5×10^{-9}–10^{-8} W m^{-2},

—maximum burst intensity above the background level 1–5 counts s^{-1},

—thermal background level 6–10 counts s^{-1}.

The total numbers of class-A and class-0 bursts are comparable over the period under study.

REFERENCES

1. F. Farnik, J. Sylwester, and O. Likin, *INTERBALL Mission and Payload* (CNES, IKI, RSA, 1995), p. 256.
2. S. Krucker, S. Christe, R. P. Lin, *et al.*, Solar Phys. **210**, 445 (2002).
3. L. N. Kurochka, Astron. Zh. **64**, 443 (1987) [Sov. Astron. **31**, 231 (1987)].
4. O. B. Likin, N. F. Pisarenko, F. Farnik, *et al.,* Kosm. Issled. **36**, 305 (1998).
5. I. K. Mirzoeva and O. B. Likin, Preprint No. Pr-2046, IKI RAN (Moscow Inst. Cosm. Res., Russian Academy of Sciences, 2002a).
6. I. K. Mirzoeva and O. B. Likin, Preprint No. Pr-2047, IKI RAN (Moscow Inst. Cosm. Res., Russian Academy of Sciences, 2002b).
7. N. F. Pisarenko and O. B. Likin, Izv. Ross. Akad. Nauk, Ser. Fiz. **59**, 37 (1995).
8. S. I. Syrovatskii, Soln. Zemn. Fiz. **3**, 106 (1972).
9. S. I. Syrovatskii, S. V. Bulanov, and V. A. Dogel', Itogi Nauki Tekh., Ser. Astron. **21**, 190 (1982).

Translated by A. Dambis

Astronomy Letters, Vol. 30, No. 3, 2004, pp. 194–199. Translated from Pis'ma v Astronomicheskiĭ Zhurnal, Vol. 30, No. 3, 2004, pp. 224–230.

The Influence of a Finite Conductivity on the Spectrum of Solar *p*-Modes

V. I. Zhukov*

Pulkovo Astronomical Observatory, Russian Academy of Sciences, Pulkovskoe shosse 65, St. Petersburg, 196140 Russia

Received February 21, 2003

Abstract—We consider the influence of a finite conductivity on the spectrum of solar *p*-modes (by taking into account their absorption at cusp resonance levels) in a plane two-layer model that consists of an upper isothermal layer with a uniform horizontal magnetic field and a lower adiabatic layer with a linear increase in temperature with depth. We show that an allowance for the finite, but high conductivity of the medium is required only to calculate the eigenfrequencies of the *p*-modes for which the resonance levels are located almost at the interface between the layers. © *2004 MAIK "Nauka/Interperiodica".*

Key words: *Sun, p-mode spectrum.*

INTRODUCTION

The influence of an atmospheric magnetic field on the spectrum of solar *p*-modes has been studied for more than fifteen years. Initially, attempts to take into account the influence of a magnetic canopy on the spectrum of *p*-modes were aimed at understanding the cause of the small (on the order of a few μHz) differences between the theoretically calculated and observed frequencies of the *p*-modes and the small variations in the frequencies of the *p*-modes with solar-cycle phase (Campbell and Roberts 1989; Evans and Roberts 1990; Jain and Roberts 1994a, 1994b). However, it soon became clear that the Alfvén and cusp resonance levels for *p*- and *f*-modes are located in the region of the magnetic canopy. Therefore, the influence of the magnetic canopy does not reduce to a simple change in oscillation eigenfrequencies. The presence of resonance levels leads not only to a change in eigenfrequencies, but also to resonant atmospheric heating, which allows us to look at the problem of the nonradiative heating of the solar atmosphere from a new perspective (Zhukov 1992, 1997a).

Beginning with the paper by Schwarzschild (1948) and up to now, the wave theory of heating has been considered as a possible mechanism of the nonradiative heating of the upper solar atmosphere. Two problems must be solved in terms of this theory: first, understanding the generation mechanism and nature of the waves that can heat the atmosphere, and, second, finding an efficient dissipation mechanism for these waves.

The generation of high-frequency (30–60 s) acoustic waves in the solar convection zone (the Lighthill mechanism), their transformation into shock waves, and, hence, the atmospheric heating have been studied adequately. However, as was shown by Mein *et al.* (1980), this mechanism can heat only the lower chromosphere.

Apart from the high-frequency acoustic waves mentioned above, a subphotospheric wave guide for acoustic waves (the so-called 5-min oscillations, i.e., *p*- and *f*-modes) is currently known to exist on the Sun. However, although Ulrich (1970) showed that the energy of the 5-min oscillations is high enough to heat the solar atmosphere, *p*-modes have not been considered as a possible source of nonradiative heating of the upper atmosphere for a long time. This is because the *p*-modes are trapped in subphotospheric layers, and no mechanism of effective energy transfer and dissipation of the *p*-modes in the upper solar atmosphere has been known until recently.

At present, the situation has changed significantly. A magnetic canopy, which, in the first approximation, may be considered as a layer with a horizontal magnetic field 5–10 G in strength, is now known to exist in the upper chromosphere and the transition region. In addition, studies of the propagation of MHD waves in an inhomogeneous magnetized plasma have led to the discovery of resonant wave absorption. The main feature of this highly efficient absorption mechanism is that the amount of wave energy absorbed at resonance levels depends neither on the dissipation mechanism (be it viscosity, Joule losses, or radiative heat exchange) nor on the dissipation coefficients

*E-mail: zhukov@SZ4792.spb.edu

1063-7737/04/3003-0194$26.00

(provided that they are small). Finally, the Alfvén and cusp resonance levels for p-modes turn out to be located in the region of the magnetic canopy.

Thus, taking into account the aforesaid, we inevitably come to the following heating scenario for the upper solar atmosphere: acoustic p-modes tunnel from subphotospheric layers to the resonance levels located in the magnetic canopy where they are absorbed, heating the upper chromosphere and the transition layer (Zhukov 1992, 1997a).

This scenario closely corresponds to the phenomenological scenario for the heating of the solar atmosphere by p-modes obtained by Libbrrecht (1988) by analyzing the line half-widths for p-modes. It should also be noted that, according to the estimates by Libbrrecht (1988), the upper atmosphere is heated only by p-modes with large ℓ. Our calculations indicate (Zhukov 2000, 2001) that only p-modes with large ℓ ($\ell > 300$) are effectively absorbed in the region of the magnetic canopy, which, in particular, justifies the use of a plane geometry in the calculated models.

In contrast to laboratory plasma, we cannot carry out an experiment on the Sun to test particular theoretical models. Therefore, it is important to find features of the phenomenon under study that could be observed directly. Since the frequencies of p-modes are measured with high accuracy, if the resonant absorption of p-modes in the magnetic canopy gave rise to any features in the p-mode spectrum, their observation could confirm the existence of resonant absorption. Such features have been found. Our calculations (Zhukov 2000, 2001) indicate that, given the resonant absorption, the p-mode spectrum has a fine structure that, in our view, was observed by Espagenet *et al.* (1996).

Thus, both the results obtained by Libbrrecht (1988) and the observations by Espagenet *et al.* (1996) are consistent with the idea of the resonant heating of the upper solar atmosphere.

Two approaches are currently used to calculate the spectrum of solar p-modes with allowance made for their resonant absorption in the region of the magnetic canopy. Previously (Zhukov 1997b, 2000, 2001) (see also Vanlommel *et al.* 2002), we calculated the spectrum in the approximation of an ideal medium by assuming that the oscillation eigenfrequencies were complex because of energy leakage from the resonator for acoustic waves (see Zhukov 1997a). Clearly, in this case, the singular points of the numerically integrable equations that correspond to resonances do not lie on the real axis. Tirry *et al.* (1998), Vanlommel and Goossens (1999), and Pintér and Goossens (1999) used a method that was developed to calculate the free oscillations of plasma structures similar to magnetic loops (Tirry and Goossens 1996) and that took into account the Joule losses in a thin resistive layer near the resonance level.

Here, we show that these two approaches must yield essentially identical results in calculations of the spectrum for p-modes with allowance made for their resonant absorption in the region of the magnetic canopy.

A TWO-LAYER MODEL

Let us consider the p-modes in a two-layer plane model that consists of an upper ($z > 0$) isothermal layer of finite conductivity with a uniform horizontal magnetic field $\mathbf{H_0}$ and a lower layer ($z < 0$) without a magnetic field in which the temperature linearly increases with depth (see Vanlommel *et al.* 2002). We restrict our analysis to the waves that propagate in the plane formed by the vectors of gravity $\mathbf{g}$ and magnetic field $\mathbf{H_0}$.

Since the solution of the equations that describe the wave propagation in the lower layer without a magnetic field is well known (see, e.g., Nye and Thomas 1976b; Evans and Roberts 1990; Vanlommel *et al.* 2002), to determine the spectrum of p-eigenmodes for this two-layer model, we only need to find a solution of the magnetohydrodynamic (MHD) equations that describes the wave propagation in an isothermal atmosphere of finite conductivity with a uniform horizontal magnetic field.

RESONANT ABSORPTION

Consider the absorption of waves at a cusp resonance level in an isothermal atmosphere of finite conductivity with a uniform horizontal magnetic field $\mathbf{H_0}$. From the basic system of MHD equations

$$\rho\frac{d\mathbf{v}}{dt} = -\mathrm{grad}p + \rho\mathbf{g} + \frac{1}{4\pi}\mathrm{curl}\mathbf{H}\times\mathbf{H}, \quad (1)$$

$$\frac{\partial\rho}{\partial t} + \mathrm{div}(\rho\mathbf{v}) = 0, \quad (2)$$

$$\frac{dp}{dt} = c^2\frac{d\rho}{dt} + \nu_\mathrm{m}\frac{\gamma-1}{4\pi}(\mathrm{curl}\mathbf{H})^2, \quad (3)$$

$$\frac{\partial\mathbf{H}}{\partial t} = \mathrm{curl}(\mathbf{v}\times\mathbf{H}) + \nu_\mathrm{m}\nabla^2\mathbf{H} \quad (4)$$

after linearization in a Cartesian coordinate system with the Z axis directed upward and the X axis directed along the magnetic field, we can derive the following differential equation for the vertical velocity v_Z:

$$f\frac{d^4v_Z}{d\xi^4} + 3\frac{df}{d\xi}\frac{d^3v_Z}{d\xi^3} + \left(3\frac{d^2f}{d\xi^2} - f - E\right)\frac{d^2v_Z}{d\xi^2} \quad (5)$$

$$+\left(\frac{d^3f}{d\xi^3}-\frac{df}{d\xi}-2\frac{dE}{d\xi}\right)\frac{dv_Z}{d\xi}-\left(E-\frac{d^2E}{d\xi^2}\right)v_Z$$
$$-\Lambda^2\left[\left(f-\Omega_X^2+\frac{\Omega_X^2}{\Omega_c^2}\right)\frac{d^2v_Z}{d\xi^2}+\frac{df}{d\xi}\frac{dv_Z}{d\xi}\right.$$
$$\left.-\left(E-\frac{\Omega_X^2}{\Omega_c^2}\left(\Omega_c^2-1\right)\right)v_Z\right]=0,$$

where we use the notation

$$\rho_0=\rho_0(0)f(\xi),\quad f(\xi)=e^{-\xi/K},$$
$$\xi=k_Xz,\quad K=k_XH,$$
$$\Lambda^2=iR_m,\quad R_m=\frac{\omega}{\nu_mk_X^2},$$
$$v_{A0}^2=\frac{H_0^2}{4\pi\rho_0(0)},\quad \Omega_X^2=\frac{v_{A0}^2k_X^2}{\omega^2},$$
$$\Omega_c^2=\frac{c^2k_X^2}{\omega^2},\quad G=\frac{gk_X}{\omega^2},$$
$$E=\left(1-\frac{1}{\Omega_c^2}\right)f+G\frac{df}{d\xi}+\frac{G^2}{\Omega_c^2}f.$$

Here, c is the speed of sound, $\mathbf{g}$ is the gravity vector, $H(=g\gamma/c^2)$ is the scale height, γ is the adiabatic index, ν_m is the magnetic viscosity, and R_m is the Reynolds magnetic number.

In deriving Eq. (5), we took a dependence of all the perturbed quantities on x and t in the form $\sim\exp i(k_Xx+\omega t)$; i.e., we restricted our analysis to the wave propagation in the plane formed by the vectors $\mathbf{H_0}$ and $\mathbf{g}$.

An Ideal Atmosphere

Let us first consider the wave propagation in an ideal atmosphere. In this case, since $\nu_m=0$, the basic equation takes the form

$$\left(f-\Omega_X^2+\frac{\Omega_X^2}{\Omega_c^2}\right)\frac{d^2v_Z}{d\xi^2}+\frac{df}{d\xi}\frac{dv_Z}{d\xi}-\left(E-\frac{\Omega_X^2}{\Omega_c^2}\left(\Omega_c^2-1\right)\right)v_Z=0. \quad (6)$$

It is easy to see that Eq. (6) has the regular singular point ξ_c at which the coefficient of the higher derivative in Eq. (6) becomes zero. This is the so-called point of cusp resonance ($\omega^2=\omega_T^2(\xi_c)$, here $\omega_T^2=c^2v_A^2k_X^2/(c^2+v_A^2)$, where $v_A^2=H_0/4\pi\rho_0$).

Clearly, the influence of a magnetic field in deep atmospheric layers may be disregarded, and we obtain a standard equation for the waves in an isothermal atmosphere without a magnetic field (Whittaker 1963). Its solutions are

$$v_Z=\left(C_1e^{ik_Zz}+C_2e^{-ik_Zz}\right)e^{z/2H}. \quad (7)$$

Here, $C_{1,2}$ are arbitrary constants, and

$$k_Z^2=-\frac{1}{4H^2}+\left(\frac{\omega^2}{c^2}-k_X^2\right)-\frac{gk_X^2}{\omega^2c^2}\left(g-\frac{c^2}{H}\right). \quad (8)$$

It follows from the dispersion relation (8) that acoustic waves with $\omega>\omega_a(=\gamma g/2c)$ and internal gravity waves with $\omega<\omega_g(=g\sqrt{\gamma-1}/c)$ can propagate in an isothermal atmosphere.

Brengauz (1970), Mekki *et al.* (1978), and Zhukov (1979) showed that internal gravity waves (to be more precise, magnetogravity waves) with frequencies below the second critical frequency ω_g could be absorbed in an isothermal atmosphere with a uniform horizontal magnetic field at a cusp resonance level. Therefore, we restrict our analysis below, to the case where an internal gravity wave is incident at a cusp resonance level.

As was shown by Nye and Thomas (1976a), changing the dependent and independent variables

$$w=v_Ze^{zK/H},\quad \eta=\frac{\Omega_c^2}{\Omega_X^2(\Omega_c^2-1)}e^{-z/H}$$

reduces Eq. (6) to

$$\eta(1-\eta)\frac{d^2w}{d\eta^2}+[C-(A+B+1)\eta]\frac{dw}{d\eta}-ABw=0. \quad (9)$$

Here,

$$A+B=C=2K+1, \quad (10)$$

$$AB=-\frac{1-\gamma}{\gamma^2}\Omega_c^2+K+\frac{K^2}{\Omega_c^2}. \quad (11)$$

Equation (9) is hypergeometric. Its general solution for $|\eta|<1$ is

$$w(\eta)=C_1F(A,B,C,\eta)+C_2F(A-C+1,B-C+1,2-C,\eta). \quad (12)$$

Here, F is the hypergeometric function, and $C_{1,2}$ are arbitrary constants.

In rarefied layers, the magnetogravity waves are nonpropagating. Since the second solution in (12) increases exponentially, it should be rejected as physically meaningless. Thus, for $|\eta|<1$, the solution of Eq. (12) is

$$w=C_0F(A,B,C,\eta). \quad (13)$$

Here, C_0 is an arbitrary constant that is assumed below to be equal to unity without loss of generality.

The singular point $\eta=1$ of Eq. (9) is the cusp resonance level (as was noted above, $\omega^2=\omega_T^2$ at this point).

To determine the behavior of the solution in deep atmospheric layers ($|\eta| > 1$), we use the following relation for the hypergeometric functions (Olver 1974):

$$F(A,B,C,\eta) = \frac{\Gamma(C)\Gamma(B-A)}{\Gamma(B)\Gamma(C-A)}(-\eta)^{-A} \times F\left(A,1+A-C,1+A-B,\eta^{-1}\right) + \frac{\Gamma(C)\Gamma(A-B)}{\Gamma(A)\Gamma(C-B)}(-\eta)^{-B} \times F\left(B,1+B-C,1+B-A,\eta^{-1}\right). \quad (14)$$

This relation is valid if the difference $A-B$ is not equal to an integer or zero and if $C \neq 0,-1,-2,\ldots$. Here, Γ is the Gamma function.

Thus, for $|\eta| > 1$, the solution of Eq. (6) is given by

$$v_Z(z) = e^{-zK/H}\left[\frac{\Gamma(A+B)\Gamma(B-A)}{\Gamma^2(B)}(-\eta)^{-A} \times F(A,1+B,1+A-B,\eta^{-1}) + \frac{\Gamma(A+B)\Gamma(A-B)}{\Gamma^2(A)}(-\eta)^{-B} \times F(B,1-A,1+B-A,\eta^{-1})\right]. \quad (15)$$

Since it follows from (10) and (11) that

$$A = \frac{1}{2} + K + ik_Z H, \text{ and}$$

$$B = \frac{1}{2} + K - ik_Z H,$$

solution (15) for $|\eta| \to \infty$ $(z \to -\infty)$ takes the form

$$v_Z \sim e^{z/2H}\left[\frac{\Gamma(A+B)\Gamma(B-A)}{\Gamma^2(B)}(-\beta)^{-A}e^{ik_Z z} + \frac{\Gamma(A+B)\Gamma(A-B)}{\Gamma^2(A)}(-\beta)^{-B}e^{-ik_Z z}\right], \quad (16)$$

$$\beta = \frac{\Omega_c^2}{\Omega_X^2(\Omega_c^2-1)},$$

i.e., transforms into (7). Consequently, for $\omega < \omega_g$, the first and second terms in (16) correspond to the incident and reflected internal gravity waves, respectively, and we obtain for the reflection coefficient

$$R_g = \frac{\Gamma(A-B)\Gamma^2(B)}{\Gamma(B-A)\Gamma^2(A)}(-\beta)^{A-B}. \quad (17)$$

Hence, using the standard properties of the Gamma function and taking into account the fact that $\omega < \omega_g < ck_X$ and, therefore, $\beta > 0$, we obtain for a low-frequency magnetogravity wave

$$|R_g| = e^{-2\pi k_Z H} < 1. \quad (18)$$

Thus, we see from (18) that the wave energy is partially lost in an isothermal atmosphere with a uniform horizontal magnetic field, and, therefore, an amount of energy equal to

$$\Delta = 1 - |R_g|^2$$

is absorbed near the cusp resonance level. However, there is no dissipation in an ideal medium, and, hence, no absorption of wave energy is actually possible.

In deriving (17), we took a time dependence in the form $\exp(i\omega t)$. In fact, this implies that the process began at $t = -\infty$, and all the transient phenomena have finished by the present time. Clearly, the solution of the problem with initial data when the process begins at $t = t_0$ is more suitable for analyzing the resonant absorption of waves in an ideal medium. As we showed previously (Zhukov 1979), in this case, the vertical velocity v_Z in an isothermal atmosphere with a uniform horizontal magnetic field at a resonance level infinitely increases with time,

$$v_Z \sim e^{i\omega t}\ln t, \quad t \to +\infty.$$

Therefore, the energy lost at the resonance level is the energy that goes into the excitation of oscillations at the resonance level.

Finite Conductivity

Let us now consider the propagation of waves in an isothermal atmosphere of finite conductivity with a uniform horizontal magnetic field $\mathbf{H_0}$. The conductivity is assumed to be high, i.e., $|\Lambda^2| \gg 1$. A solution of Eq. (5) may then be sought in the form of a series

$$v_Z = \left(v_0 + \Lambda^{-1}v_1 + \cdots\right)\exp\left[\Lambda\int^{\xi}\lambda(\xi)d\xi\right]. \quad (19)$$

Substituting series (19) into Eq. (5) and equating the terms of the same order in Λ yields

$$\lambda_{1,2}^2 = 0, \quad (20)$$

$$\lambda_{3,4}^2 = f^{-1}\left(f - \Omega_X^2 + \frac{\Omega_X^2}{\Omega_c^2}\right). \quad (21)$$

It is easy to show that v_0 for $\lambda = \lambda_{1,2}$ is a solution of the shortened equation (6) that describes the wave propagation in an ideal atmosphere and that was analyzed in detail in the previous section.

For the second pair of characteristic roots $\lambda = \lambda_{3,4}$, we obtain

$$v_0 = \left[\lambda f\left(f - \Omega_X^2 + \frac{\Omega_X^2}{\Omega_c^2}\right)\right]^{-1/2}. \quad (22)$$

The small-scale solutions (21) and (22) of Eq. (5) are exponentially small outside the resistive layer—a thin layer near the cusp resonance level ξ_c; therefore, only the large-scale waves described by Eq. (6) can propagate outside the resistive layer. Since here we are primarily interested in resonant absorption, below we restrict our analysis only to low-frequency ($\omega < \omega_g$) waves.

The point of cusp resonance ξ_c is the regular singular point of the differential equation (6). The asymptotics of solutions (21) and (22) are also invalid near this point. Clearly, the full fourth-order equation (5) should be used in the resistive layer. However, it can be simplified significantly in a thin resistive layer and reduced to a fourth-order equation that can be solved by the Laplace method.

Indeed, since near the resonance

$$f(\xi) = f(\xi_c) + \alpha(\xi - \xi_c) + \cdots, \quad \alpha = -\frac{f(\xi_c)}{K},$$

introducing a scaled variable $Y = \Lambda^{2/3}(\xi_c - \xi)$ and disregarding the small terms, we reduce Eq. (5) to

$$\frac{d^4 v_Z}{dY^4} - \frac{1}{K}\frac{d}{dY}\left(Y\frac{dv_Z}{dY}\right) = 0. \qquad (23)$$

The asymptotics of the solutions for this equation that we need below are

$$v_Z \sim -\ln(-X) - i\pi, \qquad \xi > \xi_c, \qquad (24)$$

$$v_Z \sim -\ln(X) - \frac{\pi^{1/2}}{X^{3/4}} e^{-\frac{2}{3}Y^{3/2}}, \quad \xi < \xi_c,$$

where we denoted $X = K^{-1/3}Y$.

Now, matching asymptotics (24) with the asymptotics of the solutions for (20) and (21), we finally obtain

$$v_Z = e^{-zK/H} F(A, B, C, \eta), \quad \xi > \xi_c, \qquad (25)$$

$$v_Z(z) = e^{-zK/H}\left[\frac{\Gamma(A+B)\Gamma(B-A)}{\Gamma^2(B)}(-\eta)^{-A}\right. \qquad (26)$$

$$\times F(A, 1+B, 1+A-B, \eta^{-1})$$

$$+ \frac{\Gamma(A+B)\Gamma(A-B)}{\Gamma^2(A)}(-\eta)^{-B}$$

$$\left.\times F(B, 1-A, 1+B-A, \eta^{-1})\right] + \frac{\Gamma(A+B)}{\Gamma(A)\Gamma(B)}$$

$$\times \frac{\left(\frac{\pi}{k_X H \Lambda}\right)^{1/2}\left(\Omega_X^2 - \frac{\Omega_X^2}{\Omega_c^2}\right)}{\left[\lambda f\left(f - \Omega_X^2 + \frac{\Omega_X^2}{\Omega_c^2}\right)\right]} \exp\left[\Lambda \int_{\xi_c}^{\xi} \lambda(\xi) d\xi\right],$$

$$\xi < \xi_c.$$

Here, for λ, we choose the root of Eq. (21) for which the small-scale solution (the third term in (26)) exponentially decays for $\xi < \xi_c$.

A comparison of Eqs. (26) and (15) indicates that a large-scale magnetogravity wave linearly transforms into a small-scale wave mode (described by the third term in (26)) in an isothermal atmosphere of finite conductivity near the cusp resonance. This mode effectively dissipates in a thin resistive layer $\delta \sim |\Lambda|^{-2/3}$ in the thickness near the resonance level ξ_c.

Thus, it follows from our results that the approximation of an ideal medium can be used to calculate the wave absorption efficiency at the cusp resonance. Moreover, although this conclusion was drawn from an analysis of the wave propagation only in an isothermal atmosphere, it is clearly valid for any atmosphere. This is because, as follows from Eq. (23), a large-scale wave mode linearly transforms into a small-scale mode near the cusp resonance, and Eq. (23) is itself determined only by the atmospheric parameters near the resonance level. A similar result is also obtained for the absorption at the Alfvén resonance level (see, e.g., Zhukov 1988, 1990).

THE DISPERSION RELATION

Now, knowing the solution for the upper and lower layers and taking into account the fact that the total pressure and the vertical velocity must be continuous at the interface ($z = 0$), we can easily derive a dispersion relation that defines the spectrum of p-modes in the two-layer system under consideration.

It is clear from the above results that for the eigenfrequencies of the p-modes for which the cusp resonance levels are located at $z > \delta$ (for such p-modes at $z = 0$, the third term in Eq. (26) may be disregarded, i.e., basically, the solution at $z = 0$ can be expressed in terms of hypergeometric functions for these modes), we obtain a dispersion relation that closely matches the dispersion relation derived by Vanlommel *et al.* (2002), who used the approximation of an ideal medium.

DISCUSSION AND CONCLUSIONS

In previous sections, we have considered the influence of a finite conductivity on the spectrum of p-modes in a two-layer model that consists of an upper isothermal layer with a uniform horizontal magnetic field and a lower layer without a magnetic field.

Previously (Zhukov 1997b, 2000, 2001), in our numerical calculations of the spectrum of p-modes with an allowance made for their resonant absorption in the magnetic canopy, we used a more realistic model of the solar atmosphere for the upper

layer. In addition, we took into account the resonant absorption of waves not only at cusp resonances, but also at Alfvén resonances. However, since (as was noted in the section titled "Finite conductivity") a large-scale wave mode linearly transforms into a small-scale mode at cusp and Alfvén resonance levels that effectively dissipates in a thin resistive layer; the dispersion relation in this case is determined by the large-scale wave modes that are the solutions of the ideal MHD equations.

Thus, in calculating the p-mode spectrum based on the above reasoning and when taking into account the fact that the resonance levels in the calculated models are located far from the $z = 0$ interface, we may restrict our analysis to calculating the spectrum in the approximation of ideal magnetohydrodynamics by assuming, of course, that the p-mode frequencies are complex.

In all the works known to us, when the spectrum of solar p-modes was calculated, the magnetic field in the atmosphere was assumed to be purely horizontal. In reality, the canopy magnetic field has a complex three-dimensional structure. The peculiar features of the resonant absorption of p-modes in models with such a complex field geometry have not yet been studied. However, evidence suggests that resonant absorption also takes place in such complex systems (see, e.g., Goossens 1995). Therefore, the conclusion that the approximation of an ideal medium can be used to study the resonant absorption of p-modes in models of the solar atmosphere is of particular importance, because it significantly simplifies the problem.

In conclusion, note that an allowance made for radiative heat exchange (with the Newton heat exchange law) does not increase the order of the equation that describes the resonant absorption, as is the case, for example, with finite conductivity, but just shifts the singular point of the equation corresponding to the resonance from the real axis to the complex plane (Zhukov 1989).

ACKNOWLEDGMENTS

This work was supported by the Nonstationary Phenomena in Astronomy program of the Presidium of the Russian Academy of Sciences and the Astronomy Federal Science and Technology Program. I wish to thank the referee for its valuable advice and remarks, which significantly improved the paper.

REFERENCES

1. V. D. Brengauz, Izv. Akad. Nauk SSSR, Ser. Mekh. Zhidk. Gaza **1**, 3 (1970).
2. W. R. Campbell and B. Roberts, Astrophys. J. **338**, 538 (1989).
3. O. Espagenet, R. Muller, Th. Roudier, *et al.*, Astron. Astrophys. **313**, 297 (1996).
4. J. E. Evans and B. Roberts, Astrophys. J. **356**, 704 (1990).
5. M. Goossens, *An Introduction to Plasma Astrophysics and Magnetohydrodynamics* (Kluwer Acad., Boston, 1995; Mir, Moscow, 2003).
6. R. Jain and B. Roberts, Astron. Astrophys. **286**, 243 (1994a).
7. R. Jain and B. Roberts, Astron. Astrophys. **286**, 254 (1994b).
8. K. G. Libbrrecht, Astrophys. J. **334**, 510 (1988).
9. P. Mein, N. Mein, and B. Schmieder, in *Proceedings of Japan-France Seminar on Solar Physics, 1980*, Ed. by F. Moriyama and C. Heènoux, p. 70.
10. O. El Mekki, I. A. Eltayeb, and J. F. McKenzie, Solar Phys. **57**, 261 (1978).
11. A. H. Nye and J. H. Thomas, Astrophys. J. **204**, 573 (1976a).
12. A. H. Nye and J. H. Thomas, Astrophys. J. **204**, 582 (1976b).
13. F. W. J. Olver, *Asymptotics and Special Functions* (Academic, New York, 1974; Nauka, Moscow, 1978, 1990).
14. B. Pintér and M. Goossens, Astron. Astrophys. **347**, 321 (1999).
15. M. Schwarzchild, Astrophys. J. **107**, 1 (1948).
16. W. J. Tirry and M. Goossens, Astrophys. J. **471**, 501 (1996).
17. W. J. Tirry, M. Goossens, B. Pintér, *et al.*, Astrophys. J. **503**, 422 (1998).
18. R. K. Ulrich, Astrophys. J. **162**, 993 (1970).
19. P. Vanlommel and M. Goossens, Solar Phys. **187**, 357 (1999).
20. P. Vanlommel, A. Debosscher, J. Andries, and M. Goossens, Solar Phys. **205**, 1 (2002).
21. W. A. Whittaker, Astrophys. J. **137**, 914 (1963).
22. V. I. Zhukov, Soln. Dannye **7**, 75 (1979).
23. V. I. Zhukov, Fiz. Plazmy **14**, 871 (1988).
24. V. I. Zhukov, Astron. Astrophys. **222**, 293 (1989).
25. V. I. Zhukov, Astrophys. Space Sci. **174**, 173 (1990).
26. V. I. Zhukov, Solar Phys. **139**, 201 (1992).
27. V. I. Zhukov, Solar Phys. **173**, 15 (1997a).
28. V. I. Zhukov, Astron. Astrophys. **322**, 302 (1997b).
29. V. I. Zhukov, Astron. Astrophys. **354**, 277 (2000).
30. V. I. Zhukov, Astron. Astrophys. **369**, 672 (2001).

Translated by V. Astakhov

Astronomy Letters, Vol. 30, No. 3, 2004, pp. 200–208. Translated from Pis'ma v Astronomicheskiĭ Zhurnal, Vol. 30, No. 3, 2004, pp. 231–240.

A Wide-Field Corrector at the Prime Focus of a Ritchey–Chrétien Telescope

V. Yu. Terebizh*

Sternberg Astronomical Institute, Universitetskiĭ pr. 13, Moscow, 119992 Russia

Received July 16, 2003

Abstract—We propose a form of a lens corrector at the prime focus of a hyperboloidal mirror that provides a flat field of view up to 3° in diameter at image quality $D_{80} < 0.8$ arcsec in integrated (0.32–1.1 μm) light. The corrector consists of five lenses made of fused silica. All lens surfaces are spherical in shape, so the system is capable of achieving better images, if necessary, by aspherizing the surfaces. The optical system of the corrector is stable in the sense that its principal features are retained when optimized after significant perturbations of its parameters. As an example, we calculated three versions of the corrector for the Blanco 4-m telescope at Cerro Tololo Inter-American Observatory with 2?12, 2?4, and 3?0 fields of view. © *2004 MAIK "Nauka/Interperiodica"*.

Key words: *astronomical observing techniques, devices and instruments.*

INTRODUCTION

The advent of reflectors with aperture diameters of 8–10 m required a revision of observational programs for telescopes of preceding generations. Emphasis was placed on designing systems of adaptive optics and conducting sky surveys at the prime focus with a mounted wide-angle field corrector. The choice of the second direction is determined by several factors.

First, several observational programs aimed at solving important astrophysical problems, in particular, at studying gamma-ray bursts, searching for hidden mass, and analyzing gravitational lensing in clusters of galaxies, are of current interest. For obvious reasons, the diameter of Schmidt telescopes are difficult to increase to values well above the current level of ~1.3 m. Special 4-m telescopes with lens correctors whose curves are calculated along with those of the primary mirror are being designed to solve these problems: the Next Generation Lowell Telescope (NGLT) (Blanco *et al.* 2002) and the Visible and Infrared Survey Telescope for Astronomy (VISTA) (McPherson *et al.* 2002; Emerson and Sutherland 2002). Particular attention is given to the Large Synoptic Survey Telescope (LSST) with an effective aperture of about 6.5 m at a primary mirror diameter of 8.4 m (Angel *et al.* 2000; Tyson 2002; Seppala 2002). At the same time, when equipped with correctors at the prime focus with a field of view of ~1?5–2?0 in diameter, the existing 4-m Ritchey–Chrétien telescopes achieve an efficiency comparable to the efficiency for the telescopes being designed.

In addition, the fact that a field corrector to an existing telescope can be made relatively quickly also seems important.

Finally, at a diameter of ~4 m and a focal ratio of ~2.5–3, the primary mirror of a Ritchey–Chrétien telescope with a roughly afocal field corrector can be matched in modulation transfer function with the main modern CCD detectors with pixel sizes of ~15 μm. Thus, a challenging problem during observations at the Cassegrain focus is solved in a natural way.

Much effort has been made to design field correctors at the prime focus of a reflector (see the reviews by Wynne 1972; Mikhelson 1976, Sect. 7.5; Wilson 1996, Sect. 4.3; Schroeder 2000, Sect. 9.2). The correctors designed by Ross (1935) and Wynne (1968) were the systems that determined the development of this area of research for a very long time. The former corrector has a flat field of view $2w \simeq 15'$ in diameter with stellar images better than $1''$; the latter detector has an about $50'$ field of view of similar quality. Many of the modern reflectors are equipped with three-lens Wynne correctors or similar modifications of this system. The observational programs being planned require a field of view no less than 1?5 in diameter. Thus, for example, the NGLT and VISTA projects mentioned above are to provide a flat field of view $2w = 2°$ in diameter. The correctors calculated for these telescopes have four or five aspherical lenses, with the diameter of the front lens reaching 1.25 m. The front lens of the LSST corrector is 1.34 m in diameter; the concave surfaces of the lenses are eighth-order aspherics.

*E-mail: terebizh@crao.crimea.ua

1063-7737/04/3003-0200$26.00

Here, we suggest a new type of corrector at the prime focus of a hyperboloidal mirror (Fig. 1) that provides a flat field of view up to 3° in diameter at image quality better than 0″.8 (we have in mind D_{80}—the diameter of the image of a point source within which 80% of energy is enclosed) in integrated (0.32–1.1 μm) light. Since observations are generally carried out in relatively narrow spectral ranges rather than in integrated light, the corresponding image size with the corrector is smaller than this value. All lens surfaces are spherical in shape, so the system is not only relatively easy to make, but also is capable of achieving better images by aspherizing the surfaces. All lenses are made of fused silica. This material has good manufacturing properties and provides high transparency in the ultraviolet, which is often of key importance.

The suggested corrector system is designed for a hyperboloidal mirror with a conical constant typical of Ritchey–Chrétien telescopes. As specific examples, we discuss three versions of the corrector for the Blanco 4-m telescope at Cerro Tololo Inter-American Observatory—systems "R", "S", and "T" with 2°.12, 2°.4, and 3°.0 fields of view, respectively (Table 1). The last two systems should be considered to be basic, while in system "R" designed for a reduced diameter of the front lens, we had to introduce noticeable distortions.

THE PRIMARY MIRROR OF THE TELESCOPE

The parameters of the primary mirror of the Blanco telescope (Table 2) were taken from the report by Gregory and Boccas (2000). The central obscuration is produced by a hole in the mirror and stray-light baffles. Since images far from the diffraction limit are dealt with in wide-field observations, the central obscuration affects the images only slightly.

Note that the corrector systems described below need to be adjusted only slightly for a moderate change in the parameters of the primary mirror given in Table 2. In particular, this is true for a paraboloidal primary mirror.

SYSTEM "S"

The optical layout of corrector "S" is shown in Fig. 1 (for detailed information, see Table 3). The letters FS denote fused silica. The most commonly used Schott BK7 glass was taken as the material for the filter; clearly, the system is not critical in this regard, and choosing a different glass as well as adopting a different thickness of the filter can be easily compensated for.

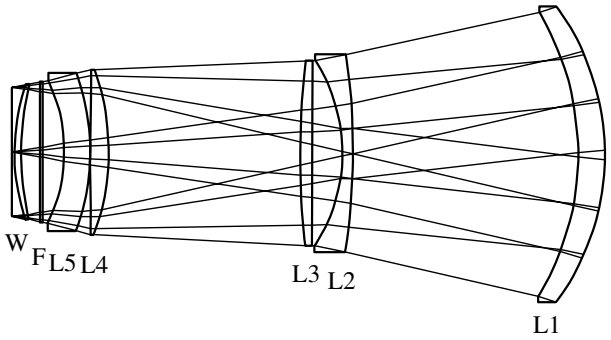

Fig. 1. Optical layout of corrector "S". The last elements are the filter (F) and detector window (W).

If we remove lenses L3 and L5 from system "S", the remaining part resembles the classical system by Wynne (1968). The necessity of introducing these two lenses to produce a really large field of view stems from the fact that, in this case, doublets L2+L3 and L4+L5 are formed; each of these effectively suppresses the aberrations of the primary mirror and primarily coma. Interestingly, lens L3 has already appeared in the corrector designed by Delabre (2002) for a $2w = 0°.95$ field of view. Delabre's system consists of three lenses and a detector window with optical power.

Optical power is also planned to be imparted to the detector window in the correctors described here. A slightly worse, but comparable image quality is achieved for a flat window. However, it seems natural to use additional degrees of freedom, given the total number of optical surfaces.

The five-lens system shown in Fig. 1 is *stable* in the sense that its principal features are retained when optimized after significant perturbations of its parameters. The final state in stable systems is reached abruptly; i.e., either a global or a nearly global minimum of the merit function is realized in the multidimensional space of optical parameters. The numerous variations of a three-lens corrector show that a similar stability is also characteristic of Wynne's triplet, but in lower-dimensional space. These features of the five-lens system allow it to be considered as a new type of field corrector at the prime focus of a reflector.

Figure 2 shows spot diagrams[1] for system "S" in integrated light. A slightly clearer idea of the image quality can be got from the plot of the fraction of enclosed energy in the diffraction stellar image shown in Fig. 3. We took special measures in order that the diameters of the stellar images remain constant over

[1] The distribution of light rays in a stellar image on the focal plane.

Table 1. General parameters of the correctors

Parameter	Corrector		
	"R"	"S"	"T"
Angular field of view, $2w$, deg	2.12	2.4	3.0
Effective focal length with telescope, mm	11506.7	11400.4	11505.9
Focal ratio	2.92	2.90	2.92
Scale, μm arcsec^{-1}	55.79	55.27	55.78
Linear field of view, mm	427	481	606
Spectral range, μm	0.32–1.10	0.32–1.10	0.32–1.10
Change of image RMS radius over field, 0.32–1.10 μm	13.2–15.6 μm 0.″24–0.″28	12.4–15.6 μm 0.″22–0.″28	14.3–19.8 μm 0.″26–0.″35
Change of D_{80} over field (center—edge, 0.32–1.10 μm)	33.2–38.5 μm 0.″60–0.″70	31.8–38.0 μm 0.″58–0.″68	36.0–45.0 μm 0.″64–0.″80
Change of D_{80} over field in 0.35–0.45-μm band	20.0–39.3 μm 0.″36–0.″70	17.4–40.2 μm 0.″32–0.″72	19.6–52.8 μm 0.″36–0.″94
Change of D_{80} over field in 0.54–0.66-μm band	24.4–30.3 μm 0.″44–0.″54	20.2–25.8 μm 0.″37–0.″47	24.0–28.2 μm 0.″44–0.″50
Change of D_{80} over field in 0.70–0.90-μm band	25.8–38.3 μm 0.″46–0.″69	20.4–33.8 μm 0.″37–0.″61	25.4–38.8 μm 0.″46–0.″70
Transmittance (including reflections, without coatings, 0.32–1.10 μm)	0.53–0.55	0.53–0.55	0.53–0.55
Maximum distortion, %	0.42	0.60	0.61
Maximum distortion gradient with wavelength, μm^{-1}	3.88×10^{-4}	2.25×10^{-4}	3.25×10^{-4}
Types of lens surfaces	All spheres	All spheres	All spheres
Maximum clear aperture, mm	900	1100	1300

the entire field. As we see from Fig. 3, D_{80} changes from 0.″58 on the optical axis to 0.″68 at the edge of the field of view. The image quality in narrow spectral bands is given in Table 1. Note that the refocusing range when passing from one spectral band to another is only a few hundredths of a millimeter; such a small value is attributable to the optimization of the system in integrated light.

Table 2. Primary mirror

Parameter	Value
Radius of curvature at vertex	−21 311.6 mm
Conic constant k	−1.09763
Aperture diameter	3934 mm
Central screening	1651 mm

The corrector is close to an afocal system, so the focal length of the telescope exceeds the focal length of the primary mirror only slightly (see Tables 1 and 2). At a pixel size of ~15 μm characteristic of the CCD detectors currently used in astronomy, an angle of 0.″27 corresponds to one pixel in the focal plane. Accordingly, approximately 1.5 to 2.5 pixels fit into the diameter D_{80}, depending on the width of the spectral range used in observations. This matching of the optical system with the detector should be considered as satisfactory.

Since the lenses of the corrector are made of fused silica, its transmittance depends weakly on wavelength in the spectral range 0.32–1.10 μm considered here (the data of Table 1 refer to lenses L1–L5). The deposition of effective modern coatings will provide a

Table 3. Parameters of the "S" optical system

Surface number	Comments	Radius of curvature, mm	Thickness, mm	Glass	Clear aperture, mm
1	Aperture stop	∞	90.755	–	3934.00
2	Primary mirror ($k = -1.09763$)	−21311.6	−8521.90	Mirror	3934.00
3	L1	−921.47	−100.00	FS	1100.00
4		−1017.83	−855.28	–	1056.78
5	L2	−2321.62	−40.00	FS	740.03
6		−620.63	−116.04	–	693.91
7	L3	∞	−45.00	FS	693.96
8		3077.69	−730.57	–	694.04
9	L4	−872.53	−70.13	FS	619.93
10		33728.22	−1.00	–	616.39
11	L5	−865.49	−98.20	FS	591.30
12		−620.76	−80.19	–	533.31
13	Filter	∞	−12.00	BK7	526.08
14		∞	−71.36	–	523.30
15	Window	1047.66	−25.00	FS	508.85
16		734.15	−10.00	–	508.06
17	Detector	∞			480.55

~83% transmittance of the corrector. Thus, adding two fused silica lenses to Wynne's corrector, which affects the system transparency only slightly, allows us to significantly expand the field of view with good images.

For linear fields of view on the order of half a meter of interest, not so much the image distortion as its variation with wavelength is hazardous (Ingerson 1997). In system "S", the positive[2] distortion reaches its maximum at the edge of the field of view in the ultraviolet; the exact value is 0.606% for a field angle of $w = 1°.2$ and a wavelength of 0.32 μm. If we are not faced with a special astrometric problem, then this value may be considered negligible. Otherwise, remaining constant over time, the distortion can be taken into account when processing the data.

In our case, the variation of the distortion with wavelength is shown in Fig. 4. The maximum (in absolute value) distortion gradient is -2.25×10^{-4} μm^{-1}. Suppose, for example, that the observations are carried out in a 0.1-μm-wide ultraviolet band. The length of the spectrum attributable to the distortion variation with wavelength is then 5.4 μm (the radius of the field of view was taken to be 240 mm). This length is only a small fraction of the total image size $D_{80} \simeq 40$ μm at the edge of the field in the ultraviolet. Since the effect under discussion plays an appreciably lesser role in other spectral ranges, the distortion in system "S" may be considered acceptable.

[2] Often called pincushion.

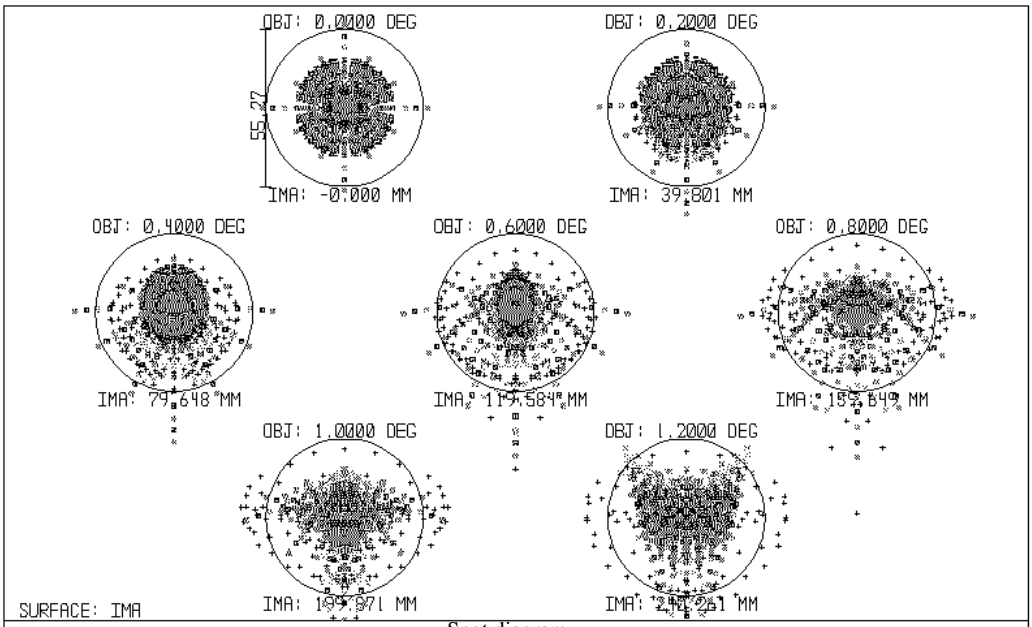

Spot diagram

Units are microns.

Field:	1	2	3	4	5	6	7
RMS radius:	12.432	12.260	12.137	12.647	13.401	13.642	15.568
GEO radius:	29.027	37.245	45.165	55.033	70.617	85.000	97.833
Circle diam:	55.27			Reference : Centroid			

Fig. 2. Spot diagrams for corrector "S" in the spectral range 0.32–1.10 μm for field angles of 0°, 0°.2, 0°.4, 0°.6, 0°.8, 1°.0, and 1°.2. The circle diameters corresponds to 1 arcsec (55.27 μm). The root-mean-square (RMS) and geometrical (GEO) radii of the images of a point source (in micrometers) are indicated for each of the seven field angles.

SYSTEM "T"

The optical layout of corrector "T" is shown in Fig. 5; its parameters are given in Table 4.

In this case, the image quality (Fig. 6) is only slightly worse than that for system "S". As above, an angle of $0''.27$ corresponds to a 15-μm detector pixel in the focal plane. Therefore, the above remarks concerning the matching of the optical system and the light detector remain valid.

The fact that the basic optical system remained virtually unchanged when the field of view increased significantly, from 2°.4 to 3°.0, suggests that it is suited primarily for *wide-field* observations. In fact, the introduction of two doublets effectively suppressing the coma supports this aim. We can also calculate a four-lens corrector with an image quality that is only slightly worse than that for the corrector in the five-lens system "S", but we failed to find a four-lens "double" of system "T" for a 3° field.

The refocusing range of the corrector when changing the spectral band does not exceed 0.05 mm.

The transparency of the system under consideration in the entire spectral range 0.32–1.10 μm is virtually the same as that for system "S".

The type of image distortion (positive) was also preserved. At the edge of the field of view, the distortion slightly increases from 0.607% in the ultraviolet to 0.611% in the infrared. The distortion in both correctors is small; if necessary, an orthoscopic corrector can be calculated rigorously. The largest distortion gradient with wavelength, more specifically, 3.25×10^{-4} μm^{-1}, is reached at the edge of the field again for $\lambda = 0.32$ μm. During observations in a 0.1-μm-wide ultraviolet band, the distortion variation with wavelength causes the images to blur at the edge of the field by slightly less than 10 μm. This value is almost twice as large as the value for system "S". However, as above, it is small compared to the sizes of the images themselves.

SYSTEM "R"

In the Introduction, we noted that decreasing the diameter of the front lens in system "R" entails a noticeable distortion of the basis system. For this reason, system "R" is given here as a supplement to the correctors considered above. Nevertheless, system "R", taken individually, is of interest in realizing

Table 4. Parameters of the optical system "T"

Surface number	Comments	Radius of curvature, mm	Thickness, mm	Glass	Clear aperture, mm
1	Aperture stop	∞	90.755	–	3934.00
2	Primary mirror ($k = -1.09763$)	−21311.6	−8150.16	Mirror	3934.00
3	L1	−1084.73	−110.00	FS	1300.00
4		−1226.17	−975.325	–	1256.42
5	L2	−2754.95	−40.00	FS	895.21
6		−742.97	−150.24	–	841.71
7	L3	9276.47	−45.00	FS	841.83
8		3011.10	−910.86	–	842.74
9	L4	−866.96	−96.00	FS	772.69
10		−14737.23	−1.00	–	769.07
11	L5	−792.85	−71.00	FS	726.26
12		−602.28	−121.60	–	669.50
13	Filter	∞	−12.00	BK7	661.82
14		∞	−81.44	–	658.87
15	Window	1269.90	−30.00	FS	643.51
16		901.66	−10.00	–	642.55
17	Detector	∞			606.38

Table 5. Parameters of the optical system "R"

Surface number	Comments	Radius of curvature, mm	Thickness, mm	Glass	Clear aperture, mm
1	Aperture stop	∞	90.755	–	3934.00
2	Primary mirror ($k = -1.09763$)	−21311.6	−9011.089	Mirror	3934.00
3	L1	−705.30	−81.34	FS	900.00
4		−823.90	−497.65	–	869.64
5	L2	−1483.06	−35.16	FS	670.60
6		−506.93	−304.37	–	621.38
7	L3	14674.93	−42.38	FS	614.17
8		1829.42	−472.97	–	613.92
9	L4	−385.00	−35.00	FS	512.86
10		−382.33	−51.69	–	494.85
11	L5	−745.23	−62.00	FS	494.24
12		−1168.35	−44.72	–	478.18
13	Filter	∞	−12.00	BK7	471.52
14		∞	−70.04	–	468.96
15	Window	878.97	−25.22	FS	455.64
16		596.19	−10.00	–	455.21
17	Detector	∞			427.71

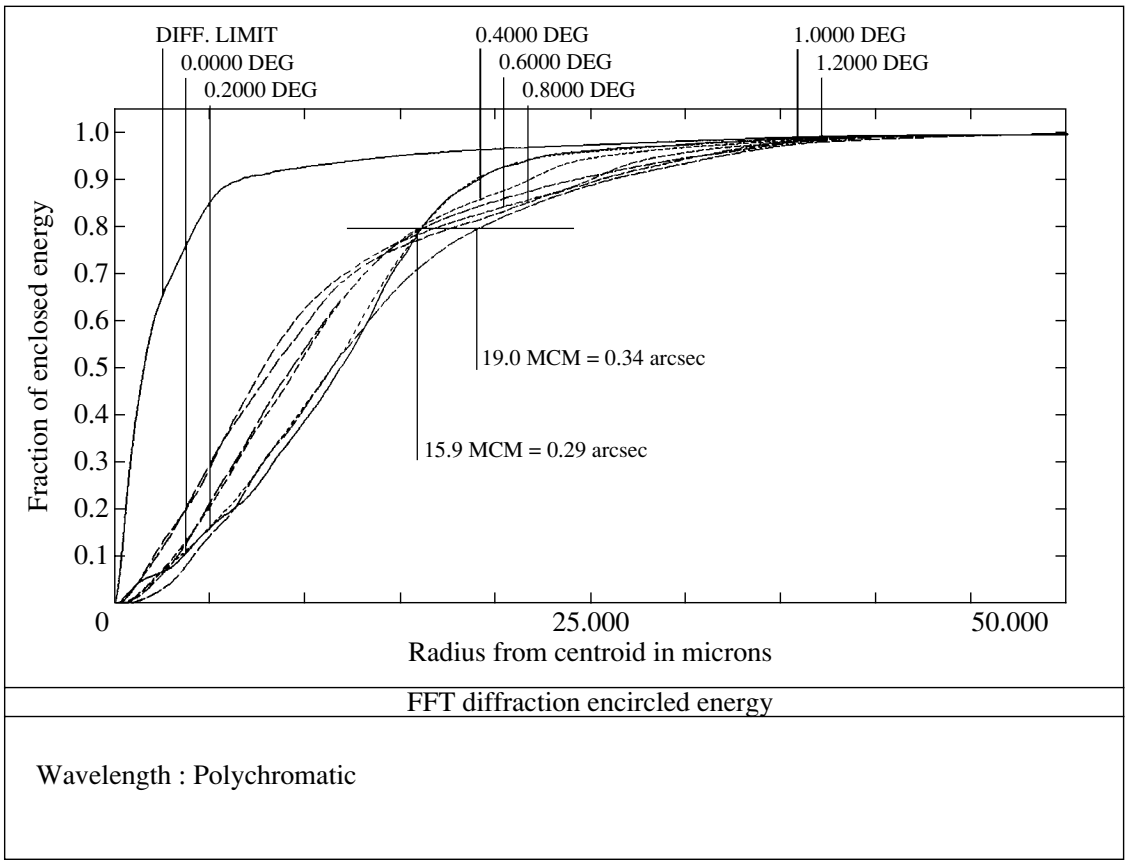

Fig. 3. Integral energy distribution along the radius in the diffraction stellar image for corrector "S" in the spectral range 0.32–1.10 μm for field angles of 0°, 0°.2, 0°.4, 0°.6, 0°.8, 1°.0, and 1°.2. The 80% level and the corresponding extreme values of the radius (in micrometers and arcseconds) are indicated.

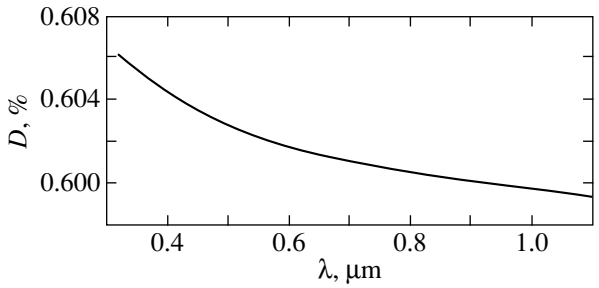

Fig. 4. Relative image distortion versus wavelength at the edge of the field of view of system "S".

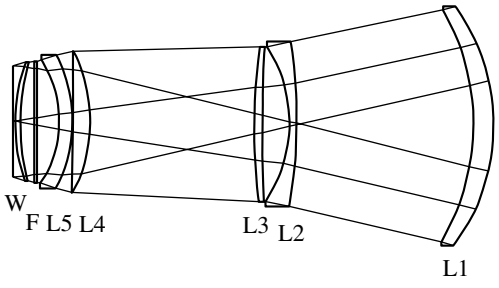

Fig. 5. Optical layout of corrector "T". The last elements are the filter (F) and detector window (W).

a field of view slightly larger than 2° (the adopted specific field diameter of 2°.12 corresponds to the diagonal of a square with a 1°.5 side).

Table 1 gives a description of system "R" enough to get an idea of the image quality. Table 5 lists parameters of the optical elements; further information can be obtained after inputting the data of Table 5 in an optical program.

As we see from Table 1, the relatively compact system "R" provides roughly the same image quality as does system "S", but within a slightly smaller field of view.

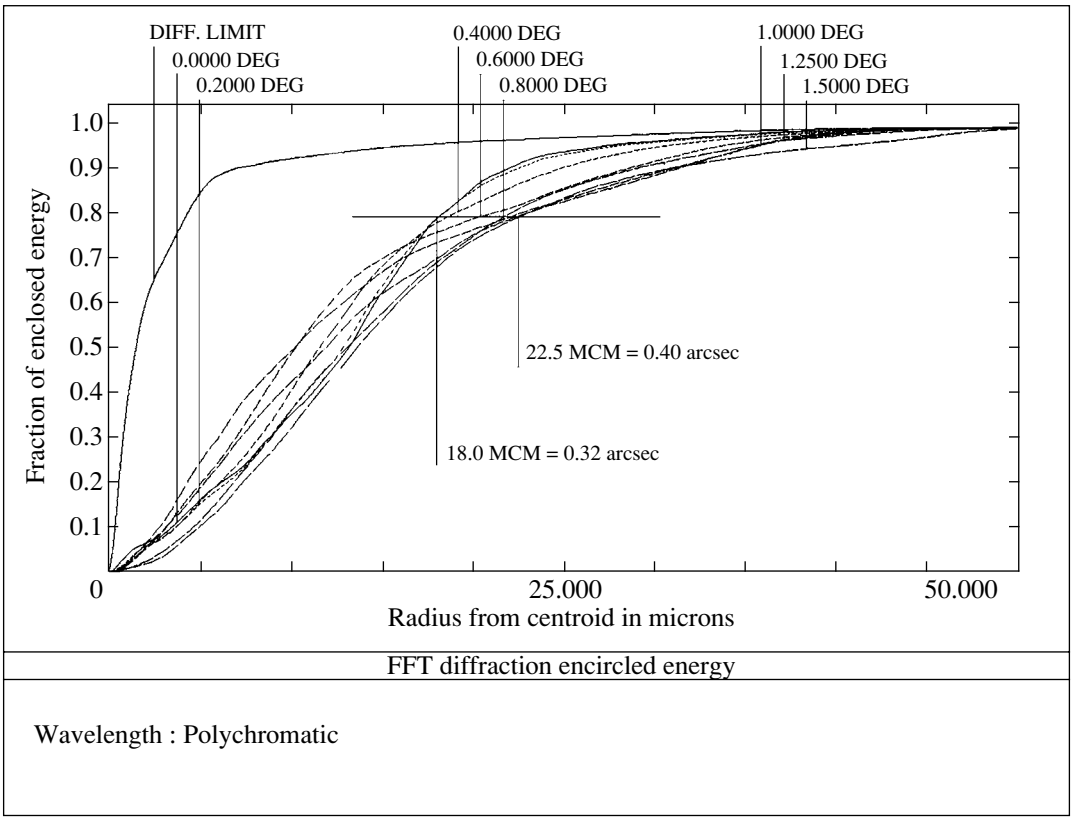

Fig. 6. Integral energy distribution along the radius in the diffraction stellar image for corrector "T" in the spectral range 0.32–1.10 μm for field angles of 0°, 0°.2, 0°.4, 0°.6, 0°.8, 1°.0, 1°.25, and 1°.5. The 80% level and the corresponding extreme values of the radius (in micrometers and arcseconds) are indicated.

CONCLUDING REMARKS

The field correctors considered here are relatively simple systems: the lens surfaces are spherical in shape, and the lenses themselves are made of the same material. The question as to whether to aspherize some or all of the surfaces should probably be solved depending on specific circumstances that include the need for achieving better images, the corrector production cost, etc.

As in systems of adaptive optics, the requirement of providing high transparency of the system in the ultraviolet range 0.32–0.34 μm presents the greatest difficulty in using the lenses (see, in particular, Tokovinin *et al.* 2003). Since the total thickness of the corrector lenses is large, this requirement, in fact, narrows down the choice to one material—fused silica. Quartz optics are known to be transparent far beyond the range 0.32–1.10 μm considered here. Computationally, it becomes possible to use a single material in such a complex optical system as the field corrector, because a moderate change in the focal length of the telescope is admissible.

Apart from high transparency, there are also other reasons for seeking to make the system purely of fused silica:

—reliable manufacturing procedures for producing large homogeneous blanks of this material have now been developed;

—fused silica can be polished well;

—it holds coatings firmly;

—all lenses of the system have not only a small, but also the same thermal expansion coefficient[3]

—fused silica has good time stability.

A discussion of the attendant questions can be found in Section 3.3 of the monograph by Wilson (1999).

Observations with telescopes that provide subarcsecond images need to be corrected for differential atmospheric refraction (Wynne and Worswick 1986; Wynne 1986; Wilson 1996, Sect. 4.4; Schroeder 2000, Sect. 9.5). The corresponding atmospheric dispersion corrector (ADC) can be realized

[3]According to Schott Lithotec (2003), it is 0.5×10^{-6} K^{-1} in the range 25–100°C.

by making the lenses of the field corrector more complex. In recent years, however, an ADC has been customarily built into the field corrector as an independent device.

At first glance, systems of the type described here have a linear field of view that is too large for CCD detectors to be effectively used. Thus, for example, the diameter of the field of view is 481 mm for system "S" and exceeds 600 mm for system "T". Meanwhile, such field sizes are typical in the modern designs of wide-angle telescopes. For example, a field 550 mm in diameter is expected to be achieved in the LSST project. The main difficulty here is associated not with filling the focal plane with many CCD chips, but with the necessity of rapidly reading out and promptly processing an extremely large amount of information. This problem has already been solved in some of the existing systems (Lesser and Tyson 2002; Walker 2002).

ACKNOWLEDGMENTS

I am grateful to V.V. Biryukov (Moscow State University) and A.A. Tokovinin (Cerro Tololo Inter-American Observatory) for valuable discussions of questions related to the use of large telescopes.

REFERENCES

1. J. R. P. Angel, M. Lesser, R. Sarlot, and T. Dunham, ASP Conf. Ser. **195**, 81 (2000).
2. D. R. Blanco, G. Pentland, C. H. Smith, *et al.*, Proc. SPIE **4842**, 85 (2003).
3. B. Delabre, *Optical Design for Astronomical Instruments* (Rio de Janeiro), http://www.on.br/institucional/portuguese/ciclo2002/pub/Delabre/RIO2002b.PPT (2002).
4. J. P. Emerson and W. Sutherland, Proc. SPIE **4836**, 35 (2002).
5. B. Gregory and M. Boccas, *The Blanco 4-m Telescope*, http://www.ctio.noao.edu/telescopes/4m/4m.html (2000).
6. T. E. Ingerson, *Empirical and Theoretical Modeling of the PFADC Corrector on the Blanco 4-m Telescope*, http://www.ctio.noao.edu/telescopes/4m/pfadc/pfadc_tei.html (1997).
7. M. P. Lesser and J. A. Tyson, Proc. SPIE **4836**, 240 (2002).
8. Schott Lithotec, *Synthetic Fused Silica. Optical and Technical Grades* (2003).
9. A. McPherson, S. C. Craig, and W. Sutherland, Proc. SPIE **4837**, 82 (2003).
10. N. N. Mikhelson, *Optical Telescopes. Theory and Design* (Nauka, Moscow, 1976) [in Russian].
11. F. E. Ross, Astrophys. J. **81**, 156 (1935).
12. L. G. Seppala, Proc. SPIE **4836**, 111 (2002).
13. D. J. Schroeder, *Astronomical Optics* (Academic, San Diego, 2000).
14. A. Tokovinin, B. Gregory, H. E. Schwarz, *et al.,* Proc. SPIE **4839**, 673 (2003).
15. J. A. Tyson, Proc. SPIE **4836**, 10 (2002).
16. A. R. Walker, Mem. Soc. Astron. Ital. **73**, 23 (2002).
17. R. N. Wilson, *Reflecting Telescope Optics* (Springer, Berlin, 1996), Vol. I.
18. R. N. Wilson, *Reflecting Telescope Optics* (Springer, Berlin, 1999), Vol. II.
19. C. G. Wynne, Astrophys. J. **152**, 675 (1968).
20. C. G. Wynne, *Progress in Optics,* Ed. by E. Wolf (North-Holland, Amsterdam, 1972), Vol. 10, p. 139.
21. C. G. Wynne, Observatory **106**, 163 (1986).
22. C. G. Wynne and S. P. Worswick, Mon. Not. R. Astron. Soc. **220**, 657 (1986).

Translated by V. Astakhov